2016

Experimental Investigations on Transient Surface Water Transport and Ice Accreting Processes Pertinent to Aircraft Icing Phenomena

Yang Liu
Iowa State University

Experimental investigations on transient surface water transport and ice accreting processes pertinent to aircraft icing phenomena

by

Yang Liu

A dissertation submitted to the graduate faculty

in partial fulfillment of the requirements for the degree of

DOCTOR OF PHILOSOPHY

Major: Aerospace Engineering

Program of Study Committee:
Hui Hu, Co-Major Professor
Leonard J. Bond, Co-Major Professor
Alric P. Rothmayer
Dale E. Chimenti
Xinwei Wang

Iowa State University
Ames, Iowa
2016

DEDICATION

I would like to dedicate this dissertation to my wife, Xi Yang and my son, David. Their support is the power for me to complete this work.

TABLE OF CONTENTS

LIST OF TABLES

LIST OF FIGURES

ACKNOWLEDGEMENTS

I would like to express my sincere gratitude and appreciation to my major advisors, Dr. Hui Hu and Dr. Leonard J. Bond, whose expertise, enthusiasm, and research attitude have been influencing me during my entire Ph.D. period. Without their generous guidance and support, this dissertation would not have been possible. I consider it a great honor to work with these prominent professors in the past four years.

My heartily appreciation also goes to my committee members, Dr. Alric P. Rothmayer, Dr. Dale E. Chimenti, and Dr. Xinwei Wang, for their generous help during my research. I would also like to thank them for evaluating my research work and giving me many insightful comments.

I am grateful to all the staff members in the Department of Aerospace Engineering, especially former and present department sectaries, Ms. Gayle Fay and Ms. Jacqueline Kester for their help on all the paperwork and many other important things.

I would like to thank Dr. Wenli Chen, Dr. Wei Tian, Dr. Rye Waldman, and Dr. Kai Zhang for their valuable help in completing the experiments and thesis writing. I also want to thank Dr. Wenwu Zhou, Mr. Morteza Khosravi, Mr. Haixing Li, Mr. Zhe Ning, Mr. Pavithra Premaratne, Mr. Linkai Li, Mr. Hao Guo and Mr. Liqun Ma for their help and the joys shared in the past four years.

I am also hugely grateful to my father and mother, Kaihe Liu, and Meiying Wang, who have given me this opportunity to study abroad. I cannot become who I am without their unconditional love and support throughout my life. My heartily appreciation also goes to my parents in-law, Lanshuan Yang, and Xiaocui Li, who dedicate so much in supporting my family and caring my newborn baby.

Finally, my deepest appreciation is reserved for my wife, Xi Yang, who has always been by my side during my Ph.D. study. With her love and encouragement, I have been able to overcome many difficulties in my life.

ABSTRACT

In the present study, an multi-transducer (sparse array) ultrasonic pulse-echo (MTUPE) technique was developed to quantify the transient surface behaviors of the water film flow driven by boundary layer airflow. The instantaneous surface waves riding on the free surface of the water film flow were characterized based on the measured time series of the water film thickness. Based on the time expansions of the measured thickness profiles of the surface water film flow, a instability transition, from periodical two-dimensional waves to pebbled waves of an obviously non-periodic nature, was observed. Then, the temporally-resolved spatial wave structures in the wind-driven water film flow were reconstructed, which provide more details of the surface morphologies and evolutions of the surface waves in the wind-driven water film flow.

A strategy, based on the use of frequency dependent ultrasonic attenuation, was investigated that has the potential to characterize and differentiate between different types of ice that can form on aircraft during winter operations. The measurement methodology and system were validated using the data for acoustic attenuation in water. The data for two types of ice, rime-like and glaze-like, are in agreement with results from previous measurements. There is a significant difference seen in the ultrasonic attenuation characteristics between the two types of ice. It would appear that there is potential to add attenuation data to on-aircraft ice detection systems which could then potentially enable ice-type specific based de-icing to be implemented. Such optimized de-icing could have a

potential for reducing winter weather operational costs, and ensure safety is maintained, or even improved.

A comprehensive experimental study was also conducted to quantify the transient surface water transport and dynamic ice accreting process over a wing surface at different icing conditions. The experiments were conducted in the Icing Research Tunnel available at Iowa State University (ISU-IRT). While the transient behaviors of the surface water transport over an NACA 23012 airfoil with realistic initial ice roughness at the airfoil leading edge were investigated using an innovative digital image projection-correlation (DIPC) technique, the unsteady heat transfer and phase changing processes under different icing conditions were examined in details based on the measured surface temperature maps over the ice accreting surfaces by using an infrared thermal imaging system. The objective of this study is to elucidate the underlying physics of surface water transport and ice accretion to improve our understanding of the important microphysical processes pertinent to aircraft icing phenomena to develop more effective and robust anti-/de-icing strategies to ensure safer and more efficient aircraft operations in cold weather.

CHAPTER 1
GENERAL INTRODUCTION

1.1 Literature Review

Aircraft icing has been considered as one of the most serious hazards to impact flight safety since early in the development of aviation (Smith 1929). Over the past few decades, though many efforts have been made to solve the icing problems, ice accretion on aircraft is still a big threat to flight safety (Potapczuk 2013). It is documented that there were 944 icing-related accidents and incidents occurred in the US from 1978 to 2005 (Petty and Floyd 2004; Green 2006). Then, Appiah-Kubi (2011) updated this number with another 228 accidents and 30 incidents from 2006 to 2010. According to these investigations, forty percent of the accidents were caused by in-flight icing, which typically occurs on aircraft wings, fuselage and control surfaces.

Most of the in-flight aircraft icing events take place when aircraft operate in cold clouds or precipitation containing a considerable amount of droplets. Ice accretion on aircraft surfaces can destroy the smooth airflow over lift and control surfaces which decreases the ability of aircraft to generate lift (Steuernagle et al. 2008). The ice shapes formed on aircraft surfaces could further affect the aerodynamic performance of aircraft by reducing the stall margin (Gent et al. 2000). Additionally, the uncontrolled shedding of ice which has built up on aircraft surfaces may severely damage aircraft components (Bassey and Simpson 2007).

From an economic perspective, ice accretion can increase the costs of flight operations due to the use of anti/de-icing fluid and equipment. An investigation by the National

Business Aviation Association (NBAA) found that the cost of removing heavy wet snow from a medium-sized business jet is about $3,000, while that for the removal of frozen/freezing rain can be up to $10,000. Moreover, the time spent in performing de-icing procedures can cause flight delays or even cancellations, which can then significantly impact airline performance, and hence total operation costs (Caliskan and Hajiyev 2013).

The in-flight ice formation and accretion are mainly determined by weather conditions, i.e., liquid water content (LWC), atmosphere temperature, and water droplet size. Various ice morphologies can be produced under different weather conditions (Shin and Bond 1992; Vargas and Tsao 2008). In the past years, many efforts have been made to characterize the effects of LWC, air temperature and velocity, and droplet size on the ice formations on aircraft (Hansman and Kirby 1986; Gent et al. 2000; Cebeci and Kafyeke 2003).

If the air temperature is very low (typically below -10 °C), when aircraft encounter cloud with low LWC and small water droplets, rime ice will form as the supercooled droplets freeze and accumulate upon impact. Rime ice appears to be white and opaque containing many small bubbles and ice grains (Hansman and Kirby 1987). If the air temperature is just below the freezing point, glaze ice tends to form, especially when an aircraft goes through cloud with a higher LWC and larger droplets. In the case of glaze ice accretion, the impinged droplets will deform and run back over the aircraft surfaces before freezing downstream. Glaze ice appears to be smooth, clear, and dense, and it forms on the leading edge of airfoils with horn-like shapes that project into the airflow (Hansman

and Kirby 1987). Mixed ice is a transition state between rime and glaze ice (Steuernagle et al. 2008). Rime ice generally conforms to the aircraft surfaces, and has a small effect on aircraft performance, while glaze ice covers more surfaces and has a more severe effect on airflow and heat transfer. Moreover, the water run-back behavior in glaze icing process could essentially redistribute the impinging water mass and disturb the local flow field, and hence, make the icing processes even more complex and unpredictable (Du et al. 2010; Zhang et al. 2015).

It is suggested that heat transfer is one of the most essential mechanisms that controls the ice morphology formed on aircraft (Yamaguchi and Hansman 1992). Ice forms as heat transfer removes the latent heat in water. If heat transfer is adequate to remove all of the latent heat of fusion in the collected water, the water will freeze immediately upon impact. The ice morphology formed in such situations is typical rime ice. If heat transfer is inadequate to remove all of the latent heat in the collected water, a portion of the collected water will deform and run back over the aircraft surfaces before freezing downstream, which is a typical glaze icing process (Hansman and Turnock 1989).

Rime ice accretion is mainly determined by the droplet impingement behavior, in which the amount and rate of ice accretion are controlled by the droplet collection efficiency (Liu and Hu 2016); while in glaze ice accretion, the ice growth rate is essentially controlled by the local heat transfer capacity that determines the amount of latent heat removal from the surface water film and rivulets (Du et al. 2010)

To reduce the potential harmful effects of aircraft icing, many anti/de-icing systems have been developed. These can be considered in three groups and are in the form of

freezing point depressants, thermal melting, and surface deformation (Thomas et al. 1996). With these various anti/de-icing approaches, the amount and the rate of ice removal is mainly determined by the volume of de-icing fluid or electrical power applied. For rime ice accretion, due to the porous nature of the structures in ice layers and typically the smaller area on the aircraft surfaces on which it forms, it is easier to remove, when compared with glaze ice, which is denser and typically has a higher adhesion to aircraft surfaces. Glaze ice usually extends further downstream on a wing surface and typically covers a larger area. Therefore, more de-icing fluid or power is required to remove glaze ice accretion (Thomas et al. 1996). In looking at performance optimization, most of the current de-icing systems were however, developed without considering the characteristics of the accreted ice. During flight operations, the de-icing systems are usually implemented using the same process and strategies, regardless of the ice type. As a result in operation, a lot of potentially unnecessary actions are performed to ensure effective removal of ice on aircraft surfaces (Gao and Rose 2009; Zou et al. 2013). In looking to improve winter flight operational performance, methods and techniques for ice detection and characterization are needed that can potentially improve and optimize de-icing.

To address this need, many ice detection and monitoring techniques have been investigated which use either direct or indirect measurement approaches. Most of the direct measurement approaches provide icing warnings with data from measuring surface properties of aircraft with changes in mass, reflective index, electrical/thermal conductivity, dielectric coefficient, or inductance. Indirect measurement approaches, however, detect icing events based on monitoring flight performance metrics, such as a

lift decrease or drag increase, or from measurements of weather conditions, such as air humidity and temperature (Homola et al. 2006; Caliskan and Hajiyev 2013).

As ice forms on aircraft surfaces, the flight performance can be affected very quickly. Therefore, for safety reasons, direct methods for ice detection are generally preferred. Among the measurement methods are those which use ultrasonic techniques and these have been widely studied and applied (Gao and Rose 2009). As reported by Hansman and Kirby (1986), an ultrasonic pulse-echo technique was developed to provide real-time thickness measurements of water/ice accretion. The water/ice layers were characterized using ultrasonic echoes where signals were generated at interfaces. In laboratory studies, such interface reflections were displayed on an oscilloscope. In recent years, ice detection and classification have been achieved by using the ultrasonic guided-wave technologies, in which the ice types were classified based on the dispersion characteristics of the phase and group velocity curves for waves in the multi-layer system (Vellekoop et al. 1999; Hongerholt et al. 2002; Gao and Rose 2009).

In terms of implementations on aircraft, various ultrasonic transducers and systems have been fabricated to provide in-situ ice detection. One example of a recent implement was that provided by Liu et al. (2008), who developed two types of flexible ultrasonic sensors that were used to monitor in-situ structural thickness and ice build-up. These transducers were easily attached on the inside of the curved airfoil surfaces on aircraft. To further extend the capability of ice detection and characterization with ultrasonic techniques, new approaches are required to more quantitatively characterize the types, and thickness, of ice that forms on aircraft.

The ice accretion on aircraft usually occurs along with surface water transport, especially in glaze icing conditions, and such surface water behaviors can redistribute the water impingement and transport, and disturb the local flow field, and hence, affect ice formation and accretion (Du et al. 2010; Zhang et al. 2015). The current icing prediction models, however, simplify many micro-physical details of water-air interactions (Wright 1999) that can essentially affect water transport and ice accretion (Fortin et al. 2006).

In looking to improve icing prediction performance, methods and techniques of dynamic thickness measurements for thin water film flows are needed that can potentially provide more physical details of surface water transport driven by boundary layer airflow. The laser induced fluorescence (LIF) technique is one of the approaches that has been widely used in measuring thin film thickness (Lel et al. 2005; Schagen and Modigell 2007). For applications, since the fluorescence intensity is temperature dependent, the measurements can be significantly affected in a temperature varying icing environment (Wang et al. 2012). In recent years, optical imaging techniques have been widely developed that employ structured light projections (Cochard and Ancey 2008; Cobelli et al. 2009; Hu et al. 2014). This approach has been demonstrated to be able to characterize surface deformations and morphologies of liquid films (Zhang et al. 2015). To implement this technique, the measuring fluid has to be formulated so that a very high reflectivity can be achieved at the fluid surface (Zhang et al. 2015). In a water film flow, however, the reflection index at the water-air interface is low, and only a fraction of the projected light can be reflected while the remainder penetrates into the water, which becomes a typical error source of the measurements. In looking at measurements of surface water transport

in potential icing conditions, a technique capable of providing real-time on-site sensing of water film flows is desired.

To address this need, ultrasonic techniques were introduced to measure the surface water/ice thickness using the time-of-flight principal (Svilainis 2012), which enables temporally-resolved measurements with rapid time response and high sampling resolution. As reported by Hansman, an ultrasonic pulse-echo technique was developed to characterize water/ice layers using ultrasonic echoes that were displayed on an oscilloscope (Hansman and Kirby 1986; Hansman et al. 1988). A modified ultrasonic technique was then investigated by Serizawa (2004) that can measure the local film thickness in a stratified air-water flow over a horizontal plate. A similar method was also applied in the measurements of the instantaneous film thickness of the falling film flow in an acrylic resin channel (Li and Serizawa 2004). In recent years, an ultrasonic transmission thickness measurement system (UTTMS) was developed to measure the time-dependent spatial distribution of water rivulets around the surface of a bridge stayed cable suffering from rain-wind induced vibration (Li et al. 2010).

The ultrasonic pulse-echo technique is therefore, believed to have the capbility to measure the thin water film flow driven by boundary layer airflow, and resolve the thin water film structures and their time-evolutions.

Besides the surface water transport behavior, heat transfer is another key factor that affects ice accretion. Based on the heat transfer models in the various ice accretion processes, there are multiple heat transfer mechanisms occurring on the airfoil/ice surfaces during ice accretions (Myers 2001; Fortin et al. 2006). Among these mechanisms,

convective heat transfer is considered to be predominant in aircraft icing (Dukhan et al. 2003; Liu et al. 2015). Therefore, the accurate modeling of convective heat transfer is desired to aid in the design of ice protection systems to mitigate icing effects, and furthermore, to improve the determination of safety operating conditions (Tecson and McClain 2013a)

Heat transfer modeling in ice accretion is first formulated by Messinger (1953). Then, numerous improvements and corrections have been subsequently made to the Messinger model. Based on these studies, the ice and water growth in the presence of incoming super-cooled droplets can be evaluated and predicted (Myers 2001). The results derived in these studies indicate that rime icing could be adequately simulated and well understood. Glaze icing, however, is hard to be accurately simulated, and there is considerable uncertainty regarding the heat transfer capacity and ice accretion profiles (Kind et al. 1998). To provide essential physical descriptions regarding the heat transfer during ice accretion, many experimental studies have been conducted in both wind tunnel and flight tests.

As reviewed by Kind (1998), there are mainly two experimental approaches to study the heat transfer characteristics during ice accretion. One is called dry-air testing, in which replicas of the real ice shapes are used to evaluate the effect of the simulated irregular ice shapes and roughness elements on the aerodynamic performance and local convective heat transfer (Arimilli et al. 1984; Hansman and Kirby 1987; Hansman et al. 1991; Yamaguchi and Hansman 1992; Henry et al. 1994; Bragg et al. 1994; Henry et al. 1995; Bragg et al. 1996; Kind et al. 1998; McClain et al. 2010). It is considered that the initially frozen water beads form the initial roughness elements. These roughness elements may trigger the

aerodynamic boundary layer transition, and hence, enhance the convective heat transfer. The enhanced convection, in turn, accelerates the roughness formation and ice accretion (Hansman and Kirby 1987; Bragg et al. 1996). The other approach to investigate the heat transfer process is to create real ice shapes in an icing wind tunnel. The heat transfer measurements are performed on the ice shape itself, rather than a casted ice model (Yamaguchi and Hansman 1992; Wang et al. 2007; Wang et al. 2008). It is observed that the convective heat transfer is constant on smooth and uniform ice surfaces, and is enhanced in regions filled with roughness and ice feathers (Henry et al. 2000).

Various measurement techniques have been developed and implemented in these experimental studies to observe and reconstruct the features in icing process. Among these techniques, strobe synchronized CCD video technology, ultrasonic measurement techniques, thermocouple measurements, and infrared thermography are typical methods that have been successfully applied in dealing with the icing-related measurements (Kind et al. 1998; Henry et al. 2000; Wang et al. 2008; Mohseni et al. 2012). The use of thermocouples provides researchers the access to collect the time-resolved temperature variation information at a single point. However, thermocouple measurement is an intrusive method that can disturb the airflow over an airfoil, and hence, influence the convective heat transfer process.

As infrared technology has developed quickly in recent years, infrared thermography is now available for measuring surface temperature distribution over an iced airfoil. An infrared camera with high sensitivity can provide accurate temperature measurements at both high spatial and good temporal resolutions. Hansman and Yamaguchi investigated

the laminar/turbulent transition behavior on an iced surface using an infrared technique (Yamaguchi and Hansman 1992). Bragg measured the convective heat transfer on an airfoil with simulated ice roughness by applying the infrared thermography (Bragg et al. 1996). The heat transfer characteristics were well defined in these studies. However, most of them were focused on the end-point features, the initial transient heat transfer behavior was ignored, which is actually of great importance in understanding the evolution of the ice accretion at the initial state.

In order to quantify the physical details during an actual icing process, from droplet impingement to ice shape formation, a time-resolved temperature distribution measurement is strongly desired to monitor and evaluate the transient heat transfer behavior. Mohseni implemented an infrared imaging technique in monitoring the ice accretion on an airfoil (Mohseni et al. 2012). This technique makes it possible to measure the transient ice formation and growth at the leading edge of an NACA 0021 airfoil based on the temperature features associated with the ice features.

As many experimental evidence of heat transfer have been provided to aid the improvement of ice accretion modeling methods, the current ice accretion codes are still limited in their capabilities in predicting ice accretion, partially due to the use of simplified ice roughness models. In the LEWICE, the ice roughness height is estimated based on the sand-grain equivalent model. Initially formed roughness is suggested to be a key factor affecting icing process (Yamaguchi and Hansman 1992; Henry et al. 1994; Dukhan et al. 1996; Henry et al. 2000). As initial ice roughness forms, the boundary layer flow and heat transfer are essentially altered as well as the water collection and run-back process, the

simplification could essentially affect the ice accretion shape and size because the sand-grain roughness is different from the real ice roughness as found in the previous icing experiments (Shin 1996). Based on the comparison of the ice shapes generated in the icing experiments and that from the LEWICE program, it was found that the predicted ice shapes did not match well with the experimental results. The comparison, consequently, presented a poor agreement of the convective heat transfer coefficients (Shin 1996; Vargas 2007).

Many experimental studies have been conducted to provide realities of the effects of the roughness elements on the surface water transport, local convective heat transfer, and boundary layer development. However, since the initial ice roughness is difficult to characterize, most of these studies were focused on the effects of the non-realistic ice roughness, or simplistically distributed roughness (Henry et al. 1994; Bragg et al. 1994; Henry et al. 1995; Kerho and Bragg 1995; Bragg et al. 1996; Winkler and Bragg 1996). Although these simulated roughness characterizations are easy to implement, they may not reflect the irregularity and broad range of topographical scales of practical roughness (Bons and Christensen 2007). Different ice accretions have unique surface features that are not always well captured by ordered arrays of discrete roughness elements. The use of these non-realistic ice roughness is proved to create biases in convective heat transfer results as compared with that using realistic distributions of roughness elements (Bons 2002; Mart et al. 2012). Assessing the impact of realistic roughness features on the initial ice accretion and heat transfer process is critical to improving the accuracy of ice accretion prediction.

Over the years, several techniques have been developed to create realistic ice roughness distributions (Rothmayer 2003; Tecson and McClain 2013b). One of the recent techniques is a Lagrangian droplet simulator, which can be used to generate realistic ice roughness distributions (Tecson and McClain 2013a; Tecson and McClain 2013b). The resultant roughness is a bead distribution with random distribution and diameters. This approach enables the characterization of boundary layer development and convective heat transfer from surfaces exhibiting such kind of roughness distributions(Tecson and McClain 2013a). The real ice roughness elements from real icing conditions may be of various shapes and sizes. To better understand the boundary layer flow and local heat transfer in these situations, another approach employing cast surfaces of real icing models was developed (Dukhan et al. 2003). The three-dimensional features of ice accretion can be captured using the mold and casting method. However, this approach is time-consuming in operation, and the cost can be significant (Lee et al. 2012). In recent years, laser-based and other optical scanning methods have been developed to accomplish three-dimension digitization of ice accretion (Lee et al. 2012). The 3-D laser scanners developed in recent years were proved to be capable of accurately recording and reproducing the details of ice formations (Lee et al. 2014).

As the realistic initial roughness can be successfully reconstructed, the microphysical details in water/ice transport process interacting with the initial ice can be further quantified. To achieve that, advanced experimental techniques capable of providing accurate quantitative measurements of surface morphology are highly desired. The structured light technique developed in recent years have been successfully applied in

reconstructing surface topographies. The basic methodology of this technique is to actively project known light patterns onto a surface, and extracting 3-D surface shapes from the images of the light patterns captured from one or more points of view (Salvi et al. 2010). As good space and time resolutions have been achieved, this technique is widely used in 3-D sensing, object recognition, robotic control, industrial inspection of manufactured parts, stress/strain and vibration measurements, biometrics, biomedicine, dressmaking, and visual media (Salvi et al. 2010). In recent years, this technique has been introduced to measure fluid flow (Cazabat et al. 1990; Zhang and Su 2002; Cobelli et al. 2009; Hu et al. 2014). As the most recent progress, a digital image projection (DIP) technique was developed to quantify the surface water transport process over an NACA 0012 airfoil (Zhang et al. 2015). The microphysical details from droplet impingement to water film/rivulets formation and run-back were revealed based on the DIP measurements, which provides a decent method for measuring surface water/ice morphology.

Since the initial ice roughness is closely coupled with the local flow field and convective heat transfer, even a slight change in roughness characteristics (i.e., element size, element spacing, etc.) could essentially impact the convective heat transfer, and hence, change the amount and rate of ice accretion (Tecson and McClain 2013a). Therefore, it is important to accurately characterize the effect of the initial roughness elements on the heat transfer and ice accretion process. Over the past few decades, many experimental studies revealed that the initial ice roughness is significant because it couples the fluid flow, droplet impingement, and heat transfer processes (Olsen and Walker 1986; Yamaguchi and Hansman 1992; Henry et al. 1994; Dukhan et al. 1996; Henry et al. 2000).

The initial ice roughness essentially induces higher levels of turbulence in the airflow and accelerate the convective heat transfer from the surfaces to freestream (Vargas 2007). However, more transient details are desired for the better understanding of the effect of realistic initial roughness on icing processes.

1.2 Motivation for the Current Research

In summary, the literature review shows several research gaps:

1. The current icing prediction models simplify many physical details (e.g., surface water transport, transient heat transfer, and formation of initial ice roughness), which can essentially affect the icing process on aircraft.

2. A technique capable of providing real-time on-site measurements of surface water flow on the aircraft surfaces is strongly desired. More quantitative details of the wind-driven surface water film flow should be investigated to provide more fundamental microphysical insights pertinent to the water transport behavior in icing processes.

3. To further extend the capability of ice detection and characterization with ultrasonic techniques, new approaches are required to more quantitatively characterize the types, and thickness, of ice that forms on aircraft.

4. The time-resolved measurements of heat transfer along with ice accretion in real icing processes are strongly desired to provide more transient details from droplet impingement to ice formation.

5. The quantitative measurements of the surface water/ice transport process over a wing model with realistic initial ice roughness are demanded to provide the microphysical

details of the surface water film/rivulets run-back behaviors interacting with the initial ice roughness.

6. The time evolution of the surface temperature distribution over a wing model with realistic initial ice roughness is strongly desired to provide more transient details in the evaluation of the effect of the initial ice roughness on heat transfer and ice accretion.

To fill these gaps, the objectives of the present study are listed as follows:

1. Develop a multi-transducer (sparse array) ultrasonic pulse-echo (MTUPE) technique to measure the thin water film flow driven by boundary layer airflow, which has the capability to resolve the thin water film structures and their time-evolutions.

2. Develop a strategy based on the use of frequency dependent ultrasonic attenuation, which has the potential to characterize and differentiate between different types of ice that can form on aircraft in winter operation.

3. Establish an energy balance model for the transient ice accretion on aircraft, and perform real-time temperature measurements over an ice accreting wing surface in the ISU icing research wind tunnel (ISUIRT) to provide more thermal details in ice accretion.

4. Apply the digital image projection-correlation (DIPC) technique to provide non-intrusive, temporally resolved, and full-field measurements of the dynamic water/ice transport process over a wing surface, and evaluate the effect of the initial ice roughness on the transient water/ice run-back behavior.

5. Thermally resolve the transient heat transfer and ice accretion processes over a wing surface with realistic initial ice roughness, and assess the impact of the roughness on the water collection process and heat transfer enhancement.

1.3 Thesis Organization

The dissertation includes eight chapters in total. A general introduction (Chapter 1) is given at the beginning, and a conclusion is provided as the last chapter of the dissertation (Chapter 8). Appendix is also included at the end of this dissertation to discuss the statistical characteristics of the wind-driven surface water film flow, which are not covered in the main chapters.

Chapter 2 describes the development of a multi-transducer (sparse array) ultrasonic pulse-echo (MTUPE) technique, which is to be used in the measurements of surface water film flows driven by boundary layer airflow. The technical basis for the MTUPE technique and the factors that influence the measurements were discussed in detail.

Chapter 3 presents a quantitative study of the wind-driven surface water film flow using the MTUPE technique. The instantaneous surface waves riding on the free surface of the water film flow were characterized based on the measured time series of the water film thickness. The instability transition was discussed based on the time expansions of the measured thickness profiles of the surface water film flow. The temporally-resolved spatial wave structures in the wind-driven water film flow were also illustrated.

Chapter 4 introduces the development of a novel strategy, based on the use of frequency dependent ultrasonic attenuation, that has the potential to characterize and differentiate between different types of ice that can form on aircraft. The measurement methodology and system were described and validated. The attenuation data for two types of ice, rime-like and glaze-like, were presented and compared with results from previous measurements.

Chapter 5 described an instant heat balance model during ice accretion on an airfoil model. Infrared thermography was used to provide measurements of surface temperature distribution over an ice accreting NACA 0012 airfoil. The initial ice formation and accretion in both dry and wet icing conditions were characterized based on the temperature maps. The local temperature variations and evolutions around the leading edge were extracted to evaluate the transient heat transfer details.

Chapter 6 presented an experimental study of the effect of initial ice roughness on the transient water/ice run-back process over an NACA 23012 airfoil. A digital image projection-correlation technique was used to provide non-intrusive, temporally resolved, and full-field thickness measurements of the water/ice transport process. The instantaneous surface morphologies of the water film/rivulets flow over the wing with different leading edge conditions (smooth and rough) were reconstructed and quantified. As a new method was proposed to recognize the film/rivulets boundary, the instantaneous chordwise distribution of water coverage ratio was acquired, from which the dynamic process of film/rivulets boundary formation, rivulets transition, and development were

quantified. The time-averaged thickness profile of the water film/rivulets flow was derived, based on which the characteristics of the steady-state rivulets flow were extracted.

Chapter 7 presented an experimental study of the effect of initial ice roughness on the transient ice accretion and heat transfer process over an NACA 23012 airfoil. Icing experiments were performed in the ISU Icing Research Wind Tunnel (ISU-IRWT). A high-speed videography was used to visualize the icing process, i.e., droplet collection, ice formation, water run-back, and the evolution of the accreted ice. An infrared thermometry was also applied to map the temperature distribution over the ice accreting airfoil surfaces. The effect of the realistic ice roughness on the droplet collection distribution and the heat transfer enhancement were elucidated.

CHAPTER 2
DEVELOPMENT OF AN MULTI-TRANSDUCER ULTRASONIC PULSE-ECHO TECHNIQUE

2.1 Introduction

Aircraft operating in cold weathers face the risk of icing. Flight performance can be affected when ice accumulates on aircraft surfaces (Steuernagle et al. 2008). The morphology of in-flight icing is determined by weather conditions (Gent et al. 2000). For example, if the air temperature is very low (typically below -10°C), when an aircraft encounters cloud with low liquid water content (LWC) and small water droplets, rime ice will form. If the air temperature is just below the freezing point, glaze ice tends to form as aircraft operate in cloud with higher LWC and larger droplets. In the case of glaze ice accretion, the impinged droplets usually deform and run back over aircraft surfaces before freezing downstream (Hansman and Kirby 1987). Such surface water behaviors can redistribute the water impingement and transport, and disturb the local flow field, and hence, affect ice formation and accretion (Du et al. 2010; Zhang et al. 2015). The current icing prediction models, however, simplify many micro-physical details of water-air interactions (Wright 1999) that can essentially affect water transport and ice accretion (Fortin et al. 2006).

In looking to improve icing prediction performance, methods and techniques of dynamic thickness measurements for thin water film flows are needed that can potentially provide more physical details of surface water transport driven by boundary layer airflow. The laser induced fluorescence (LIF) technique is one of the approaches that has been

widely used in measuring thin film thickness (Lel et al. 2005; Schagen and Modigell 2007). For applications, since the fluorescence intensity is temperature dependent, the measurements can be significantly affected in a temperature varying icing environment (Wang et al. 2012). In recent years, optical imaging techniques have been widely developed that employ structured light projections (Cochard and Ancey 2008; Cobelli et al. 2009; Hu et al. 2014). This approach has been demonstrated to be able to characterize surface deformations and morphologies of liquid films (Zhang et al. 2015). To implement this technique, the measuring fluid has to be formulated so that a very high reflectivity can be achieved at the fluid surface (Zhang et al. 2015). In a water film flow, however, the reflection index at the water-air interface is low, and only a fraction of the projected light can be reflected while the remainder penetrates into the water, which becomes a typical error source of the measurements. In looking at measurements of surface water transport in potential icing conditions, a technique capable of providing real-time on-site sensing of water film flows is desired.

To address this need, ultrasonic techniques were introduced to measure the surface water/ice thickness using the time-of-flight principal (Svilainis 2012), which enables temporally-resolved measurements with rapid time response and high sampling resolution. As reported by Hansman, an ultrasonic pulse-echo technique was developed to characterize water/ice layers using ultrasonic echoes that were displayed on an oscilloscope (Hansman and Kirby 1986; Hansman et al. 1988). A modified ultrasonic technique was then investigated by Serizawa (2004) that can measure the local film thickness in a stratified air-water flow over a horizontal plate. A similar method was also

applied in the measurements of the instantaneous film thickness of the falling film flow in an acrylic resin channel (Li and Serizawa 2004). In recent years, an ultrasonic transmission thickness measurement system (UTTMS) was developed to measure the time-dependent spatial distribution of water rivulets around the surface of a bridge stayed cable suffering from rain-wind induced vibration (Li et al. 2010).

In the present study, a multi-transducer (sparse array) ultrasonic pulse-echo (MTUPE) technique was developed to measure the thin water film flow driven by boundary layer airflow. The technical basis for the MTUPE technique and the factors that influence the measurements were described.

2.2 Technical Basis and Measurement Principles

Figure 2.1 shows the schematic of the multi-transducer ultrasonic pulse-echo (MTUPE) system developed in the present study to quantify the transient behavior of wind-driven surface water film flows over a test plate. The MTUPE system includes a multichannel inspection unit (Omniscan iX) and a phased ultrasonic transducer array (i.e., comprised of multiple ultrasonic transducers). The system is functioned as a multiplexer, which has the capability to simultaneously generate and send voltage pulses to multiple (up to 8) ultrasonic transducers. With the high voltage excitation, the ultrasonic transducers can emit ultrasonic waves into the object of interest (i.e., surface water film flows over the test plate). The emitted ultrasonic waves will then interact with different materials along their propagation paths, and are partially reflected at the interfaces between the different media (e.g., at the interfaces of test plate–water and water-air). The reflected ultrasonic waves are then received by the same transducers in pulse-echoes. These echo responses are

collected, recorded and processed to derive time-resolved measurements to quantify the transient behavior of the unsteady wind-driven surface water film flows.

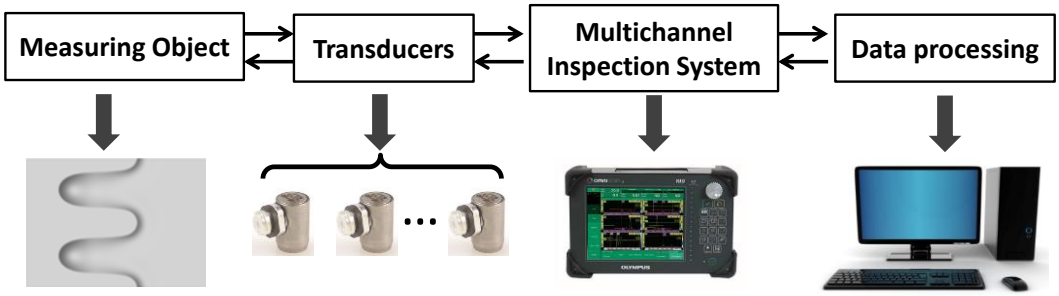

Figure 2.1 A typical multi-transducer ultrasonic pulse-echo (MTUPE) system

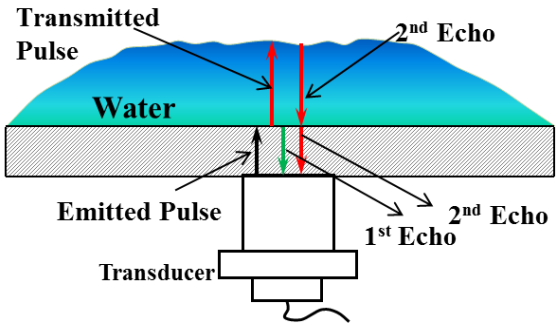

Figure 2.2 A schematic for local film thickness measurements using ultrasonic pulse-echo technique

Figure 2.2 shows schematically the technical basis of the ultrasonic pulse-echo (UPE) technique for achieving quantitative measurements of the local surface water film thickness over a test plate. An ultrasonic pulse is emitted into the surface water film flow over the test plate by using a piezoelectric based ultrasonic transducer. A fraction of the ultrasonic waves would be reflected at the plate-water interface; and the reflected waves, which are identified as the 1st echo, will be received by the ultrasonic transducer in real time. The remaining ultrasonic waves would transmit into the water film flow, and then are largely reflected at the water-air interface. The reflected waves, which are identified

as the 2nd echo, are partially transmitted through the plate and then received by the transducer. Based on the time-of-flight principle (Svilainis 2012), the water film thickness can be calculated using Eq. (2.1).

$$h = \left(\Delta t \times c\right)/2 \tag{2.1}$$

where h is water film thickness, Δt is the time interval between the two echoes, and c is acoustic velocity in water.

2.3 Discussions on the Measurements of MTUPE System

For the thickness measurements using the ultrasonic pulse-echo method, several factors need to be considered, which may influence measurement performance. A typical pulse-echo signal obtained in an individual channel of the MTUPE system is shown in Figure 2.3(a). Several echoes (i.e., in the form of multiple peaks) can be found in the signal sequence. An auto-correlation algorithm (Eq (2.2)) was used to define the time intervals between the echo signals.

$$R(\tau) = E\left[\left(Y_t - \mu\right)\left(Y_{t+\tau} - \mu\right)\right]/\sigma^2 \tag{2.2}$$

Figure 2.3(b) shows an example of the auto-correlation function of the signal sequence. The time intervals between different echoes are determined by finding the time delays corresponding to the local peaks in the auto-correlation profile. As shown clearly in the figure, the time interval between the first and second echoes is the time delay at the second correlation peak in the auto-correlation profile.

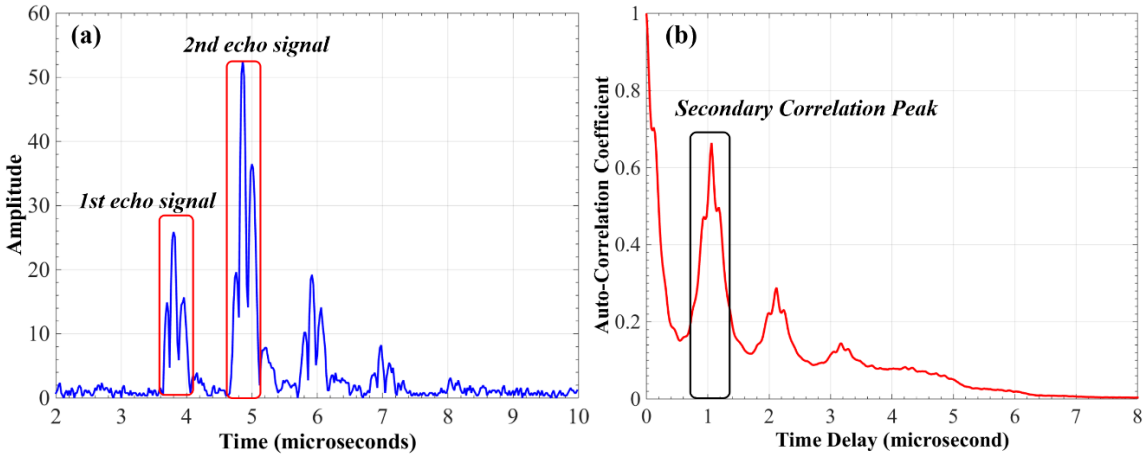

Figure 2.3 Typical ultrasonic signals in time-of-flight. (a) A typical echo signal obtained using MTUPE system. (b) Autocorrelation profile of the echo signal.

In the ultrasonic pulse-echo measurements, it is necessary to match the transducer characteristics to the operating configurations. The amplitude characteristics of a typical transducer-emitted ultrasonic pulse signal are generally determined by several factors, e.g., near-field fluctuation, beam-spread effect, wave attenuation, mode-conversion, interface reflection and transmission (Ensminger and Bond 2011). In the present study, since the ultrasonic beam was set to be normally incident into the measuring objects, there is a minimal mode conversion at the interfaces. Additionally, no significant grain or other scatterers is embedded along the propagation path of the ultrasonic waves, the wave attenuation is therefore minor and can be neglected. In looking to quantitatively evaluate the amplitude characteristics, more details about the near field effect, beam spread, and interface reflection and transmission are discussed in this study.

2.3.1 Near Field Effect

The sound field for a transducer can be generally divided into two zones: near-field and far field. The near-field is the region close to the transducer front where there is

interference between the plane and edge waves going through a series of maxima and minima. The location of the last maxima is known as the near-field length N_0, which is given in Eq (2.3) (Ensminger and Bond 2011).

$$N_0 = D^2 f / 4c \tag{2.3}$$

where D is element diameter of a transducer, f is the center frequency of the transducer, and c is acoustic velocity.

The far-field is the region beyond the near-field where the wave amplitude on-axis is well behaved and follows a decay/spreading law. Because of the complex acoustic field fluctuation within the near-field, it is usually difficult to make accurate amplitude dependent measurements. Far-field measurements at ranges between one to three times of the near field length are generally preferred. For the case of the present study, the near-field distance was estimated to be 7.4 mm by using Eq (2.3). The region of interest for the present study (>12.5 mm) is therefore beyond the near-field, and within the preferred measurement range.

2.3.2 Beam Spread Effect

For a flat ultrasonic transducer with finite aperture, as the ultrasonic beam propagates along the transducer axis, it generally diverges due to the aperture effect, known as "beam spread". Beam spread takes place because the beam is not a perfect cylinder of energy. As particles vibrate, some energy would be transferred radially out of the primary direction of wave propagation (Schmerr 1998). In the ultrasonic pulse-echo measurements, "beam-spread" effect may reduce the amplitude of reflections, since the sound field is less concentrated and, therefore, within the measurement range, becomes less intense. In the

present study, the -6 dB pulse-echo beam-spread angle was estimated by using Eq. (2.4) (Ensminger and Bond 2011) in order to evaluate the "beam-spread" effect.

$$\sin(\alpha/2) = 0.514c/fD \tag{2.4}$$

where $\alpha/2$ is half angle spread between -6 dB points, c is the wave propagation velocity in the material, f is the frequency of the ultrasonic pulse, and D is the diameter of the transducer element.

For the experimental settings used in the present study, the beam spread angle was estimated to be $\alpha = 3.52°$ in the substrate plate, and 2.76° in water. The maximum beam diameters at the plate-water and water-air interfaces were thus estimated to be 0.78 and 0.83 mm, respectively. Then, the beam diameters of the first and second echo signals at the transducer front were estimated to be 1.56 and 1.68 mm, respectively, which are smaller than the transducer diameter (3.175 mm). The energy loss due to the "beam spread" effect is therefore small and can be neglected.

2.3.3 Interface Reflection and Transmission

The energy in the ultrasonic pulse-echoes is partitioned at interfaces where there is a difference in acoustic impedance. In the present study, the ultrasonic pulse-echoes would go through two interfaces that generate multiple echo signals. A good estimation of the reflection and transmission amplitude is necessary to evaluate the signal-to-noise ratio (SNR) of the signal sequence.

The ratio of the reflected wave amplitude and the incident wave amplitude is known as the reflection coefficient, which can be calculated by using Eq. (2.5). The relationship between the transmission and reflection coefficients at a certain interface is given by Eq.

(2.6). Based on the acoustic properties of the materials used in the present study (as listed in Table 2.1), the reflection coefficients at the plate-water interface and water-air interface were calculated to be 0.32 and 0.99, respectively.

$$R_{12} = R_{21} = \left| \frac{Z_2 - Z_1}{Z_2 + Z_1} \right| \tag{2.5}$$

$$T_{12} \cdot T_{21} = 1 - R_{12}^2 \tag{2.6}$$

Table 2.1 Acoustic Properties of Materials

Material	Acoustic Speed, c (m/s)	Density, ρ (kg/m^3)	Acoustic Impedance, Z (kg/m^{2}s ($\times 10^3$))
FullCure®830 VeroWhite	2415	1183	2856.95
Water (20 °C)	1483	1000	1483
Air (20 °C)	343	1.2	0.412

The amplitudes of the 1st echo and the 2nd echo signals were then calculated using the reflection and transmission coefficients, and expressed in dB as shown in Table 2.2. By comparing the amplitude of the echo signals with the noise level, the minimum SNR was found to be more than 10 dB for the MTUPE system with the experimental settings of the present study. It confirms that the MTUPE system used in the present study is capable of providing accurate "time-of-flight" measurements with reasonably good SNR.

Table 2.2 Estimation of Echo Amplitude in dB

Echo Signals	Amplitude Coefficient	Echo Amplitude
1st Echo	R_a	-5 dB
2nd Echo	$R_b(1\text{-}R_a^2)$	-1 dB

2.4 Resolution and Validation of the MTUPE System

For the MTUPE system used in the present study, the resolution of the measured water film thickness is determined by the sample frequency of the system. With the data sampling rate being 100 MHz and the acoustic velocity in water being 1483 m/s at the room temperature of 20°C, the measurement resolution of the MTUPE system used in this study is estimated to be ± 5 μm.

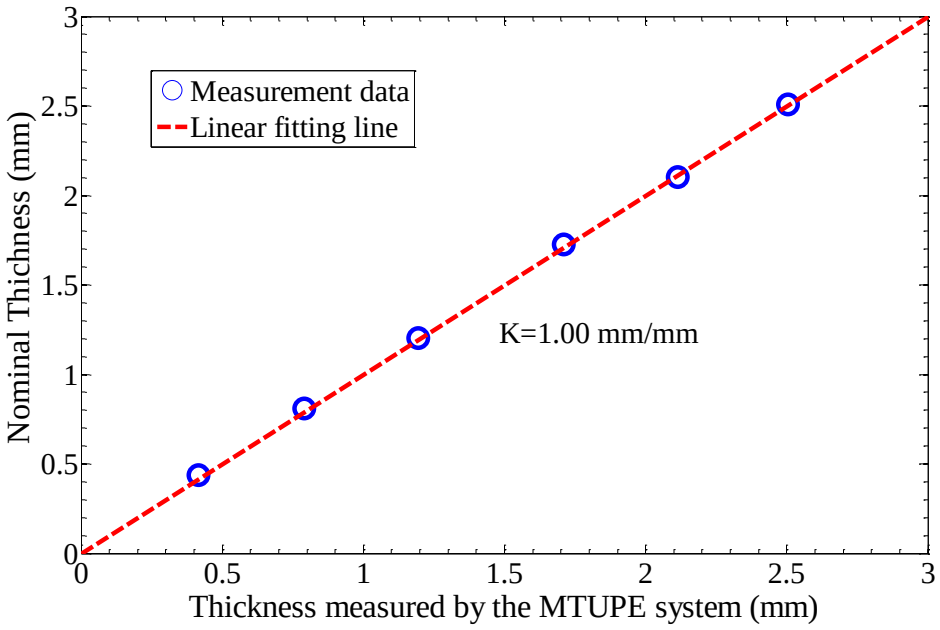

Figure 2.4 Comparison of the thickness measured using the MTUPE system and the nominal thickness.

A simple experiment was designed to demonstrate the feasibility of the MTUPE system described above for water film thickness measurements over the test plate. For the demonstration experiment, a small pool of water was poured over a flat test plate. The film thickness of the water pool over the test plate was measured by using the MTUPE system described above. The measurement results of the MTUPE system were compared quantitatively with the nominal thickness of the water pool in order to validate the MTUPE

measurement results as shown in Figure 2.4. A good agreement was achieved between the nominal water film thickness over the test plate and the measurement results of the MTUPE system.

2.5 Conclusions

In this study, a multi-transducer (sparse array) ultrasonic pulse-echo (MTUPE) technique was developed to measure the thickness of surface water film flow. The technical basis for the MTUPE technique was illustrated. A new method was developed to characterize the time-of-flight in the ultrasonic pulse-echo signal based on the auto-correlation algorithm. The factors that influence the measurements were discussed. The near field effect, beam spread effect, and interface reflection and transmission were described in detail for the MTUPE system in the present study. The measurement accuracy of the system was estimated to be ± 5 μm. To validate the new MTUPE technique, The measurement results of the MTUPE system were compared quantitatively with the nominal thickness of a water pool, in which a good agreement was achieved.

CHAPTER 3
QUANTIFICATION OF WIND-DRIVEN SURFACE WATER FILM FLOWS USING THE MTUPE TECHNIQUE

3.1 Introduction

Aircraft operating in cold clouds or precipitation face the risk of icing. The flight performance can be significantly affected when ice accretes on aircraft surfaces (Steuernagle et al. 2008). The in-flight ice morphology is dependent on weather conditions (Gent et al. 2000). Generally, rime ice forms at freezing temperatures (typically below -10°C) when aircraft encounter cloud with low liquid water content (LWC) and small water droplets. If the air temperature is just below the freezing point, glaze ice tends to form when aircraft go through the cloud with higher LWC and larger droplets. In rime ice accretion, the super-cooled droplets freeze immediately upon impact, which results in ice shapes conforming to the aircraft surfaces. In glaze ice accretion, however, the impinged droplets will deform and run back over the aircraft surfaces before freezing downstream (Hansman and Kirby 1987). The water run-back behavior redistributes the impinging water mass and disturbs the local flow field, and hence, makes the glaze icing process more complex and unpredictable (Du et al. 2010; Zhang et al. 2015).

To accurately predict glaze ice accretion, good modeling and simulations incorporating iterative computation of airflow, water droplet trajectories, collection efficiency, and heat and mass transfer process are required. However, due to the complexity in the coupled mass and heat transfer process, many simplifications were made in modeling glaze icing (Wright 1999), which essentially affects the prediction of final

glaze ice shapes(Fortin et al. 2006). More efforts in quantifying the physical processes in glaze icing are required to provide facts to help improve the prediction models. It is suggested that the surface water film transport behavior is one of the key factors that influences the morphology and growth of glaze ice (Du et al. 2010). Therefore, quantitative measurements of wind-driven surface water film flow are strongly desired to provide more fundamental physical details pertinent to the water transport behavior in glaze icing process.

In the present study, a multi-transducer (sparse array) ultrasonic pulse-echo (MTUPE) technique was used to measure the thin water film flow driven by boundary layer airflow. The MTUPE technique has the capability to resolve the thin water film structures and their time-evolutions. Based on the measured thickness data, the instantaneous wave patterns riding on the surface water film flow were characterized. The time series of the thickness profiles were then formulated to reconstruct the wave structures of the wind-driven water film flow in the space domain.

3.2 Experimental Setup and Test Model

The experimental study was conducted in a low-speed open circuit wind tunnel available at Aerospace Engineering Department of Iowa State University. The tunnel has a test section with optically transparent walls, which is 300mm × 200 mm × 140mm in length, width and height, respectively. The wind tunnel has a contraction section upstream of the test section with a set of honeycombs and screen structures installed ahead of the contraction section to provide uniform low turbulent airflow into the test section. The

turbulence intensity level in the test section of the wind tunnel was about 1.0 %, measured by using a hotwire anemometer.

Figure 3.1 shows the experimental setup used in the present study to quantify the transient behavior of wind-driven surface water film flows over a flat test plate by using the MTUPE technique described above. As shown in the figure, the flat test plate, which was designed to have 250 mm in length and 150 mm in width, is made of a hard plastic material by using a rapid prototyping machine (i.e., 3D printer). The upper surface of the test model was processed with fine sandpaper (i.e., up to 2000 grit) and special plastic polishes to achieve a very smooth, glossy finish. During the experiments, the test plate was flush-mounted to the bottom wall of the wind tunnel test section. Two side guide vanes with 4mm in height and rounded trailing edges were also designed at two sides of the test plate in order to reduce the edge effects to ensure uniform surface water film flows over the flat test plate.

As shown schematically in Figure 3.1, a row of 13 water injection holes with 2.0 mm in hole diameter were designed over the test plate at a distance of 25.4 mm away from the leading edge of the test plate. During the experiments, a digital gear pump (Cole-Parmer 75211-30) was used to drive water flow from a reservoir to go through the water injection holes to form surface water film flow over the test plate. The flow rate of the surface water film flow was controlled by adjusting the settings of the digital gear pump, and monitored by using a digital flowmeter (Omega FLR 1010 T-D). After injected from the water injection holes, the surface water film flow over the test plate would run back rapidly, as driven by the boundary layer airflow over the test plate. As the wind speed in the wind

tunnel becomes high enough (i.e., for the test cases with the freestream wind speed of $U_\infty \geq 10$ m/s), surface waves would be generated on the free surface of the water film flow at the downstream of the water injection holes.

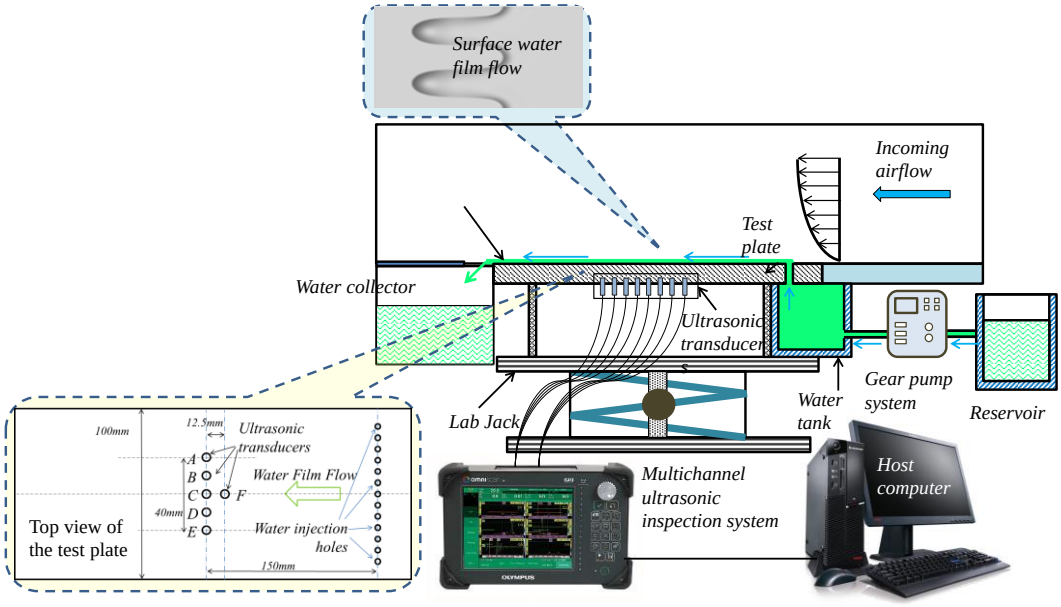

Figure 3.1 Experimental setup for the measurements of surface water film flow over a flat plate using MTUPE technique

In the present study, an array of 6 ultrasonic transducers, which were mounted at the backside of the flat test plate, were used to quantify the transient behavior of wind-driven surface water film flows over a flat test plate. The locations of the ultrasonic transducers were shown schematically in Figure 3.1. All of the transducers were connected to a multichannel inspection system (Omniscan iX), which was used to acquire measurement data with a pulse repetition frequency (PRF) of 1200 Hz.

3.3 Results and Discussions

3.3.1 Time-resolved Thickness Measurements of the Wind-driven Surface Water Film Flow

As described above, the MTUPE system is capable of providing time-resolved film thickness measurements at multiple points simultaneously to quantify the wind-driven surface water film flow over the test plate. Figure 3.2 shows typical measurement results of the MTUPE system in the term of the measured instantaneous film thickness at the center of the test plate (i.e., at point "C" shown in Figure 3.1) with freestream velocity of V_∞=10 m/s while the volumetric flow rate Q varies from 100 to 300 ml/min. The surface waves riding on the free surface of the water film flow was revealed quantitatively based on the time histories and the corresponding amplitude spectra of the measured film thickness of the wind-driven surface water film flow over the test plate.

As shown clearly in Figure 3.2 (a), with the freestream velocity of the airflow in the wind tunnel being kept constant at V_∞=10 m/s, there are periodical surface waves appeared in the wind-driven water film flow. When the volumetric flow rate was set at Q =100 ml/min, the surface of the water film was stable, and almost mirror-smooth. The only disturbances of the surface were the minute waves, which have a frequency of 4.92 Hz as indicated in the amplitude spectrum shown in Figure 3.2 (b). These minute waves were suggested to be caused by small fast-moving eddies in the turbulent air stream (Craik 1966). When the volumetric flow rate increased to 200 ml/min, along with the increase of film thickness, obvious sinusoidal waves appeared at the film surface with a frequency of 6.21 Hz as shown in Figure 3.2 (c). It has been demonstrated by Craik (1966) that the surface waves are essentially governed by the stresses exerted by the airflow upon the

water/air interface, with a normal stress in phase with the wave elevation and a tangential stress in phase with the wave slope. If the stresses are not sufficient to overcome the stiffness of the water film surface due to gravity and surface tension, the surface waves can be retained in a stable state. As we further increased the flow rate to 300 ml/min, the surface water film became thicker. More energy was transferred from the primary water flow to the interface disturbances. The surface waves developed into a pattern with steeper wave fronts, which are more like triangle waves with a frequency of 6.95 Hz (given in Figure 3.2 (d)), but were still in a stable state.

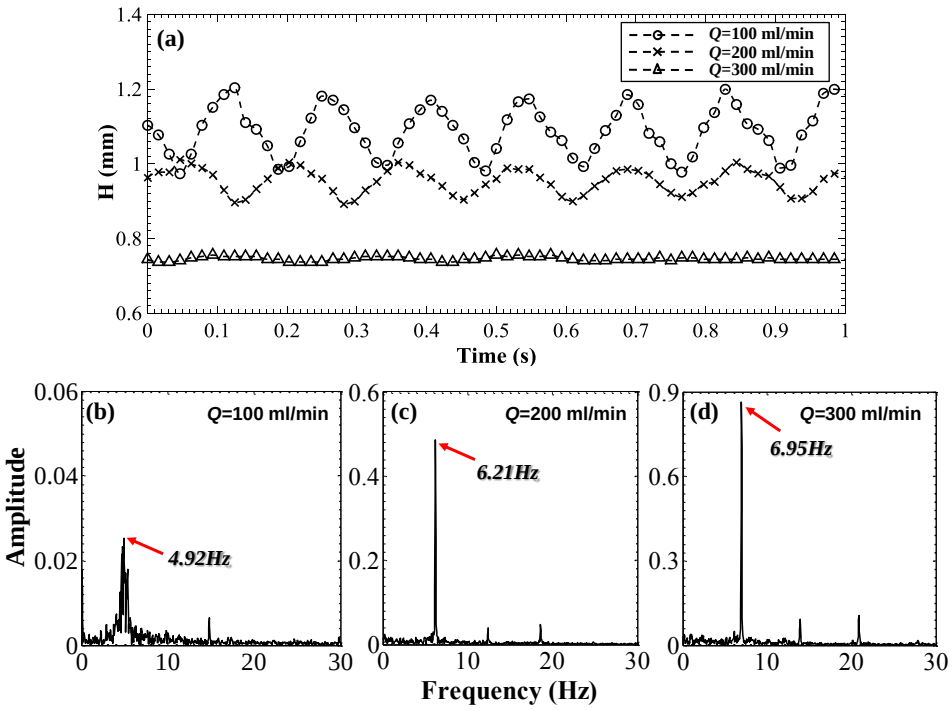

Figure 3.2 Time-resolved film thickness at the center of the test plate with freestream velocity of 10 m/s and volumetric flow rate of 100 to 300 ml/min. (a) Time histories of the water film thickness variation. (b-d) Amplitude spectra of the water film thickness variations at Q = 100, 200, and 300 ml/min.

Since the surface water film flow was horizontal, the motion was independent of gravity, and the film was subject to a uniform shear stress, with the velocity profile in the water film being nearly linear (Craik 1966). The mean velocity of the moving water film was half the surface velocity. Since the volumetric flow rate Q and the channel width w are known, the mean film thickness h can be measured in the present study, the surface velocity of the water film U can be found from the expression $U = 2Q/hw$. It is seen from the data listed in Table 3.1 that, the surface water film transports faster at higher volumetric flow rate. Since the velocity of the main airflow was kept constant, if the velocity profile within the water film is linear, the surface velocity of the water film may increase as the film extends further into the boundary layer airflow when the film thickens at higher volumetric flow rate.

Table 3.1 Characteristic Parameters of the Surface Water Film Flow

V_∞ (m/s)	Q (ml/min)	Mean thickness μ (mm)	Standard Deviation σ (mm)	Surface Velocity U (mm/s)
10	100	0.745	0.005	44.13
	200	0.960	0.040	68.49
	300	1.090	0.065	90.48
15	100	0.350	0.055	93.92
	200	0.365	0.065	180.13
	300	0.390	0.070	252.87
20	100	0.195	0.035	168.58
	200	0.210	0.050	313.08
	300	0.255	0.065	386.74

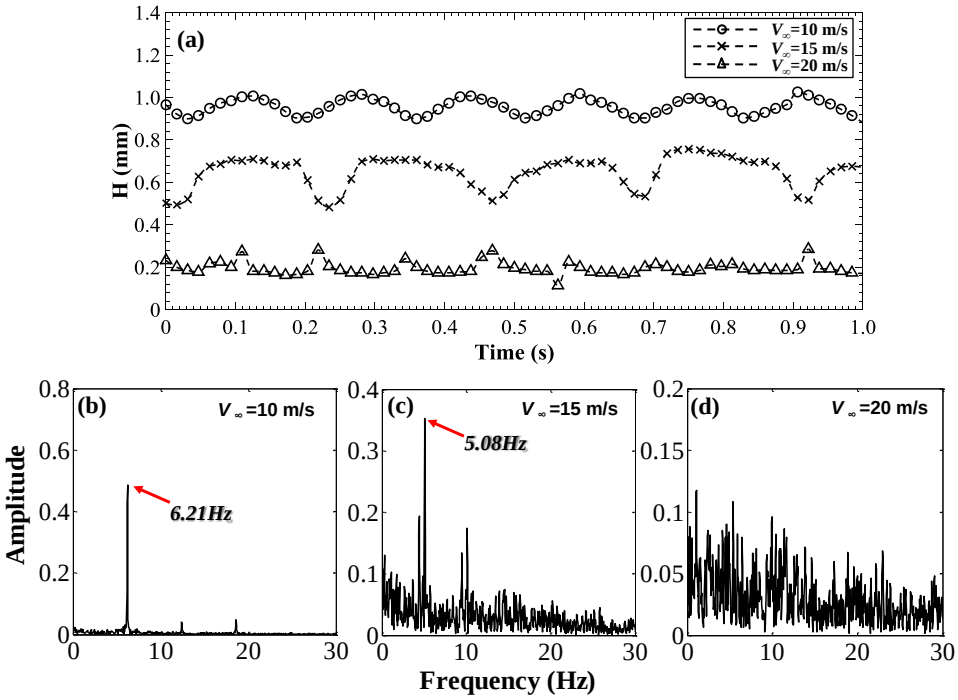

Figure 3.3 Time-resolved film thickness at the center of the test plate with freestream velocity of 10 to 20 m/s and volumetric flow rate of 200 ml/min. (a) Time histories of the water film thickness variation. (b-d) Amplitude spectra of the water film thickness variations at V_∞= 10, 15, and 20 m/s.

When the velocity of the main airflow increases, more energy is transferred from the main air stream to the interface disturbances. If the airflow velocity is sufficiently large, instability arises owing to the irreversible transfer of energy from the airflow to the surface disturbances in forms of various wave patterns (Cohen and Hanratty 1965). To evaluate the transition process of the interface stability as the airflow velocity increases, we look at the instantaneous time series of the water film thickness at the center of the test plate at a constant volumetric flow rate of 200 ml/min, while the freestream velocity varies from 10 to 20 m/s as shown in Figure 3.3 (a).

As described above, when the velocity of the main airflow was kept at 10 m/s, the surface water film flow was in a stable state with sinusoidal surface waves, which has a

clear dominant frequency of 6.21 Hz as shown in Figure 3.3 (b). When the airflow velocity was increased to 15 m/s, the water film became thinner due to the acceleration of the surface water. The surface waves turned into a pattern featured like a pulsed rectangular wave, having steep fronts and long rear portions, which has a frequency of 5.08 Hz as shown in Figure 3.3 (c). As we further increased the freestream velocity to 20 m/s, the surface waves were of an obviously non-periodic nature, with no dominant frequency being seen in the amplitude spectrum (Figure 3.3 (d)), which indicates the instability occurring at the water film surface.

As has been revealed by Ueno and Farzaneh (2011), the amplification rate of the disturbance can be significantly increased when the velocity of the main airflow increases. Since the turbulence intensity of the air stream is enhanced at higher airflow velocity, there is more random fluctuations of stress exist at the water surface. The interaction between the surface perturbations and the turbulent fluctuations in the airflow may give rise to a systematic surface stress (Craik 1966), which is a potential factor that triggers the interface instability. In the present study, we introduced a parameter called boundary slip factor (BSF), denoted by β, to evaluate the transition of surface stability of the water film flow. The BSF is defined as the ratio of the surface velocity of the water film flow and the freestream velocity of the airflow as expressed in Eq. (3.1).

$$\beta = \frac{2Q}{w \cdot \tilde{h} \cdot V_{\infty}} \tag{3.1}$$

Where Q is the water flow rate, w is the width of the surface water film flow, $\tilde{h}$ is the instantaneous thickness of the water film flow, and V_{∞} is the freestream velocity of the air flow.

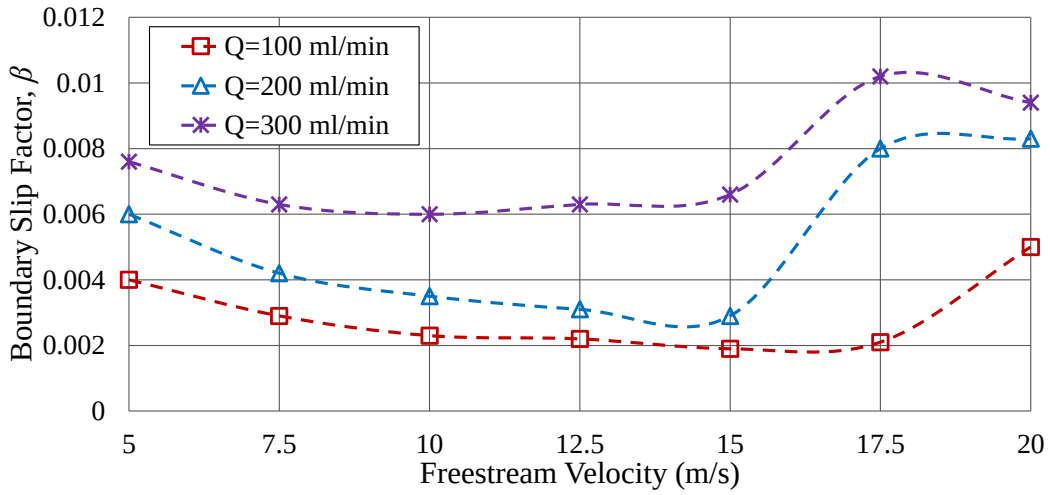

Figure 3.4 *Evolution of the time-averaged boundary slip factor (BSF) in the term of increasing freestream velocity of the air flow.*

Figure 3.4 shows the evolutions of the time-averaged BSF in the term of increasing freestream velocity at different volumetric flow rate. It is seen that at the flow rate of 100 ml/min, the BSF decreases as the freestream velocity increases from 5 to 15 m/s. Since the surface motion of the water film is driven by the stresses exerted by the boundary layer airflow, as the airflow velocity increases, the stresses at the interface will increase, and hence accelerate the surface water film flow. However, the acceleration of the film surface is not proportional to that of the main airflow due to the change of thickness of the water film. As the freestream velocity goes beyond 17.5 m/s, the surface instability occurred as indicated by the sudden increase of the BSF. It is because when the airflow velocity is sufficiently large, the stresses exerted by the airflow may overcome the restoring forces comprised of gravity and surface tension. The viscous dissipation is insufficient to balance the energy transfer to the corresponding neutral waves, due to which the stable surface wave system breaks and the surface velocity of the water film may increase dramatically.

At the volumetric flow rate of 200 and 300 ml/min, similar processes of the BSF evolutions are observed, with the value decreasing or being kept constant when the freestream velocity increases from 5 to 15 m/s, and a sudden increase occurring as the airflow velocity goes beyond 15 m/s. The instability of the water film surface occurred when the airflow velocity was sufficiently large, which is 15 m/s for the cases discussed here. It can be found that as the instability occurs, the surface water transports much faster, and another type of surface waves may form, which contributes to a larger BSF as indicated in the figure.

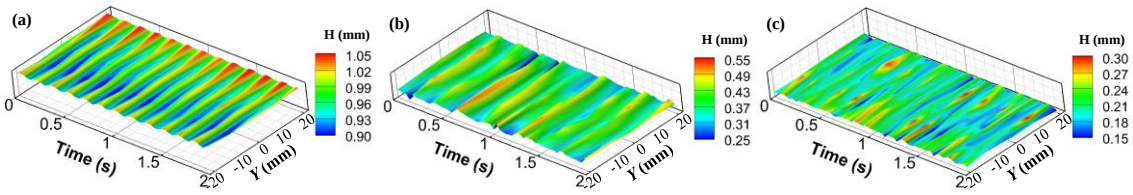

Figure 3.5 Time expansions of the span-wise thickness profiles of the surface water film flow at the volumetric flow rate of 200 ml/min while the freestream velocity varies at (a) V_∞*=10 m/s, (b)* V_∞*=15 m/s, and (c)* V_∞*=20 m/s*

To further evaluate the surface wave characteristics during the instability transition, five transducers were aligned spanning the surface water film flow, i.e., point A, B, C, D, and E as shown in Figure 3.1, to provide simultaneous measurements of the surface water film thickness at multiple sites in transverse. The time evolutions of the span-wise thickness profiles of the surface water film flow at the volumetric flow rate of 200 ml/min, and under different freestream velocities (i.e., (a) V_∞=10 m/s, (b) V_∞=15 m/s, and (c) V_∞=20 m/s) are shown in Figure 3.5.

It is clearly shown that when the water flow rate was kept constant, the most obvious effect of increasing the airflow velocity was to decrease the water film thickness. As the

freestream velocity increases from 10 to 20 m/s, the mean value of the film thickness decreases from 0.96 to 0.21 mm as listed in Table 3.1. Due to the change of thickness in the surface water film, the liquid Reynolds number in the water film flow changes and the viscous dissipation within the film can be significantly affected (Cohen and Hanratty 1965). In the meantime, the stresses exerted by the airflow on the water film surface will increase when the airflow velocity increases, which essentially enhances the interaction between the surface perturbations in the water film and the turbulent fluctuations in the airflow. At the airflow velocity of 10 m/s, the sinusoidal surface waves can be seen as shown in Figure 3.5 (a), which are similar to the 'fast' waves that were observed in Craik's experiments (Craik 1966). As has been mentioned above, the surface water film flow in this case was in a stable state. The shear stresses were uniformly distributed in span-wise, and the surface water film flow was a typical two-dimensional flow with periodical surface waves.

When the freestream velocity was increased to V_∞=15 m/s, the film thickness decreased while the turbulence intensity in the boundary layer airflow was enhanced. More energy was transferred from the airflow to the surface disturbances, which generated the surface waves with steeper fronts and longer rear portions as shown in Figure 3.5 (b). It is clear that the surface waves in this case were still two-dimensional. The surface water film flow was still in a stable state. As the airflow velocity was further increased to 20 m/s, the surface waves were no longer two-dimensional, but of an obviously non-periodic nature, having pebbled wave structures as shown in Figure 3.5 (c). The surface water film

flow with wave-like disturbances became unstable due to the irreversible transfer of energy from the airflow to the surface disturbances (Cohen and Hanratty 1965).

3.3.2 Reconstruction of Spatial Wave Structures in the Wind-driven Surface Water Film Flow

In the present study, we also made effort to reconstruct the temporally-resolved surface wave structures to evaluate the surface wave behaviors in the wind-driven water film flow. To achieve that, the velocity of the surface waves was first quantified, so that we can transform the time-series of the surface waves into spatial wave structures based on Taylor's hypothesis (Taylor 1938).

When we consider the determination of velocity, a simple but typical methodology is $c = l/\tau$, where l is the distance between two points, τ is the travel time between the two points, and c is the velocity of wave features traveling over the two points. In this study, two monitoring points were set along the flow direction with a separation of 12.5 mm. The time-series of the surface waves at the two points were recorded simultaneously. The velocity of the surface waves was determined by finding the time delay between the two wave series at the two points.

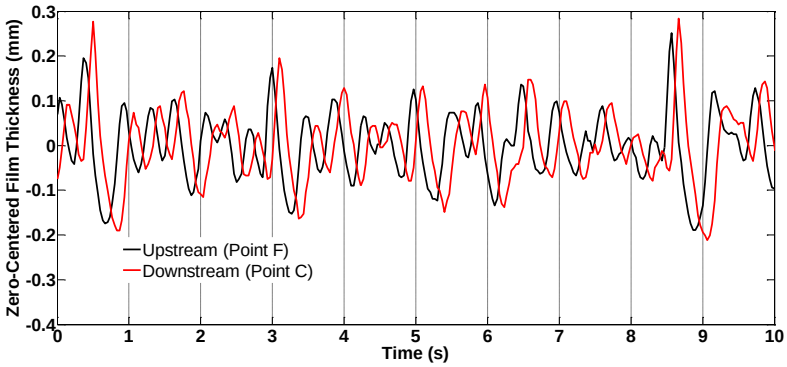

Figure 3.6 Comparison of the thickness profiles at the upstream and downstream center points with a separation of 12.5 mm.

The two points selected for the velocity determination are point F (upstream point) and C (downstream point) as shown in Figure 3.1. The zero-centered time-series of the surface waves (e.g., at V_∞ = 15 m/s and Q = 100 ml/min) recorded at the two monitoring points are shown in Figure 3.6. It is seen that the two wave series are obviously of the same features but with a phase shift. The phase delay between the two wave-series was obtained by performing an auto-correlation of the upstream wave series and a cross-correlation between the upstream and downstream wave series using Eq. (3.2) and (3.3) (Smith 1997), respectively.

$$R_{Auto}(\tau) = E\left[\left(H_{up}(t+\tau) - \mu_{H_{up}}\right)\left(H_{up}(t) - \mu_{H_{up}}\right)\right] \Big/ \sigma^2_{H_{up}} \tag{3.2}$$

$$R_{Cross}(\tau) = E\left[\left(H_{up}(t+\tau) - \mu_{H_{up}}\right)\left(H_{down}(t) - \mu_{H_{down}}\right)\right] \Big/ \sigma_{H_{up}}\sigma_{H_{down}} \tag{3.3}$$

where $R(\tau)$ is the correlation coefficient that varies with time lag τ.

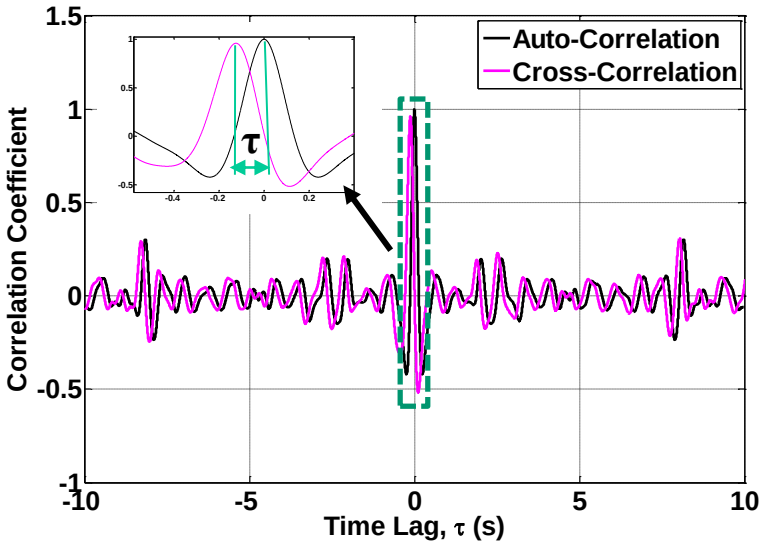

Figure 3.7 Autocorrelation function of the upstream wave series and cross-correlation function of upstream and downstream wave series.

The auto-correlation function of the upstream wave series and the cross-correlation function of upstream and downstream wave series are shown in Figure 3.7. For each correlation function, there is a maximum correlation coefficient. By comparing the time lag between the two maximum correlations, the phase delay between the two wave series was acquired with a value of 0.124 s, for example in this case. The time-averaged surface wave velocity was then calculated to be 81.30 mm/s

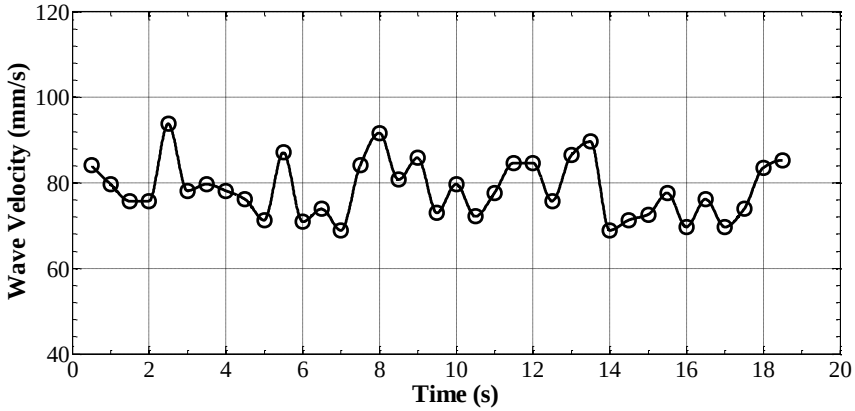

Figure 3.8 Velocity fluctuation of surface wave features in the water film flow.

When we applied the methodology using gated segments (with a length of 1.0 s) . The time-series of the surface wave velocity was obtained as shown in Figure 3.8. The wave velocity in this case was therefore determined to be 81.30±6.55 mm/s.

The temporal wave series can be transformed into the space domain by multiplying the wave velocity. This temporal-to-spatial operation was developed based on Taylor's frozen flow hypothesis (Taylor 1938), which stated that if the turbulence intensity is small compared to the mean flow velocity, the temporal response at a fixed point in space can be regarded as the result of an unchanging spatial pattern convecting uniformly past the point at the mean flow velocity (Moin 2009). In this case, the ratio of the velocity

fluctuating magnitude and the mean velocity was calculated to be 0.08, i.e., $\sigma_u/\mathbf{U} << 1$, which satisfies the criteria proposed by Willis and Deardorff (1976).

Taylor's hypothesis assumes that the time-space transformation is linear:

$$R(r,\tau) = R(r - U\tau, 0) \tag{3.4}$$

which can be further transformed to relate the time-correlation and space-correlation:

$$R(0,\tau) = R(-U\tau, 0) \tag{3.5}$$

Therefore, the spatial distribution can be constructed simply using Eq. (3.6).

$$dx = -\mathrm{U} \cdot dt \tag{3.6}$$

where U is the mean flow velocity.

Suppose the stream-wise location of the transducer array (point A ~ E) is at $x = x_0$. To reconstruct the flow structures at $t = t_0$, we first calculated the time required for the wave features to travel over the wave zone: $t_s = w/c$. Then the stream-wise coordinates were generated using Eq. (3.7).

$$x_i = x_0 + i \cdot \Delta t \cdot c \quad \left(i \cdot \Delta t \le t_s\right) \tag{3.7}$$

Then, the spatial thickness distribution can be expanded using Eq. (3.8) and (3.9).

$$H\left[x_0, y_i\right] = H\left(t_0, y_i\right) \tag{3.8}$$

$$H\left[x_i, y_i\right] = H\left[\left(x_0 + i \cdot \Delta t \cdot c\right), y_i\right] = H\left(t_0 - i \cdot \Delta t, y_i\right) \tag{3.9}$$

A schematic of the temporal-to-spatial thickness transformation process is shown in Figure 3.9. At $t = t_n$, the thickness at the transducer array location ($x = x_0$) is the thickness at $t = t_n$ in time series. The thickness at the *ith* spatial position is defined as the thickness at $t_i = t_n - i \cdot \Delta t$ in time series, where $i \leqslant t_s/\Delta t$. Thus, the spatial thickness distribution in the wave zone at $t = t_n$ can be established.

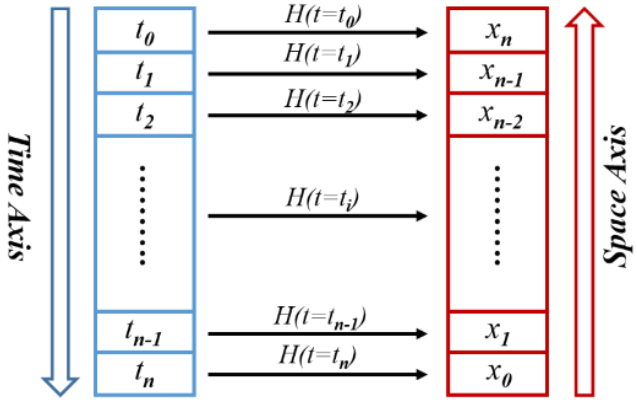

Figure 3.9 A schematic of the temporal-to-spatial thickness transformation.

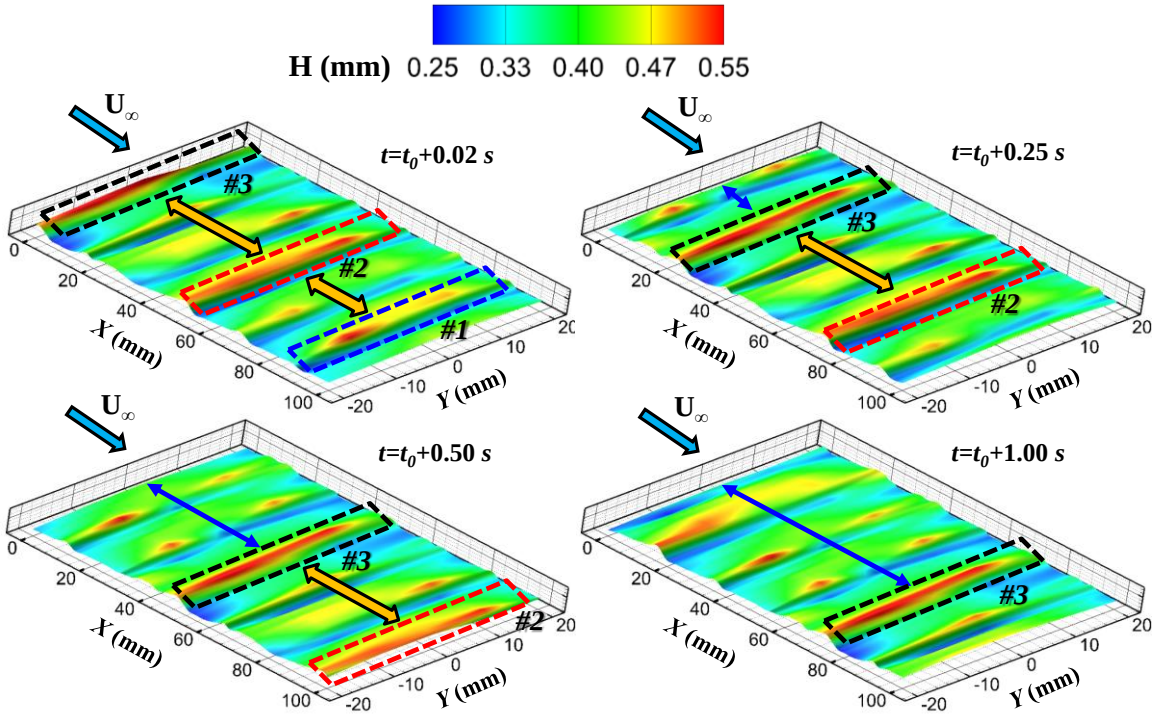

Figure 3.10 Time-resolved spatial flow structures at a wind speed of 15 m/s and water supply rate of 100 ml/min.

If we apply the above methodology along the time axis, the time-resolved spatial structures of the surface water film flow can be obtained. The spatial flow structures at a wind speed of 15 m/s and water flow rate of 200 ml/min at different times are shown in

Figure 3.10. The time evolution of the surface wave features can be clearly observed. At $t=t_0+0.02$ s, we numbered three obvious wave peaks, with the #1 wave at X = 89 mm, the #2 wave at X = 51 mm, and the #3 wave at X = 0 mm. As time goes on, the two-dimensional wave features move downstream. At $t=t_0+0.25$ s, the #1 wave moves out of the view, while the #2 and #3 waves advance to X = 73 mm and 21 mm, respectively. After 0.25 s, the #2 wave moves to the end of the view (i.e., X = 100 mm), while the #3 wave arrives at X = 43 mm. At $t=t_0+1.00$ s, the #2 wave is no longer in the view, and the #3 wave is located at X = 81 mm. Therefore, by the means developed in this study, more details can be quantitatively resolved in the term of the time evolutions of the surface wave structures in the wind-driven water film flow.

3.4 Conclusions

An multi-transducer (sparse array) ultrasonic pulse-echo (MTUPE) technique was developed to quantify the transient surface behaviors of the water film flow driven by boundary layer airflow. The instantaneous surface waves riding on the free surface of the water film flow were characterized based on the measured time series of the film thickness. Surface waves of various patterns (e.g., sinusoidal wave and triangular wave) were revealed as the water film flow was kept in a stable state. At a specific airflow velocity where the surface stability can be retained, the surface velocity of the water film was found to increase as the film thickness increases, while more energy was transferred from the liquid flow to the surface disturbances in various wave patterns.

The instability transition of the wind-driven water film flow was examined by increasing the freestream velocity while the volumetric flow rate was kept constant. The

instability was found to occur when the stresses exerted by the airflow overcome the restoring forces in the water film. The occurring of the instability can be indicated by the boundary slip factor (BSF) as defined in the present study. Based on the time expansions of the measured thickness profiles of the surface water film flow, the surface wave features during the instability transition were revealed. A transition from periodical two-dimensional waves to pebbled waves of an obviously non-periodic nature was observed when instability of the film surface occurred.

In the present study, a methodology, based on the use of MTUPE technique, was also developed to reconstruct the temporally-resolved spatial wave structures in the wind-driven water film flow. It would appear that there is potential to implement such system and method for real-time water/ice detection on aircraft which could then provide more details of surface morphologies and evolutions of the surface waves in wind-driven water films.

CHAPTER 4
A ULTRASONIC-BASED STRATEGY FOR ICE CHARACTERIZATION PERTINENT TO AIRCRAFT ICING PHENOMENA

4.1 Introduction

Aircraft icing has been considered as one of the most serious hazards to impact flight safety since early in the development of aviation (Smith 1929). Ice accretion can destroy the smooth airflow over lift and control surfaces which decreases the ability of aircraft to generate lift (Steuernagle et al. 2008). Additionally, the uncontrolled shedding of ice which has built up on aircraft surfaces may severely damage aircraft components (Bassey and Simpson 2007). From an economic perspective, ice accretion can increase the costs of flight operations due to the use of anti/de-icing equipment and fluid. An investigation by the National Business Aviation Association (NBAA) found that the cost of removing heavy wet snow from a medium-sized business jet is about $3,000, while that for the removal of frozen/freezing rain can be up to $10,000. Moreover, the time spent in performing de-icing procedures can cause flight delays or even cancellations, which can then significantly impact airline performance, and hence total operation costs (Caliskan and Hajiyev 2013)

The morphology of ice accretion on aircraft surface is determined by weather conditions (Gent et al. 2000). For example, if the air temperature is very low (typically below -10°C), when an aircraft encounters cloud with low liquid water content (LWC) and small water droplets, rime ice will form as the super-cooled droplets freeze and accumulate upon impact. Such rime ice appears to be white and opaque and it is formed

containing many micro bubbles and cracks (Hansman and Kirby 1987). If the air temperature is just below the freezing point, glaze ice tends to form, especially when an aircraft goes through cloud with a higher LWC and larger droplets. In the case of glaze ice accretion, the impinged droplets will deform and run back over the aircraft surfaces as liquid before freezing downstream. Glaze ice appears to be smooth, clear, and dense, and it forms on the leading edge of airfoils with horn-like shapes that project into the airflow (Hansman and Kirby 1987). Due to the different physical mechanisms which occur in the two icing processes, rime ice generally conforms to the shape of aircraft surfaces, and it therefore has a smaller effect on aircraft performance, while glaze ice forms and covers more surfaces and has a more severe effect on the flight performance of aircraft.

To reduce the potential harmful effects of aircraft icing, many anti/de-icing systems have been developed. These can be considered in three groups and are in the form of freezing point depressants, thermal melting, and surface deformation (Thomas et al. 1996). With these various anti/de-icing approaches, the amount and the rate of ice removal is mainly determined by the volume of de-icing fluid or electrical power applied. For rime ice accretion, due to the porous nature of the structures in ice layers and typically the smaller area on the aircraft surfaces on which it forms, it is easier to remove, when compared with glaze ice, which is denser and typically has a higher adhesion to aircraft surfaces. Glaze ice usually extends further downstream on a wing surface and typically covers a larger area. Therefore, more de-icing fluid or power is required to remove glaze ice accretion (Thomas et al. 1996). In looking at performance optimization, most of the current de-icing systems were however, developed without considering the characteristics

of the accreted ice. During flight operations, the de-icing systems are usually implemented using the same process and strategies, regardless of the ice type. As a result in operation, a lot of potentially unnecessary actions are performed to ensure effective removal of ice on aircraft surfaces (Gao and Rose 2009; Zou et al. 2013). In looking to improve winter flight operational performance, methods and techniques for ice detection and characterization are needed that can potentially improve and optimize de-icing.

To address this need, many ice detection and monitoring techniques have been investigated which use either direct or indirect measurement approaches. Most of the direct measurement approaches provide icing warnings with data from measuring surface properties of aircraft with changes in mass, reflective index, electrical/thermal conductivity, dielectric coefficient, or inductance. Indirect measurement approaches, however, detect icing events based on monitoring flight performance metrics, such as a lift decrease or drag increase, or from measurements of weather conditions, such as air humidity and temperature (Homola et al. 2006; Caliskan and Hajiyev 2013).

As ice forms on aircraft surfaces, the flight performance can be affected very quickly. Therefore, for safety reasons, direct methods for ice detection are generally preferred. Among the measurement methods are those which use ultrasonic techniques and these have been widely studied and applied (Gao and Rose 2009). As reported by Hansman and Kirby (Hansman and Kirby 1986), an ultrasonic pulse-echo technique was developed to provide real-time thickness measurements of water/ice accretion. The water/ice layers were characterized using ultrasonic echoes where signals were generated at interfaces. In laboratory studies, such interface reflections were displayed on an oscilloscope. In recent

years, ice detection and classification have been achieved by using the ultrasonic guided-wave technologies, in which the ice types were classified based on the dispersion characteristics of the phase and group velocity curves for waves in the multi-layer system (Vellekoop et al. 1999; Hongerholt et al. 2002; Gao and Rose 2009).

In terms of implementations on aircraft, various ultrasonic transducers and systems have been fabricated to provide in-situ ice detection. One example of a recent implement was that provided by Liu et al. (2008) who developed two types of flexible ultrasonic sensors that were used to monitor in-situ structural thickness and ice build-up. These transducers were easily attached on the inside of the curved airfoil surfaces on aircraft.

To further extend the capability of ice detection and characterization with ultrasonic techniques, new approaches are required to more quantitatively characterize the types, and thickness, of ice that forms on aircraft. In looking to better understand the properties and structures of ice, the attenuation characteristics of ultrasonic waves have been widely used (Abbasi et al. 2011; Gudra and Najwer 2011). In the present study, two different classes of ice morphology were characterized based on attenuation of ultrasonic waves, in a pulse-echo configuration, which is extended from a feasibility study with preliminary data presented (Liu et al. 2014). The acoustic velocities in the two ice types were also measured, and compared with data in the literature. The feasibility study then considered the frequency-dependent ultrasonic attenuation for two typical ice samples representing rime and glaze ice.

4.2 Theories of Ultrasonic Attenuation in Pulse-Echo Field

In a typical ultrasonic pulse-echo measurement, the ultrasonic pulse is first emitted into the object being investigated using a transducer. If the object is comprised of multiple layers with different acoustic impedances, the ultrasonic waves will be partially transmitted/reflected at each of the layer interfaces. The reflected waves, i.e., echoes, will be detected by the same transducer, and measured as a voltage-time signal. Such ultrasonic pulse-echo measurements are commonly used in ultrasonic thickness gages, in which the material thickness is measured by determining the time interval between the various waves reflected from the interfaces (Svilainis 2012).

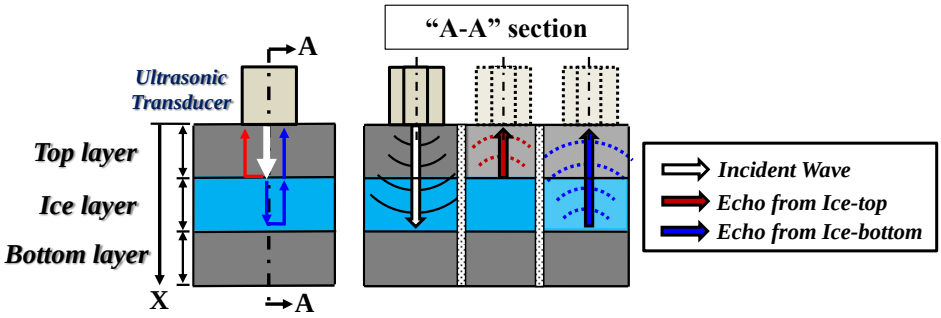

Figure 4.1 Schematic of the ultrasonic pulse-echo paths in a multi-layer object

When ultrasonic wave travels through a medium, its intensity diminishes with distance. In a non-attenuating ideal material, the wave amplitude is only reduced by the beam spread. In real materials, however, the wave is also reduced in amplitude by scattering and absorption. The combined effects of scattering and absorption cause what is known as attenuation (Schmerr 1998). Ultrasonic attenuation is defined as the decay of wave amplitude as it propagates through a material. In the present study, ice samples with different internal morphology were characterized using a ultrasonic pulse-echo method,

where the ultrasonic attenuation is expected to vary due to differences in the ice crystal structure and the porosity which cause scattering.

A schematic of the propagation paths of ultrasonic waves in pulse-echo in a multi-layer object is shown in Figure 4.1. In this multi-layer model, the top and bottom layers are made of the same material, while the sample layer being measured, which in this case is the ice, is sandwiched between these plates. As the ultrasonic waves travel through the top layer, a fraction of the energy is reflected at the first interface (i.e., ice-top interface), while the remainder is transmitted into the ice and then partially reflected at the second interface (i.e., ice-bottom interface).

The ultrasonic waves traveling in the multi-layer model can be described by the basic equation (Eq. (4.1)) for a progressive wave (Ensminger and Bond 2011).

$$A = A_0 e^{-\alpha x} \cos\left(kx - \omega t\right) \tag{4.1}$$

where A is the amplitude of the ultrasonic wave at coordinate x; A_0 is the amplitude of the ultrasonic wave at the origin (x=0); α is the attenuation coefficient; k is the propagation constant ($k=2\pi/\lambda=\omega/c$); ω is the angular frequency ($\omega=2\pi f$); and c is the phase velocity in the propagation medium.

For a conventional ultrasonic transducer, the ultrasonic pulse is a superposition of harmonic waves with many different frequencies and it can be expressed as shown in Eq. (4.2) (Ensminger and Bond 2011):

$$u\left(x,t\right) = \frac{1}{2\pi}\int_{-\infty}^{\infty} F_0\left(\omega\right) e^{-\alpha x} \cos\left(kx - \omega t\right) d\omega \tag{4.2}$$

where $F_0(\omega)$ is the Fourier transform of $u(0, t)$.

The signal that is measured for the reflected waves is a combination of the pressure signals that are, in effect, convolved, with the transducer and electronics characteristics, the reflection and transmission at interfaces, as well as the beam spread. Therefore, to describe the measured ultrasonic pulse-echo waves, additional terms need to be added, and these are given in Eq. (4.3):

$$u_n = \frac{1}{2\pi}\int_{-\infty}^{\infty}\left[\beta(\omega)\cdot R\cdot T\cdot C_n(\omega)\cdot F_0(\omega)e^{-\alpha x}\right]e^{-j\omega t}d\omega \tag{4.3}$$

where $\beta(\omega)$ is the system efficiency factor, R and T are the reflection and transmission coefficients at the interfaces, and $C_n(\omega)$ describes the effects of beam spread.

The ultrasonic attenuation in the ice layer was derived by comparing the amplitude spectra of the primary echoes (i.e., the first echoes in time sequence) that are reflected from the ice-top and bottom interfaces. The Fourier transform of u_n can be expressed in the form given as Eq. (4.4).

$$B(u_n) = B(\omega) = B(f) = \beta(\omega)\cdot R\cdot T\cdot C_n(\omega)\cdot F_0(\omega)e^{-\alpha x} \tag{4.4}$$

If the thickness of the top layer is d, the amplitude spectrum of the primary echo from the ice-top interface can be written as:

$$B_0(f) = \beta(f)T_{01}R_{12}T_{10}C(2d, f)F_0(f)e^{-2\alpha_0 d} \tag{4.5}$$

where T_{01} and T_{10} are the transmission coefficients when the ultrasonic waves travel through the ice-top interface; R_{12} is the reflection coefficient at the ice-top interface; $C(2d, f)$ is the beam diffraction correction term in the top layer; and α_0 is the ultrasonic attenuation coefficient in the top layer.

To formulate the amplitude spectrum of the primary echo from the ice-bottom interface, the diffraction term was first calculated using an equivalent path length z, which

is equal to the summation of the actual path length in the top layer and the equivalent path length of the ice layer in the top layer, which is given as Eq. (4.6):

$$2z = 2d + \frac{V_{ice}}{V_1} 2h \tag{4.6}$$

where U_{ice} and U_1 are the sound velocities in the ice layer and top layer; h is the thickness of the ice layer. Therefore, the amplitude of the primary echo from the ice-bottom interface can be derived and this is shown as Eq. (4.7):

$$B_1(f) = \beta(f) T_{01} T_{12} R_{23} T_{21} T_{10} C(2z, f) F_0(f) e^{-2\alpha_0 d} e^{-2\alpha_1 h} \tag{4.7}$$

where T_{12} and T_{21} are the transmission coefficients when the ultrasonic waves travel forwards and backwards through the ice-bottom interface; R_{23} is the reflection coefficient at the ice-bottom interface. $C(2z, f)$ is the equivalent beam diffraction for the primary echo from the ice-bottom interface; $\alpha_1(f)$ is the ultrasonic attenuation coefficient in the ice layer. The reflection coefficients at the ice-top and -bottom interfaces are given as Eqns. (4.8) and (4.9):

$$R_1 = R_{12} = R_{21} = \left| \frac{Z_{ice} - Z_1}{Z_1 + Z_{ice}} \right| \tag{4.8}$$

$$R_2 = R_{23} = R_{32} = \left| \frac{Z_2 - Z_{ice}}{Z_{ice} + Z_2} \right| \tag{4.9}$$

where Z_1 and Z_2 are the acoustic impedances of the top and bottom layers; Z_{ice} is the acoustic impedance of the ice layer, The relationships between the transmission coefficient and reflection coefficient at the two interfaces are given as Eqns. (4.10) and (4.11):

$$T_{01} \cdot T_{10} = 1 - R_0^2 \tag{4.10}$$

$$T_{12} \cdot T_{21} = 1 - R_1^2 \tag{4.11}$$

The beam diffraction correction term has been derived and evaluated in many studies. Here, an exact expression for the Lommel diffraction correction integral derived by Rogers and Van Buren (1974) was applied and this is in the form shown as Eq. (4.12).

$$C = 1 - e^{-(2\pi/s)i}\left[J_0(2\pi/s) + iJ_1(2\pi/s)\right] \tag{4.12}$$

where $s=2\pi z/ka^2$; $k=\omega/V$; $\omega=2\pi f$; J_0 and J_1 are Bessel functions of the first kind; and a is the radius of the circular piston source; and a is the radius of the circular piston source. The magnitude of the diffraction correction is usually given in a simple form:

$$|C| = \left\{ \begin{matrix} \left[\cos(2\pi/s) - J_0(2\pi/s)\right]^2 \\ +\left[\sin(2\pi/s) - J_1(2\pi/s)\right]^2 \end{matrix} \right\}^{1/2} \tag{4.13}$$

The correction terms are used in the amplitude spectrum equations (Eqns. 4.5 and 4.7). By comparing the two frequency-dependent amplitude spectra (Eq. 4.14), the ultrasonic attenuation in the sample layer, which in this case is ice, can be derived and is given in Eq. (4.15):

$$\frac{B_0(f)}{B_1(f)} = \frac{R_1}{\left(1-R_1^2\right)R_2}\frac{C(2d,f)}{C(2z,f)}e^{2\alpha_1 h} \tag{4.14}$$

$$\alpha_1(f) = \frac{1}{2h}\left[\ln\frac{B_0(f)}{B_1(f)} - \ln\frac{C(2d,f)}{C(2z,f)} - \ln\frac{R_1}{\left(1-R_1^2\right)R_2}\right] \tag{4.15}$$

In the present study, the time domain response of the echoes from the ice-top and -bottom interfaces were measured using an ultrasonic pulse-echo technique. The amplitude spectra of the echo waves were calculated by using a Fast Fourier Transform (FFT). Since the correction terms have been quantitatively evaluated, the frequency-dependent ultrasonic attenuation coefficient can be calculated.

4.3 Experimental Evidence

4.3.1 Experimental Setup for the Attenuation Measurements

A schematic of the experimental setup for the attenuation measurements with an ultrasonic pulse-echo method is shown in Figure 4.2. In the present study, two well-polished aluminum plates were used as the top and bottom layers, while the measured layer was deposited in between the two plates. The top- and bottom-plates were fixed so as to be parallel and placed within a low-temperature resistant plastic tank, in which various materials can be deposited (e.g., water, ice). The ultrasonic transducer, with element diameter of 3.175 mm (0.125 inches) and nominal center frequency of 10 MHz, was attached to the top-plate, and connected to the pulser/receiver as shown in the figure. The pulser/receiver was a modified commercial ultrasonic inspection unit (Omniscan iX), which has a sampling frequency of 100 MHz. While the pulser/receiver was used to generate and receive pulse-echo signals, a host computer was used to control the measurements, collect and process the pulse-echo signals.

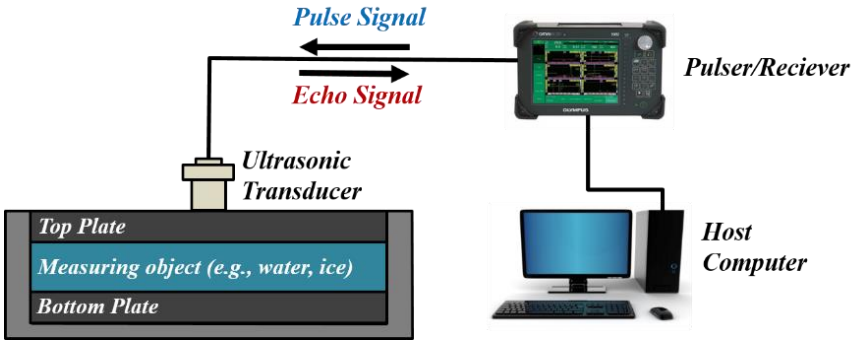

Figure 4.2 Experimental setup for the attenuation measurement with the ultrasonic pulse-echo method.

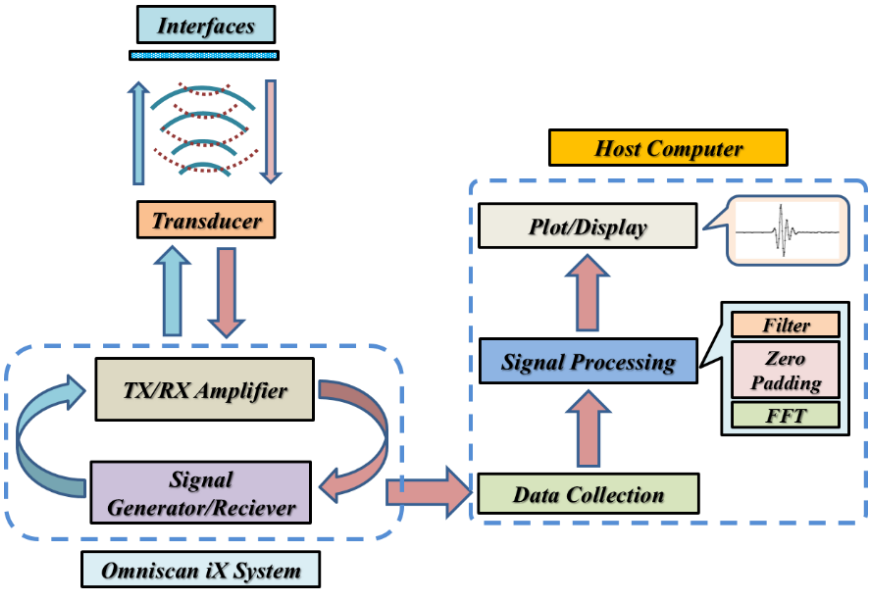

Figure 4.3 Schematic of the ultrasonic pulse-echo measurement system.

The integration of the ultrasonic transducer, pulser/receiver, and host computer forms a typical ultrasonic pulse-echo system, which is further illustrated in Figure 4.3. The Omniscan iX unit is designed to operate with a phased array and was modified so as to be capable of generating, amplifying and sending voltage pulses to multiple discrete ultrasonic transducers. With the high voltage excitation, the transducer will emit ultrasonic pulses into the test sample. As the pulses arrive at interfaces, they are partially reflected and signals are received by the transducer. The echo signal is received, amplified and digitized in the Omniscan iX unit. Semi-custom software is used to control the system functions, the signal generation, data collection and processing in the host computer.

4.3.2 Validation of the Ultrasonic Attenuation Model

To validate the theoretical model for calculation of the ultrasonic attenuation in the multi-layer object, data for determining ultrasonic attenuation in water was first collected, processed, and examined. The plastic tank was filled with distilled water at room

temperature. The methodology developed in this study, for determining the ultrasonic attenuation, was then applied to the sequence of echo signals.

The data for ultrasonic attenuation in water (at room temperature), as a function of frequency is shown as Figure 4.4. The proposed methodology, as well as software implementation was validated by comparing the results from the present experiments with the data for ultrasonic attenuation in water (at room temperature) previously reported by Krautkrämer (1990). It is seen that there is good agreement with attenuation based on fundamental physical constants.

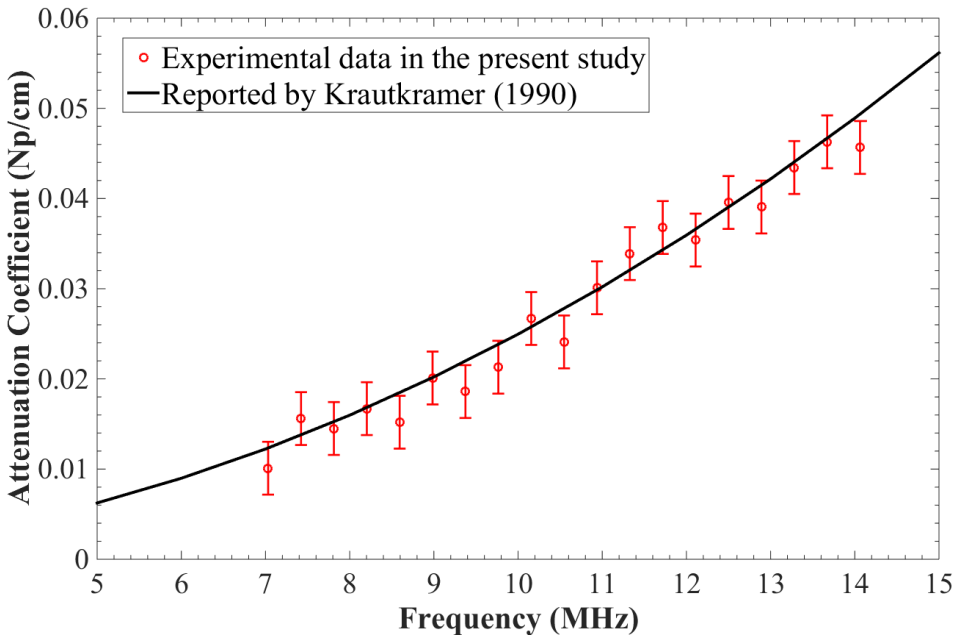

Figure 4.4 Comparison of the present experimental data and the result reported by Krautkramer (1990).

The measurement accuracy in the present work was mainly limited by the digitizing resolution in the ultrasonic pulse-echo system. Based on the uncertainty analysis, the attenuation measurement accuracy was estimated to be ±0.003 Np/cm and there was a correlation coefficient of 98% between the data sets.

4.3.3 Ultrasonic Attenuation in Ice Samples

4.3.3.1 Ice Sample Preparation

The two forms of ice are rime and glaze ice that are seen with in-flight ice accretions on aircraft. These ice forms have been described in qualitative terms in a number of publications (Hansman and Kirby 1987; Steuernagle et al. 2008; Potapczuk 2013). When forming on an aircraft, the ice structure is essentially determined by size of water droplets , ambient temperature, and the thermal conductivity of the substrate. In actual in-flight conditions, rime ice generally forms when small droplets impinge on a freezing cold surface (typically below -10 C°), and glaze ice forms when large droplets impinge on surfaces at temperatures just below the freezing point. Due to the different icing mechanisms, the appearances of the two ice morphologies are very different. Rime ice appears to be white and opaque, containing many air bubbles and ice grains, while glaze ice is transparent, clear, and dense.

To provide ice samples for measurements, a process was developed to give rime-like and glaze-like ice. A series of water distillation and forced freezing procedures were developed to prepare samples that are, at least in qualitative terms, similar to those previously reported (Hansman and Kirby 1985) for rime and glaze ice.

To prepare the rime-like ice sample, the plastic tank with the fixed aluminum plates was placed in a refrigerator with the temperature set below -10 ºC while water was chilled to near 0 ºC. When the aluminum plates were chilled to below -10 C°, and the near zero-degree water was sprayed onto the bottom plate. It was found that as the droplets impacting on the aluminum surface, they froze immediately. Small ice particles formed and built up

between the plates. An ice layer containing many air bubbles and ice grains formed as shown in Figure 4.5 (a).

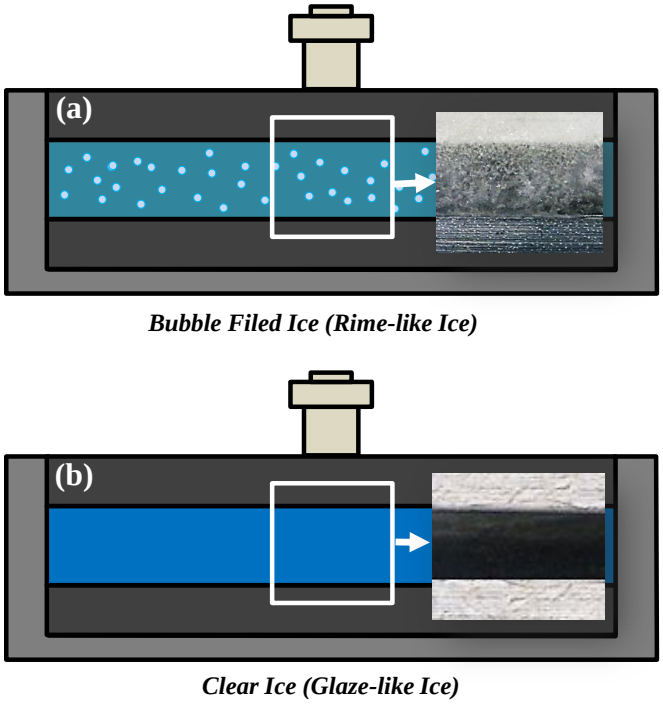

Figure 4.5 Laboratory prepared ice samples representing rime and glaze ice structures.

To prepare a glaze-like ice sample, water was first double-boiled to eliminate dissolved air. The sample was permitted to cool between boiling and an interval of 30 minutes was left between the boiling operations. The double boiled water was then slowly added into the plastic tank to fill the gap between the top and bottom aluminum plates. The tank was then placed in the refrigerator with temperature set at -5 ºC. A clear dense ice layer gradually formed with no observable bubbles or cracks trapped inside as shown in Figure 4.5 (b).

4.3.3.2 Acoustic Velocity in Ice samples

To enable calculation of the wave reflection coefficient (Eqns. 8 and 9) at interfaces, it is necessary to first evaluate the acoustic velocity and impedance in the ice samples. The acoustic velocity was determined by measuring the time-of-flight and propagation path and the relationship shown as Eq. (4.16) (Svilainis 2012):

$$U = \frac{2h}{\Delta t} \tag{4.16}$$

where U is the acoustic velocity in the ice layer, h is the thickness of the ice layer, and Δt is the time interval between the echoes reflected from the ice-top and -bottom interfaces. In this study, the thickness of the ice layer (i.e., the gap between the aluminum plates) was measured to be 6.00±0.02 mm using a digital caliper.

Examples of the time-domain responses of the ultrasonic pulse-echo signals in the rime-like and glaze-like ice samples are shown in Figure 4.6. In both of the ice samples, two echo sequences can be observed, with one being from the ice-top interface, and the other from the ice-bottom interface.

To find the time intervals between the pulses in the echo sequences, an auto-correlation algorithm was applied to the digitized waveforms (Liu et al. 2016). The correlation process gave the transit time interval by measuring the time delay between the corresponding peaks in the auto-correlation function. For example, the time delay between the ice-top and -bottom echoes for the rime-like ice sample was 3.05±0.05 μs, while the time delay for the glaze-like ice sample was 3.15±0.05 μs. Thus, the acoustic velocity in the two ice samples can be calculated using Eq. (4.16), and these velocities are 3.93±0.08 and 3.80±0.08 mm/μs for the rime-like and glaze-like ice samples, respectively.

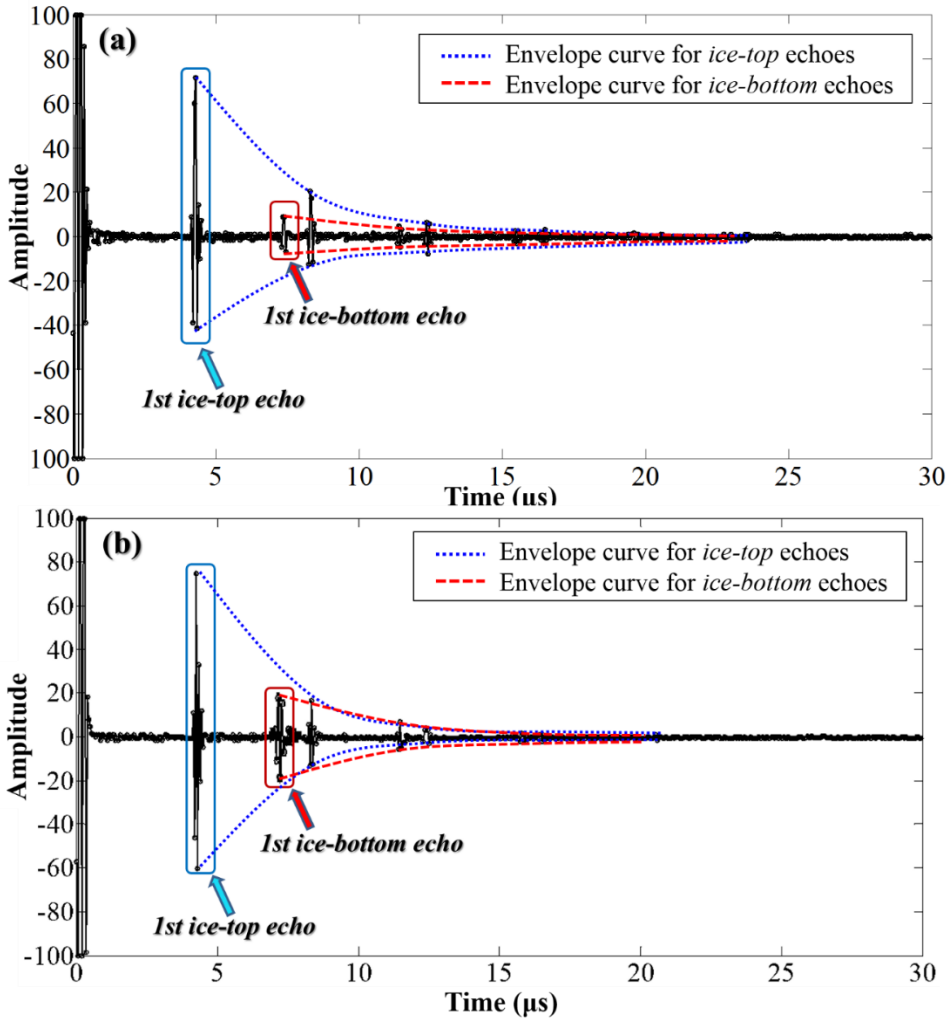

Figure 4.6 Ultrasonic pulse-echo signals with highlighted ice-top and ice-bottom echoes in (a) rime-like and (b) glaze-like ice samples.

The velocities measured using the above method were compared with previously reported values (Filipczynski et al. 1966; Hansman and Kirby 1985; Vogt et al. 2008; Abbasi et al. 2010), and selected data are given in Table 4.1. It can be seen that the acoustic velocity only exhibits a modest sensitivity to ice types (Hansman and Kirby 1985). The data values for velocity from the present study are in agreement with the values given by Hansman and Kirby (1985). The acoustic velocity in the rime-like ice sample is slightly

faster than that in the glaze-like ice sample. In addition to any differences due to composition (ice and bubbles), it has been previously found that sound speed in ice is temperature dependent, with a faster velocity being seen at lower temperatures (Vogt et al. 2008).

Table 4.1 Acoustic Velocities in Ice

Ice Type	Acoustic Velocity in Ice (mm/μs)	Data Source
General Ice	3.98	Filipczynski et al. (1966)
South Pole Ice	3.85 (at Zero Depth)	Abbasi et al. (2010)
Bubble Free Ice	3.87 (T = -10 °C) 3.85 (T = -5 °C)	Vogt et al. (2008)
Rime Ice	3.95 3.93 (T = -10 °C)	Hansman and Kirby (1985) The Present Study
Glaze Ice	3.78 3.80 (T = -5 °C)	Hansman and Kirby (1985) The Present Study

The densities for the samples were measured using $\rho = m/V$, where ρ is density, m is mass of ice sample that can be measured using the OHAUS Scout® Pro Balance with an accuracy of ±0.01 g, and V is volume of ice sample (i.e., gap volume between the top and bottom plates). The densities for the rime-like and glaze-like ice samples are measured to be 0.88±0.02 and 0.90±0.02 g/cm^3, respectively. It has been previously demonstrated by Vargas et al. (2007) that the ice density does not change significantly when the morphology of the ice changes. The only changes are when there are bubbles present. The ice densities measured in the present study are consistent with those for rime and glaze ice reported by Vargas et al. (2007) as shown in Table 4.2. These density and velocity data were then used to calculate the acoustic impedance, i.e., $Z=\rho c$, in the ice samples.

Table 4.2 Total Densities in Ice

Ice Type	Total Density in Ice (g/cm^3)	Data Source
Rime Ice	0.873	Vargas et al. (2007)
	0.88±0.02	The Present Study
Glaze Ice	0.857~0.905	Vargas et al. (2007)
	0.90±0.02	The Present Study

4.3.3.3 Ultrasonic attenuation in the ice samples

The reflection and transmission terms were calculated using Eqs. (4.8) to (4.11), and the diffraction correction was estimated using Rogers's theory (Rogers and Van Buren 1974). The frequency dependent ultrasonic attenuation coefficients for the ice samples were then determined using the amplitude spectra, obtained from the digitized ultrasonic pulse-echo signals. A Fast Fourier Transform (FFT) was applied to gated segments (with a length of 1.5 μs) of the time domain response which correspond to the echoes reflected from the ice-top and -bottom interfaces.

The amplitude spectra of the reflected signals from the ice-top and -bottom interfaces for the rime-like ice sample are shown in Figure 4.7 (a). It is seen that for each signal, it has a center frequency close to 10 MHz, which corresponds to the transducer nominal frequency. The amplitude diminishes to near zero at frequencies lower than about 3 MHz and higher than about 18 MHz. A band pass filter with -6 dB bandwidth was applied to minimize possible effects of processing low amplitude signals and noise on the attenuation coefficient. The responses are then deconvolved to obtain a frequency dependent attenuation coefficient in the frequency range of 5.5 to 14.0 MHz for the rime-like ice sample as shown in Figure 4.8.

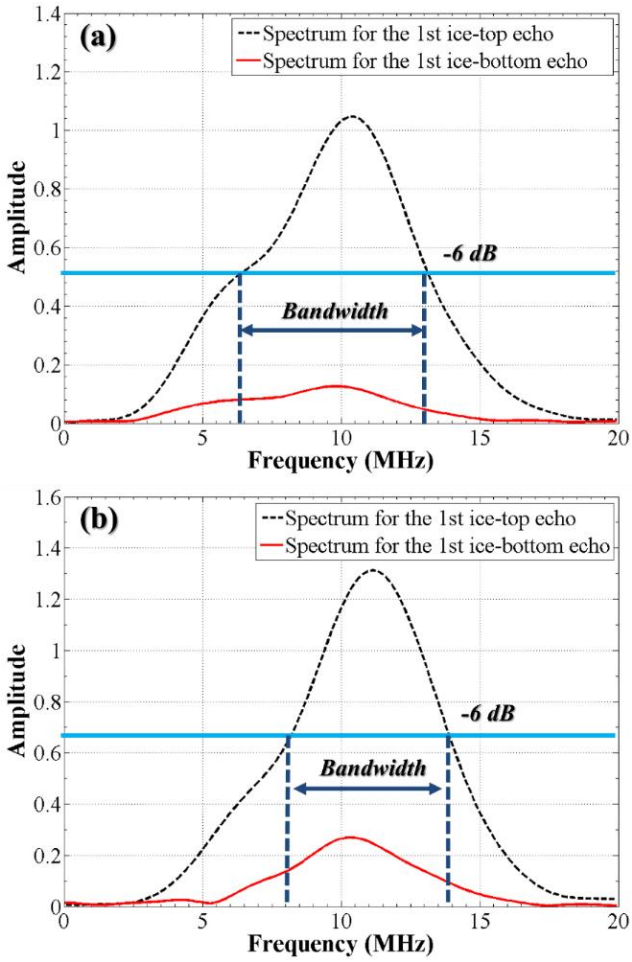

Figure 4.7 Amplitude spectra of the ice-top and –bottom echoes for the (a) rime-like and (b) glaze-like ice samples.

A similar process was applied to the data shown in Figure 4.6 (b). for the glaze-like ice sample. The spectra for the two signals are shown in Figure 4.7 (b). The data used was limited to that within the transducer response -6 dB bandwidth to minimize possible unreliable or inaccurate data due to processing low amplitude signals and noise on the attenuation coefficient. The attenuation coefficient variation in a frequency range of 7.5 to 14.5 MHz for the glaze-like ice sample is shown in Figure 4.8.

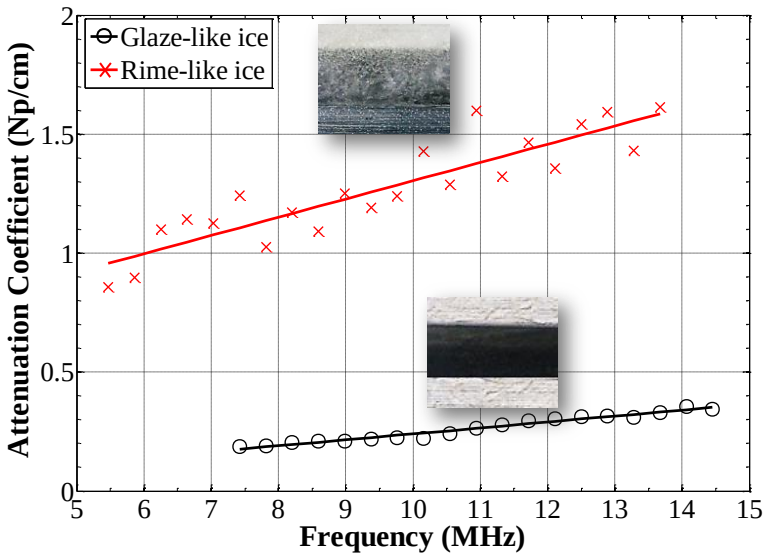

Figure 4.8 *Frequency dependent ultrasonic attenuation in the rime-like and glaze-like ice samples.*

By comparing the frequency dependent ultrasonic attenuation in the rime-like and glaze-like ice samples, it can be found that over the frequency range of 5 to 15 MHz, while the attenuation increases with frequency in both of the ice samples, at a given frequency, the attenuation has a higher value for the rime-like ice sample. It is also noted based on the linear regression lines for the attenuation data that the linear slope ($d\alpha/df$) for the rime-like ice sample is greater than that for the glaze-like ice sample. It is also seen that there is more scatter in the individual data points for the rime-like ice, which is consistant with scattering in a more complex micro-morphology.

4.4 Discussions

For the ultrasonic attenuation in other bubble/grain filled materials, for example, the carbon/epoxy laminates, the attenuation curve typically shows linear behavior with frequency as seen in Figure 4.8, and the curve slope is found to increase as the void content

increases (Jeong and Hsu 1995). It is therefore suggested that the slope of the attenuation curve for ultrasonic waves in ice is related to the void content in the ice structures.

The micro-structures of the rime-like and glaze-like ice samples are shown in Figure 4.9. It is clear that bubbles of various sizes are randomly distributed in the rime-like ice sample, together with ice grains of various shapes. In contrast, the glaze-like ice is homogeneous without any observable scattering sources. The void content is estimated to be 9.7% for the rime-like ice sample, and 0% for the glaze-like ice sample. It has been previously demonstrated that the acoustic attenuation in ice is typically caused by the wave absorption in ice and the bubble/grain induced scattering (Price 2006b).

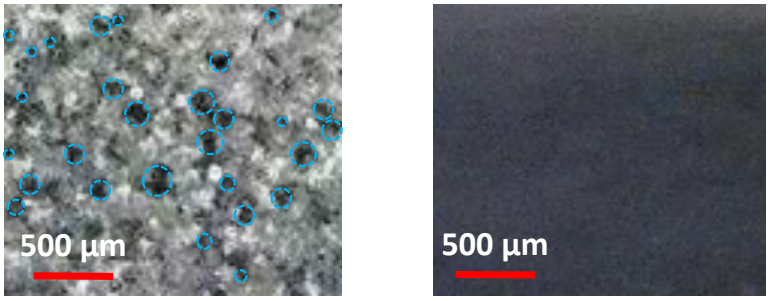

Figure 4.9 Micro structures of the rime-like and glaze-like ice samples.

In physical acoustics for bubble-ultrasound interaction, there are three distinct scattering regimes, which depend on the magnitude of the parameter $\lambda/2\pi D$, where λ is the wavelength, and D is the diameter of the bubbles/ice grains. In the Rayleigh regime, where $\lambda/2\pi D > 1$, the scattering coefficient is proportional to $D^3 f^4$; in the Stochastic regime, where $0.5 < \lambda/2\pi D < 1$, the scattering increases as a function of Df^2; in the geometric regime, where $\lambda/2\pi D < 0.5$, the scattering is no longer dependent on frequency, but is inversely proportional to bubble/grain diameter (Price 2006b).

In the present study, the mean diameter of the air bubbles was estimated to be 100 μm, while the ultrasonic wavelength was calculated to be 390 μm. It was calculated that $\lambda/2\pi D_{bubble}$ is in the 0.5 to 1 range and therefore that the bubble related scattering is mainly in the Stochastic regime, and it is proportional to f^2. The mean diameter of the ice grains in the ice sample was estimated to be 50 μm, and the parameter was calculated to be $\lambda/2\pi D_{grain} > 1$. The ice-grain caused scattering is therefore in the Rayleigh regime, and proportional to f^4.

$$\alpha_{rime}\left(\text{Np/cm}\right) = 0.067 \times f\left(\text{MHz}\right) + 0.3 \tag{4.17}$$

$$\alpha_{glaze}\left(\text{Np/cm}\right) = 0.020 \times f\left(\text{MHz}\right) + 0.08 \tag{4.18}$$

The present study considers ultrasonic attenuation in ice at high frequencies (e.g., $f \geq$ 5.0 MHz). Although there is a significant literature that considers acoustic and ultrasonic waves in ice (Selfridge 1985; Wu and Stepinski 2000; Umchid 2008; Treiber et al. 2009; Zeng et al. 2010)), unfortunately, there is only a limited literature that is available to give data for comparison with that from the present study.

Table 4.3 Acoustic Attenuation in Ice at Frequency of 1.1 MHz

Ice Type	Acoustic Attenuation Coefficient (Np/cm)	Data Source
Sea and freshwater ice	0.173	Bogorodskii et al. (1976)
Rime-like Ice	0.374	The Present Study
Glaze-like Ice	0.102	The Present Study

Bogorodskii (1976) evaluated the acoustic attenuation in sea and freshwater ice in the frequency range of 200-1100 kHz, and gives attenuation data at $f = 1.1$ MHz. Based on the equations for the linear regression line formulated in this study, the acoustic

attenuation at the same frequency (i.e., $f = 1.1$ MHz) can be estimated. The data based on the work by Bogorodskii and the present study were compared, and this is shown in Table 4.3. It is seen that the previously reported attenuation coefficient (Np/cm) is in between of the data values from the present study for the rime-like and glaze-like ice estimated using the linear equations. The results from the present study are therefore consistent with the limited data that can be deduced from the literature.

4.5 Conclusions

A strategy, based on use of frequency dependent ultrasonic attenuation, was investigated that seems to have the potential to characterization and differentiate between different types of ice that can form on aircraft in winter operation.

The measurement methodology and system was validated using the data for ultrasonic attenuation in water. The acoustic velocities in two typical ice samples were experimentally derived, and are in agreement with previous measurements. Attenuation was measured and there is a significant difference seen in the ultrasonic attenuation characteristics (e.g., the amplitude level, the scattering scale, and the linear slope) between the two types of ice.

It would appear that there is potential to add attenuation data to on-aircraft ice detection systems which could then potentially enable ice-type specific based de-icing to be implemented. Such optimized de-icing could have a potential for reducing winter weather operational costs, and ensure safety is maintained, or even improved.

CHAPTER 5
TRANSIENT HEAT TRANSFER PROCESS OVER AN ICE ACCRETING AIRFOIL

5.1 Introduction

Aircraft icing has been recognized as a big threat to flight safety since the beginning of aviation history. It is recorded that there were 944 icing-related accidents and incidents occurred in the US from 1978 to 2005 (Petty and Floyd 2004; Green 2006). Philip Appiah-Kubi updated this number with another 228 accidents and 30 incidents from 2006 to 2010 (Appiah-Kubi 2011). Based on these investigations, 40% of the accidents were related to in-flight icing occurring on the wings, fuselage or control surfaces. Ice accumulated on these surfaces can significantly contaminate the flight performance by reducing lift and increasing drag. The in-flight ice formation and accretion are highly dependent on weather conditions that include liquid water content (LWC), atmosphere temperature, and water droplet size. The accreted ice can be rime, glaze, or mixed ice shapes based on the ice morphology. In rime ice accretion, the impinged droplets freeze immediately upon impact with surfaces, resulting in a rough, milky white appearance conforming to the aircraft surfaces. In glaze ice accretion, however, just a portion of the impinged water freezes on impact. Moreover, there is a water run-back behavior over the aircraft or existing ice surfaces. This process creates a clear, smooth, and dense ice appearance. Mixed ice is a transition state between rime and glaze ice (Steuernagle et al. 2008). The different ice morphologies are subject to cloud conditions. Rime ice generally forms at low LWC and cold temperatures (typically below -8 ºC) with small droplets surrounded, at which

situation the heat transfer is adequate to remove all of the latent heat in the collected water. Glaze ice is formed at higher LWC and temperatures just below the freezing point, where the heat transfer is inadequate to remove all of the latent heat in the collected water (Hansman and Kirby 1987). Therefore, rime ice accretion is mainly determined by the droplet impingement behavior; the amount and rate of ice accretion are controlled by the droplet collection efficiency. However, in glaze ice accretion, the ice growth rate is essentially controlled by the local heat transfer capacity that determines the amount of latent heat removal from the collected droplets or run-back film and rivulets (Yamaguchi and Hansman 1992).

During the past years, many efforts have been made to model the ice accretion. Some ice prediction methods have been developed to help understand the physical details of various icing processes (Myers 2001; Fortin et al. 2006). An essential part of modeling is the energy balance, as first formulated by Messinger (Messinger 1953). Numerous improvements and corrections have been subsequently made to the Messinger model. Based on these studies, the ice and water growth in the presence of incoming super-cooled droplets can be evaluated and predicted (Myers 2001). The results derived in these studies indicate that rime icing could be adequately simulated and well understood. Glaze icing, however, is hard to be accurately simulated, and there is considerable uncertainty regarding the heat transfer capacity and ice accretion profiles (Kind et al. 1998). To provide essential physical descriptions regarding the heat transfer during ice accretion, many experimental studies have been conducted in both wind tunnel and flight tests.

As reviewed by Kind (Kind et al. 1998), there are mainly two experimental approaches to study the heat transfer characteristics during ice accretion. One is called dry-air testing, in which replicas of the real ice shapes are used to evaluate the effect of the simulated irregular ice shapes and roughness elements on the aerodynamic performance and local convective heat transfer (Arimilli et al. 1984; Hansman and Kirby 1987; Hansman et al. 1991; Yamaguchi and Hansman 1992; Henry et al. 1994; Bragg et al. 1994; Henry et al. 1995; Bragg et al. 1996; Kind et al. 1998; McClain et al. 2010). It is considered that the initially frozen water beads form the initial roughness elements. These roughness elements may trigger the aerodynamic boundary layer transition, and hence, enhance the convective heat transfer. The enhanced convection, in turn, accelerates the roughness formation and ice accretion (Hansman and Kirby 1987; Bragg et al. 1996). The other approach to investigate the heat transfer process is to create real ice shapes in an icing wind tunnel. The heat transfer measurements are performed on the ice shape itself, rather than a casted ice model (Yamaguchi and Hansman 1992; Wang et al. 2007; Wang et al. 2008). It is observed that the convective heat transfer is constant on smooth and uniform ice surfaces, and is enhanced in regions filled with roughness and ice feathers (Henry et al. 2000).

Various measurement techniques have been developed and implemented in these experimental studies to observe and reconstruct the features in icing process. Among these techniques, strobe synchronized CCD video technology, ultrasonic measurement techniques, thermocouple measurements, and infrared thermography are typical methods that have been successfully applied in dealing with the icing-related measurements (Kind et al. 1998; Henry et al. 2000; Wang et al. 2008; Mohseni et al. 2012). The use of

thermocouples provides researchers the access to collect the time-resolved temperature variation information at a single point. However, thermocouple measurement is an intrusive method that can disturb the airflow over an airfoil, and hence, influence the convective heat transfer process. As infrared technology has developed quickly in recent years, infrared thermography is now available for measuring surface temperature distribution over an iced airfoil. An infrared camera with high sensitivity can provide accurate temperature measurements at both high spatial and good temporal resolutions. Hansman and Yamaguchi investigated the laminar/turbulent transition behavior on an iced surface using an infrared technique (Yamaguchi and Hansman 1992). Bragg measured the convective heat transfer on an airfoil with simulated ice roughness by applying the infrared thermography (Bragg et al. 1996). The heat transfer characteristics were well defined in these studies. However, most of them were focused on the end-point features, the initial transient heat transfer behavior was ignored, which is actually of great importance in understanding the evolution of the ice accretion at the initial state.

In order to quantify the physical details during an actual icing process, from droplet impingement to ice shape formation, a time-resolved temperature distribution measurement is strongly desired to monitor and evaluate the transient heat transfer behavior. Mohseni implemented an infrared imaging technique in monitoring the ice accretion on an airfoil (Mohseni et al. 2012). This technique makes it possible to measure the transient ice formation and growth at the leading edge of an NACA 0021 airfoil based on the temperature features associated with the ice features. However, no heat transfer process was investigated in his paper.

In this study, an instant energy balance equation on an icing airfoil was modeled based on the previous heat transfer modeling in icing processes. A methodology based on infrared thermography was developed to achieve nonintrusive measurements of the transient heat transfer process over an ice accreting NACA 0012 airfoil. Comprehensive surface temperature distribution measurements were performed under various icing conditions (e.g. air temperature, liquid water content (LWC), and wind speed) in the ISU icing research wind tunnel (ISUIRT). Time-resolved temperature distributions on the ice accreting airfoil were acquired. Chord-wise temperature variations and evolutions were extracted in describing the ice formation and expansion under wet and dry icing conditions. Instantaneous temperature distributions around the leading edge were isolated in diagnosing the transient details at the initial icing state. Finally, based on the instant heat transfer model derived in this paper, the convective heat transfer was characterized under various icing conditions.

5.2 Transient Heat Transfer in Ice Accretion

At any instant on an icing airfoil, the energy balance in a control volume is schematically shown in Figure 5.1. The rate at which thermal and mechanical energy enters the control volume, minus the rate at which thermal and mechanical energy leaves the control volume is equal to the rate of energy increase stored within the control volume as shown in Eq. (5.1) (Incropera 2011)

$$\dot{E}_{in} - \dot{E}_{out} = \frac{dE_{st}}{dt} \equiv \dot{E}_{st} \tag{5.1}$$

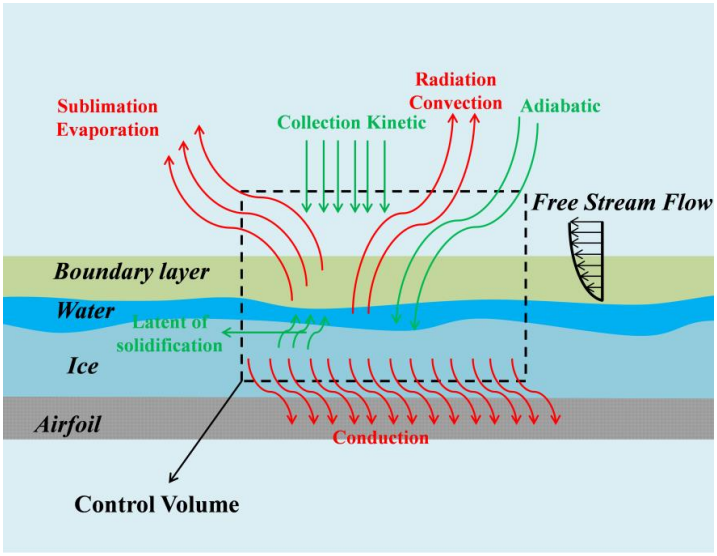

Figure 5.1 A schematic of heat balance during ice accretion in a control volume.

The energy enters the control volume includes adiabatic heating and kinetic heating energy. The energy leaves the control volume includes the evaporation and sublimation, convection heat, energy radiation, conduction heat, and sensible heat that is produced by the temperature change of water and ice (Myers 2001; Fortin et al. 2006). The energy storage changes within the control volume are due to changes in the internal, kinetic, and/or potential energies of its contents as shown in Eq. (5.2).

$$\Delta E_{st} = \Delta U + \Delta KE + \Delta PE \tag{5.2}$$

When ice accretes on an airfoil surface, the kinetic and potential energy changes in the control volume are small and can be neglected. While the change of the internal energy is mainly due to a latent heat release, which relates the intermolecular forces that influence the liquid-solid phase change, and less from a sensible component that accounts for the motion of the atoms/molecules, the energy storage change rate is reduced to the form of Eq. (5.3).

$$\dot{E}_{st} = -\left(\dot{Q}_{latent} + \dot{Q}_{ss}\right) \tag{5.3}$$

Thus, at any instant, the energy balance in the control volume can be expressed in Eq. (5.4).

$$\left[\dot{Q}_{adh} + \dot{Q}_{kin}\right] - \left[\dot{Q}_{conv} + \dot{Q}_{sub/evp} + \dot{Q}_{cond}\right] = -\left(\dot{Q}_{latent} + \dot{Q}_{ss}\right) \tag{5.4}$$

The heat introduced by adiabatic heating occurs inside of the boundary layer and is defined in Eq. (5.5).

$$\dot{Q}_{adh} = h_{cv} \cdot \left(T_{rec} - T_{\infty}\right) \cdot A \tag{5.5}$$

The recovery temperature, T_{rec} is originally defined by Schlichting (2000), and successfully implemented by Fortin in modeling heat transfer during ice accretion (Fortin et al. 2006).

$$T_{rec} = T_{\infty} + r \cdot \frac{T_{\infty}}{T_e} \cdot \frac{U_e^2}{2 \cdot Cp_{air}} \tag{5.6}$$

where r is the recovery factor, and can be defined as $r = \sqrt{Pr}$ for laminar flow. Here, the Prandtl number is defined in Eq. (5.7).

$$Pr = \frac{Cp_{air} \cdot \mu_{air}}{k_{air}} \tag{5.7}$$

The heat income due to kinetic energy as droplets impact on surfaces is defined in Eq. (5.8).

$$\dot{Q}_{kin} = \frac{1}{2} \cdot \dot{m}_{imp} \cdot V_{imp}^2 \tag{5.8}$$

where $\dot{m}_{imp}$ is the mass flux of water impingement, and defined as $\dot{m}_{imp} = LWC \cdot V_{imp} \cdot A$.

The convective heat transfer occurs when cold air flows over the surface. The convection term in the energy equation is expressed in Eq. (5.9).

$$\dot{Q}_{conv} = h_{cv} \cdot \left(T_s - T_\infty\right) \cdot A \tag{5.9}$$

The heat removal by evaporation and sublimation is dependent on the amount of mass taken by the two process. The mass flux due to evaporation and sublimation can be expressed in the form of Eq. (5.10), as has been successfully applied by Li (2014) and Dong (2015).

$$\dot{m}_{es} = 0.696 \cdot \frac{h_{cv}}{Cp_a} \cdot \frac{p_s\left(T_b\right) - p_s\left(T_\infty\right)}{p_m} \cdot A \tag{5.10}$$

where the saturated vapor pressures, $P_s(T_b)$ and $P_s(T_\infty)$ are obtained using Goff-Gratch equation (Murphy and Koop 2005). Thus the latent heat of evaporation and sublimation can be quantified as shown in Eq. (5.11).

$$\dot{Q}_{sub/evp} = \dot{m}_{es} \cdot \left[\eta \cdot L_i + \left(1-\eta\right) \cdot L_w\right] \tag{5.11}$$

The conductive heat transfer occurs if there is a temperature gradient between the ice/water and the airfoil substrate. The heat flux due to thermal conduction is expressed in Eq. (5.12).

$$\dot{Q}_{cond} = \frac{A \cdot \left(T_s - T_{airfoil}\right)}{R_{tot,cond}} \tag{5.12}$$

where the equivalent thermal resistance for conduction, $R_{tot,cond}$ is derived based on the equivalent thermal circuit theory.

$$R_{tot,cond} = \frac{H_{ice}}{k_{ice}} + \frac{H_{airfoil}}{k_{airfoil}} \tag{5.13}$$

where H_{ice} is the thickness of ice layer, and $H_{airfoil}$ is the thickness of the airfoil substrate. Substitute Eq. (5.13) into (5.12), the heat flux due to thermal conduction can be derived as:

$$\dot{Q}_{cond} = \frac{A \cdot \left(T_s - T_{airfoil}\right)}{\frac{H_{ice}}{k_{ice}} + \frac{H_{LE}}{k_{airfoil}}} \tag{5.14}$$

The latent heat of fusion is released when water freezes on the airfoil surface. The amount of the latent heat released in the control volume is dependent on the mass of frozen water, and can be written as:

$$Q_{latent} = m_{freeze} \cdot L_s \tag{5.15}$$

If set the control volume at the stagnation point, the amount of the water collection is principally from droplet impingement. Depending on the air cloud and wing conditions, the amount of ice accumulated in the control volume is determined by the freezing ratio, η, which is the mass ratio of the frozen water and that collected in the control volume. Thus, the freezing rate in the control volume can be expressed as Eq. 16.

$$\dot{m}_{freeze} = LWC \cdot V_{imp} \cdot A \cdot \beta \cdot \eta \tag{5.16}$$

Then the heat flux due to the latent heat of fusion can be derived as shown in Eq. 17.

$$\dot{Q}_{latent} = \dot{m}_{freeze} \cdot L_s = LWC \cdot V_{imp} \cdot A \cdot \beta \cdot \eta \cdot L_s \tag{5.17}$$

The sensible heat is mainly due to the enthalpy variation of frozen and liquid water from the freezing temperature to the surface temperature.

$$\dot{Q}_{ss} = \dot{m}_{freeze} \cdot Cp_i \cdot \left(T_f - T_s\right) + (\dot{m}_w - \dot{m}_{freeze}) \cdot Cp_w \cdot \left(T_f - T_s\right) \tag{5.18}$$

Here, $\dot{m}_w$ is the mass flux of water in the control volume. At the stagnation point, the water is mainly from the droplets impingement, so we assume $\dot{m}_w \approx \dot{m}_{imp} \cdot \beta$. Substitute

Eq. (5.5), (5.8), (5.9), (5.11), (5.14), (5.17) and (5.18) into Eq. (5.4), the instant energy balance arrives to the following expression:

$$\begin{aligned} & h_{cv}\cdot\left(T_{rec}-T_{\infty}\right)\cdot A+\frac{1}{2}\cdot LWC\cdot V_{imp}\cdot A\cdot V_{imp}^{2}-A\cdot\left[h_{cv}\cdot\left(T_{s}-T_{\infty}\right)\right] \\ & -A\cdot\left(T_{s}-T_{airfoil}\right)\Big/R_{cond,tot}-0.696\cdot h_{cv}/Cp_{a}\cdot\left[p_{s}\left(T_{b}\right)-p_{s}\left(T_{\infty}\right)\right]\Big/p_{m} \\ & \cdot A\cdot\left[\eta\cdot L_{i}+\left(1-\eta\right)\cdot L_{w}\right]+LWC\cdot V_{imp}\cdot A\cdot\beta\cdot\begin{bmatrix}\eta\cdot L_{s}+\left(T_{f}-T_{s}\right)\\ \cdot\left(\eta\cdot Cp_{i}+\left(1-\eta\right)\cdot Cp_{w}\right)\end{bmatrix}=0 \end{aligned} \tag{5.19}$$

Since the airfoil is pre-frozen to the same temperature level as that of the oncoming airflow before the water droplets impinge on it. The temperature differences in the convection and conduction terms are the same and denoted as ΔT. Therefore, the convection coefficient, h_{cv} can be written in the following form:

$$h_{cv}=\frac{\left[\Delta T/R_{cond,tot}-LWC\cdot V_{imp}\cdot\beta\cdot\left[\begin{matrix}\eta\cdot L_{s}+\left(T_{f}-T_{s}\right)\cdot\\ \left(\eta\cdot Cp_{i}+\left(1-\eta\right)\cdot Cp_{w}\right)\end{matrix}\right]-0.5\cdot LWC\cdot V_{imp}^{3}\right]}{\left[T_{rec}-T_{\infty}-\Delta T-0.696\cdot\frac{\left[p_{s}\left(T_{b}\right)-p_{s}\left(T_{\infty}\right)\right]}{\left(Cp_{a}\cdot p_{m}\right)}\cdot\left[\eta\cdot L_{i}+\left(1-\eta\right)\cdot L_{w}\right]\right]} \tag{5.20}$$

5.3 Experimental Setup and Measurement Procedure

5.3.1 Experimental Facility and Setup

The experiments were carried out in the ISU Icing Research Tunnel (ISUIRT) as shown in Figure 5.2. The wind tunnel is a closed-loop type tunnel. It is equipped with a heat exchange system that can refrigerate the tunnel to freezing conditions as low as -20 °C. The operating temperature can be set by a temperature controller. There is a pneumatic spray system installed before the test section. The spray system consists of three pneumatic atomizing spray nozzles and two pressure regulators. The pressure

regulators are used to control the water and air pressures. By adjusting the pressure regulators, the mass flow rate of water can be set in coordinate with the desired LWC. The size of the water droplet is adjusted by controlling the relative air and water pressures, and can be set to mean volume diameters from 15 to 100 μm. The wind speed in this closed circuit tunnel can be set up to 90 m/s.

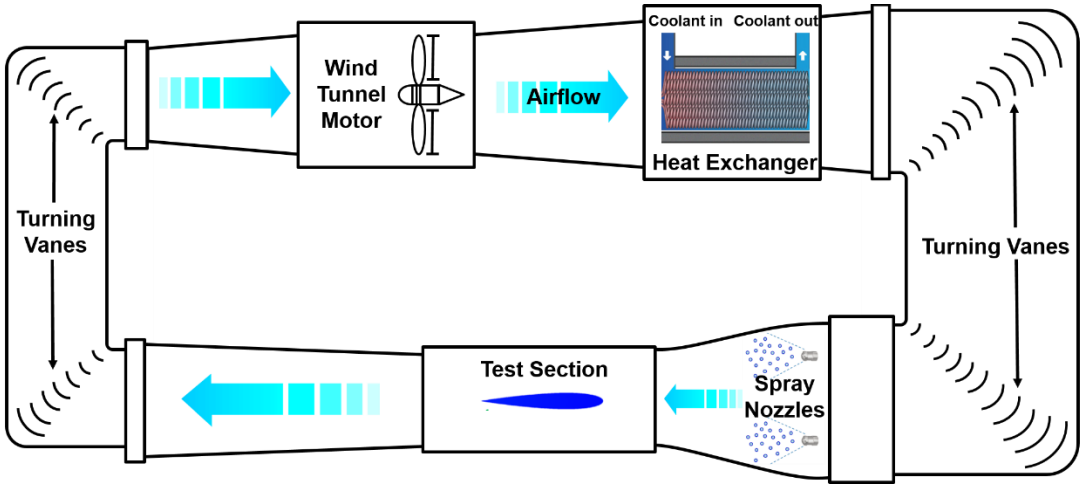

Figure 5.2 A Schematic of the ISU-Icing Research Tunnel (ISUIRT).

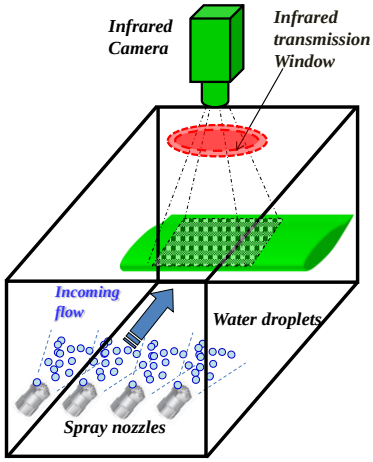

Figure 5.3 A schematic of the experimental setup for infrared measurements on NACA 0012 airfoil.

A schematic of the experimental setup for infrared imaging measurements on an NACA 0012 airfoil is shown in Figure 5.3. The test section has a cross-section dimension of 254×254 mm (W×H). The window panels in the test section are detachable, which makes both visible and infrared imaging measurements available. In this study, an infrared transmission window (FLIR IR Window-IRW-4C) with a diameter of 101.6 mm was set in the top panel of the test section. An infrared (IR) camera (FLIR A615) was mounted above the IR window as shown in the figure. The wavelength range that can be detected by the camera sensor is from 7.5 to 14 μm. The resolution of the camera is 640 × 480 pixels, which is capable of providing high accuracy of measured temperatures spotting even small objects from a distance. FLIR A615 adopts a new camera interface standard, GigE Vision that allows for fast image transfer even over long distances. The camera can achieve a 16-bit temperature linear output at frequencies up to 200 Hz. The IR imaging measurements were conducted using a 3D printed NACA 0012 airfoil that spanned the width of the test section. The chord length of the airfoil is 101.6 mm. The airfoil had a coating of primer and was wet-sanded to a fairly smooth finish.

5.3.2 Measurement Calibration

In the experiments, the IR camera was mounted above the test section at a distance of 350 mm. The infrared radiation from the airfoil and ice/water surface can be transmitted through the IR window with a transmission coefficient of 0.82. The emissivity coefficients of the airfoil surface, ice, and water are listed in Table 5.1, respectively.

Table 5.1 Emissivity of materials in the experiments

Material	Emissivity
Airfoil surface (primer coated)	0.96
Ice	0.965
Water	0.95-0.963

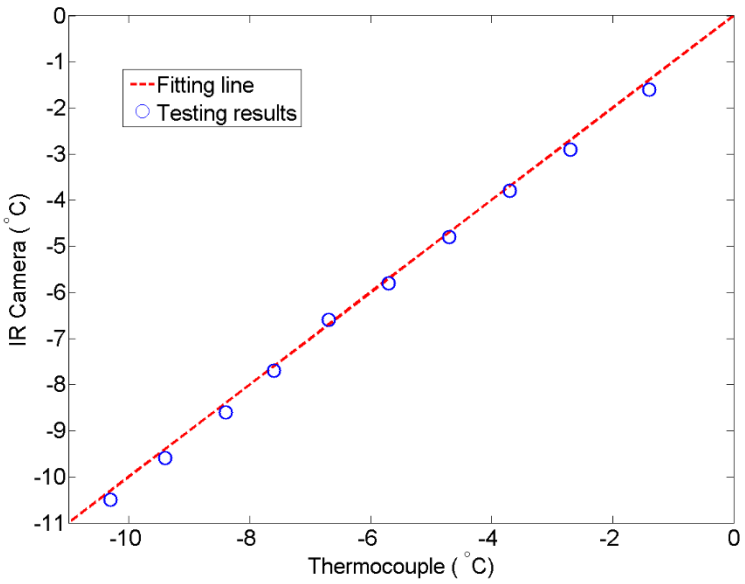

Figure 5.4 Comparison of the temperature measured by the IR camera and a thermocouple.

To validate the IR measurement, a spot temperature measurement was performed on the airfoil. The temperatures measured by the IR camera were compared with those from a thermocouple as shown in Figure 5.4. The temperature range was from -11 to 0 ºC. The comparison indicates that the temperatures measured by the IR camera and the thermocouple are in good agreement.

5.3.3 Test Conditions

In the experiments, various icing conditions can be simulated by adjusting the air temperature, wind speed, and LWC level. In order to produce both wet and dry ice growth, the wind tunnel temperature was set at -4 and -8 ºC to provide warm and cold temperatures.

In the meantime, a series of LWC levels can be adjusted to achieve different icing conditions. The effects of Reynold number on the temperature distribution and heat transfer were examined by adjusting the wind speed. The airfoil was set at the angle of attack of -5º for all test conditions. Table 5.2 lists the icing tunnel conditions in the experiments.

Table 5.2 Icing conditions examined in the experiment

Temperature (ºC)	Wind Speed (m/s)	LWC (g/m^3)	Ice Growth
-4	20	0.3	Wet
		1.0	Wet
		3.0	Wet
	40	0.3	Wet
		1.0	Wet
		3.0	Wet
-8	20	0.3	Dry
		1.0	Dry
		3.0	Wet
	40	0.3	Dry
		1.0	Wet
		3.0	Wet

In this experiment, the free stream temperature in the test section was monitored by a thermocouple set in the upstream of the airfoil. When setting the wind tunnel temperature, a cooling process at low wind speed was required to freeze the air below the target temperature. Then turn up the motor to the target wind speed. The wind tunnel temperature will rise due to the enhanced convection in the tunnel. Multiple adjustments were required to achieve a stable temperature environment. Then, the air and water pressures in the spray system were adjusted to achieve the target LWC level. The IR image acquisition and spray

system start-up were simultaneously enabled to record the icing process, from droplet impingement, impact freezing, to film/rivulets run-back over the airfoil surface.

5.4 Results and Discussions

5.4.1 Time-Resolved Temperature Distribution over Icing Airfoil

In this section, the time-resolved temperature distribution over icing airfoil under both wet and dry icing conditions are presented to provide more underlying physical details in the initial ice formation and accretion. Four typical icing processes are discussed at V_∞=40 m/s: (1) lower LWC level & warm temperature, (2) higher LWC level & warm temperature, (3) lower LWC level & cold temperature, and (4) higher LWC level & cold temperature. Here, lower and higher LWC level correspond to LWC = 0.3 and 3 g/m^3; warm and cold temperatures correspond to T_∞=-4 and -8 °C, respectively. Both wet and dry ice growth were observed under these conditions. The time evolution of temperature distribution over the icing airfoil under these icing conditions are shown in Figure 5.5 and Figure 5.6. The temperature shown in the figures is the temperature difference between the surface and the free stream flow.

The icing processes at the warm temperature are basically wet growth as shown in Figure 5.5. At lower LWC level (Figure 5.5(a)), less water was collected on the airfoil surface. As water droplets impinge onto the leading edge of the airfoil (t= 0.3 s), it can be found that the temperature difference is smaller than 1.0 ºC, which indicates the water droplets are in the super-cooled state. As more water impinges onto the surface, a water film forms near the leading edge (t= 0.5-1.0 s). In the meantime of film formation, part of the water freezes and release latent heat of fusion, indicated by the temperature increase

over the freezing region. The temperature near the leading edge is higher than that in downstream regions. More water is collected near the leading edge, and more latent heat of fusion can be taken away by heat transfer. However, the heat transfer is inadequate to remove all the latent heat of fusion in the water, as more water impinges on the surface, the water film transports downstream and breaks into rivulets (t= 3.2-8.2 s). The residual latent heat of fusion in the rivulet-shaped water is removed at further downstream as can be seen at t= 8.2 s.

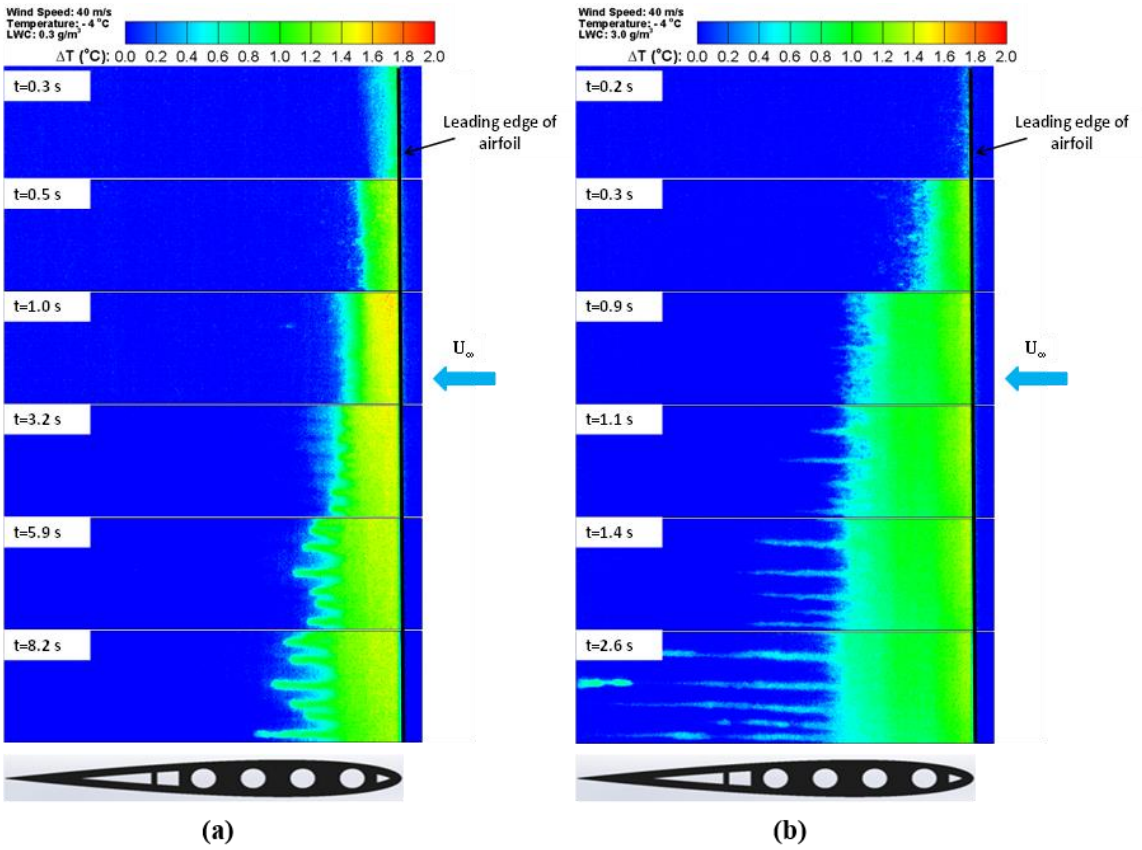

Figure 5.5 Time evolution of temperature distribution over icing airfoil at test conditions of T_∞=-4 ℃ and (a) LWC=0.3 g/m^3; (b) LWC=3.0 g/m^3

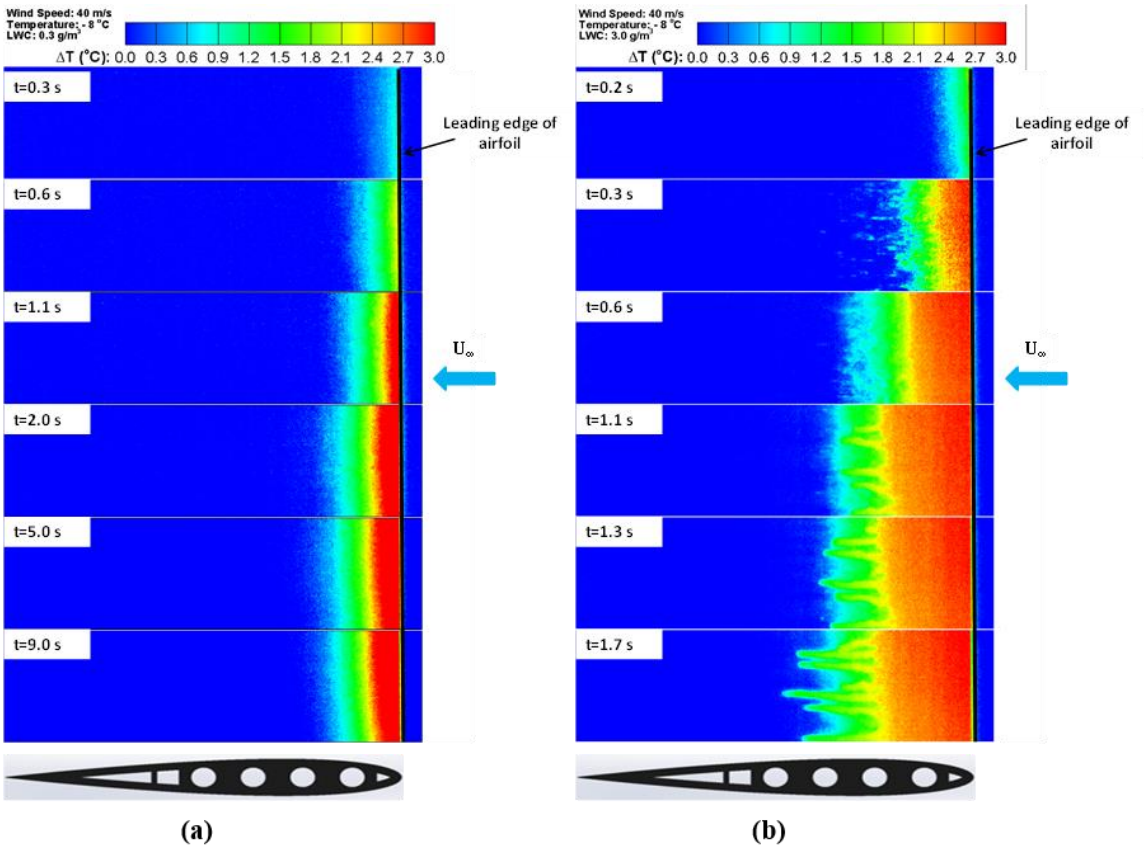

Figure 5.6 Time evolution of temperature distribution over icing airfoil at test conditions of T_∞=-8 ℃ and (a) LWC=0.3 g/m^3; (b) LWC=3.0 g/m^3

At higher LWC level (Figure 5.5(b)), more water impinges on the airfoil surface. The process of film formation, water transport, and rivulets formation is similar to that at lower LWC level. The difference is that, at the downstream edge of the film, a rougher region can be observed as indicated by the randomly distributed spots (*t*= 0.3-0.9 s). The temperature in the rough region is lower than that in the film region. In one hand, the amount of water decreases as it transports downstream, thus less latent heat of fusion can be removed by heat transfer. In the other hand, the roughness elements may trigger the flow transition and enhance the convective heat transfer. As time goes on, water rivulets form further downstream (*t*= 1.1-2.6 s). Some more latent heat of fusion can be removed

as the rivulets flow downstream. However, since too much water impinges on the surface, heat transfer is inadequate to remove all the latent heat of fusion during the water transport, the later impinged water would follow the track of the film and rivulets until the trailing edge ($t \geq 2.6$ s).

At the cold temperature, both wet and dry ice growth presented depending on the operating LWC level as shown in Figure 5.6. The icing process at lower LWC level is typically a dry growth as shown in Figure 5.6(a). Since the temperature difference between the impinged water and the freestream (or airfoil substrate) is bigger at the cold temperature, more heat transfer dominants over the surface, and it is adequate to remove all the latent heat of fusion in the water. As water droplets impinge on the surface, they will freeze immediately on impact, and no further runback behavior is observed (t= 0.3-0.6 s). As more droplets impinge on the surface, more latent heat is removed by the heat transfer, especially around the leading edge as can be seen from t = 1.1 to 2.6 s. In this process, an obvious boundary between the low- and high-temperature regions can be observed. This is mainly because of the higher collection efficiency around the leading edge. As more water is deposited around the leading edge, more latent heat is removed by heat transfer, represented by higher temperature. Also, as roughness elements form downstream, a flow transition could be triggered, and the convective heat transfer is therefore enhanced, resulting in a faster freezing process. The smaller temperature difference is a result of the change of sensible heat. It can be found that the temperature remains the same after t= 2.0 s. The ice layer becomes thicker as time goes on, rather than expands further downstream as that occurs at the warm temperature.

As increase to higher LWC level (Figure 5.6(b)), at the initial state (t= 0.2-0.6 s), the icing process is more like a dry growth. The water droplets freeze immediately as they impinge on the airfoil surface, and there are scattered roughness elements form downstream as shown in the figure. These initial roughness elements may form as the water droplets splash upon the impact. In this initial process, heat transfer is adequate to remove all the latent heat of fusion in the water, such that no obvious water run-back is observed. As more water impinges on the surface and splashes downstream, heat transfer is inadequate to remove all the latent heat of fusion, and a wet ice growth presents. There is a water run-back happening after t= 1.1 s, and rivulets form in downstream as can be seen from t= 1.1-1.7 s. As the water transports downstream, the residual latent heat is further removed by heat transfer. Thus, rivulet shaped ice forms along the airfoil surface, and further contribute to the flow transition and convection enhancement. As time goes on, the collected water will follow the track of the existing ice patterns and freeze further downstream.

5.4.2 Chord-wise Temperature Variation and Evolution

From the temperature distributions over the icing airfoil, it is noticed that there is a chordwise temperature gradient as water/ice expands downstream. There are multiple factors that attribute to this temperature gradient, e.g. water impingement, aerodynamics, and heat transfer. Since temperature is an indicator of heat, and in this particular circumstance, temperature features are good indications of ice features as well; if we can extract the temperature variations at different chord-wise locations, the transient process

of ice feature formations and heat balance evolutions along the airfoil could be further revealed.

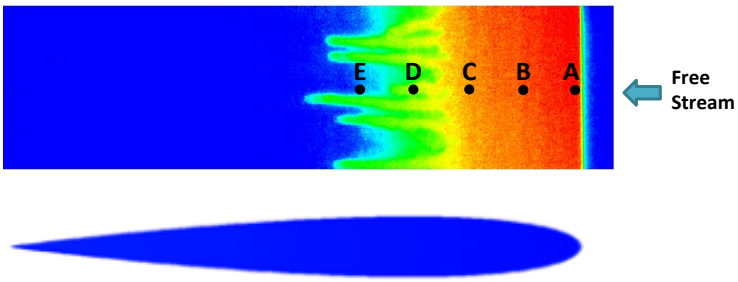

Figure 5.7 Set of monitoring points along chord-wise.

In this section, five monitoring points were set along chord-wise to evaluate the temperature variations at different chord-wise locations. Based on the local temperatures at different time, the ice feature expansion and heat balance evolution along the airfoil are subsequently discussed. The monitoring points were set as shown in Figure 5.7. Point A was set on the upper surface at the leading edge. The five points were aligned with the same spacing: AB = BC = CD = DE = 10% chord length. Since the heat release in an ice accretion is mainly from the latent heat of fusion in water while the heat removal is mainly due to convection, which is a function of temperature difference between surface and freestream flow. As water impinges on the surface, if in dry ice growth, all of the latent heat is released, and the local temperature turns out to be an indication of the amount of local ice accretion. As ice forms and accretes on the surface, roughness elements will form, which can essentially change the boundary layer flow and enhance the heat transfer process. After the latent heat of fusion is completely taken away by the heat transfer, the continuous temperature decrease is due to the discharge of sensible heat. In this section,

the transient ice accretion and heat balance evolution along the chord-wise locations at a wind speed of 40 m/s under different LWC levels (0.3, 1.0, and 3.0 g/m^3) are evaluated.

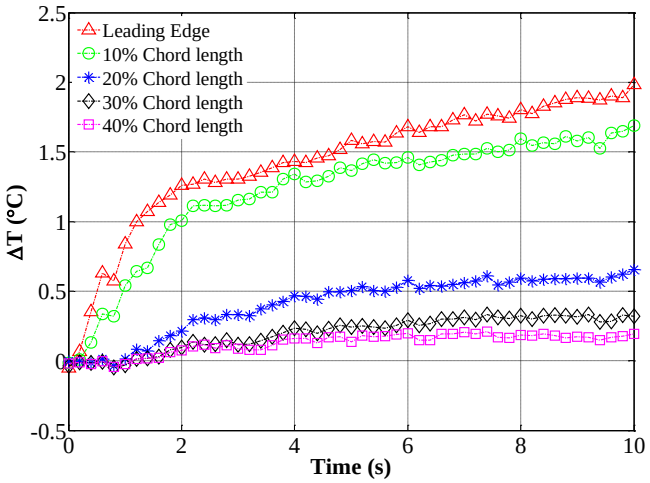

Figure 5.8 Temperature variations at different chord-wise locations at test condition of T_∞ = -8 °C & LWC = 0.3 g/m^3.

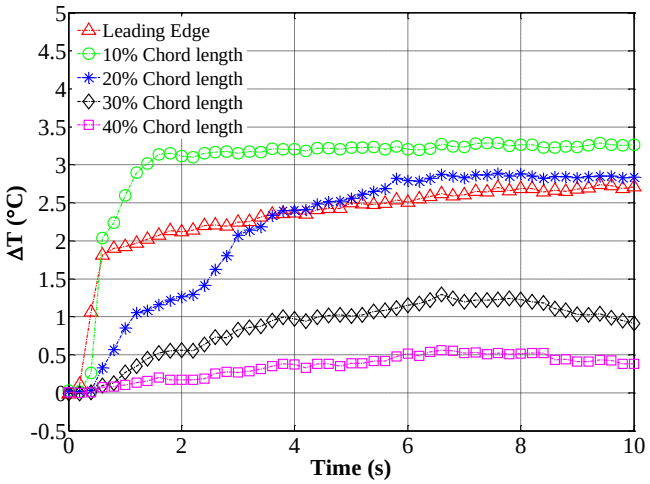

Figure 5.9 Temperature variations at different chord-wise locations at test conditions of T_∞ = -8 °C & LWC = 1.0 g/m^3.

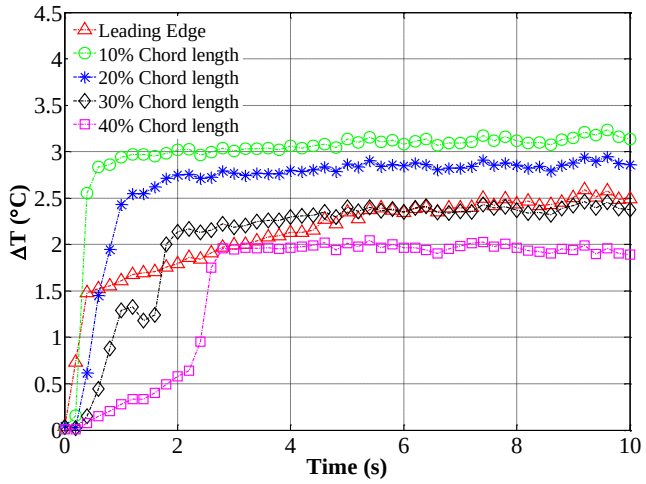

Figure 5.10 Temperature variations at different chord-wise locations at test conditions of T_∞ = -8 °C & LWC = 3.0 g/m^3.

Figure 5.8 shows the temperature variations at the chord-wise locations under test condition of T_∞ = -8 °C and LWC = 0.3 g/m^3. It can be found that the temperature at different chord-wise locations basically increases as time goes on. In the initial impingement state ($t \leqslant$ 2.0 s), the temperature around the leading edge quickly increases to a higher level, while the temperature at downstream locations has only slight changes. This is mainly because of the collection of water around the leading edge. At the angle of attack of -5 °, the droplet collection efficiency distribution, as investigated by Özgen, indicates that it is highest at the stagnation point with a value of about 0.6; and quickly reduces to 0 at locations around 15% chord length (Özgen and Canıbek 2009). Therefore, at the initial state, most of the collected water droplets are concentrated around the leading edge. Since the temperature is sufficiently cold in this test condition, and the collection rate of water mass is low at LWC of 0.3 g/m^3, the heat transfer is adequate to remove all the latent heat of fusion in the water. Ice features rapidly form and accrete around the

leading edge, as indicated by the rapid increase of temperature in the figure. As time goes on, the further collected water continually deposits around the leading edge and a thin ice film forms. The icing process under this test condition is obviously a dry growth. The collected water freezes immediately upon impact, and there is no water run-back on the surface. As more droplets impinge on the surface, the ice film becomes thicker but conforms to the airfoil profile. The temperature continuously increases along with the latent heat release. For the temperature at downstream locations, it can be seen in the figure that there is a slight increase as time goes on. It is suggested that this slight increase is due to the heat dissipation by the airfoil, though it is small and negligible.

Figure 5.9 shows the temperature variations at different chord-wise locations under test condition of T_∞ = -8 ºC & LWC = 1.0 g/m^3. It can be seen that as droplets impinge on the airfoil surface ($t \leq 2.0$ s), the temperatures around the leading edge (within 10% chord length) quickly increase to higher levels. However, it is clear that the temperature at 10% chord length increases to an even higher level than that at the leading edge. This suggests that there is more latent heat release at 10% chord length under this test condition. Özgen's investigation shows that the distribution of droplet collection efficiency remains the same even at higher LWC levels. If there is no water run-back, the latent heat at 10% chord length should be less than that at the leading edge. At the LWC of 1.0 g/m^3, however, there is more water collected on the surface. Moreover, the heat transfer is inadequate to remove all the latent heat of fusion in the collected water. Thus, there should be a water run-back on the surface, so that more water deposits at 10% chord length, and release more latent heat of fusion as indicated in the figure. As time goes on, the temperature at both the

leading edge and 10% chord length tend to become constant, which suggests a constant heat release over the region. And still, more latent heat is released at 10% chord length. In the meantime, it can be noticed that the temperature at 20% chord length gradually increases to a high level, and even higher than that at the leading edge after t = 4 s. This suggests that the local latent heat of fusion at 20% chord length is increasingly removed as time goes on, and provides further evidence of the existence of water run-back behavior. As for the temperature at further downstream (30% chord length), there is also a recognizable increase before t = 7 s. However, it is hard to tell if there is latent heat release at the location. The heat dissipation across the airfoil may also contribute to the temperature increase.

Figure 5.10 shows the temperature variations at different chord-wise locations under test condition of T_∞ = -8 ºC & LWC = 3.0 g/m^3. Since there is far more water impinges on the airfoil surface per unit time under this condition. If the droplet collection efficiency remains the same, there is accordingly far more water that is collected on the surface. This initial water collection process, thus is largely shortened, and recognized to be less than 1 s, as featured by the rapid increase of temperature around the leading edge. It is obvious that the temperature at 10% chord length is much higher than that at the leading edge. This gives us a clue that much more latent heat is released at 10% chord length, which suggests a considerable water run-back behavior occurring on the surface. As time goes on, the water transports downstream as indicated by the temperature increase at 20% chord length. The high LWC level provides sufficient amount of water that transports downstream, which makes the icing process extensively occurs over the airfoil. Latent heat of fusion is

thus extensively released over the icing region. And more heat is released at downstream locations, as far as 30% chord length, than that at the leading edge. Now consider the temperature variation at 30% chord length. It can be seen that there is a temperature increase from t = 0 to 1 s. This is obviously a result of water impingement at the initial state, which is in accordance with the temperature increase at upstream locations. At t = 1.5 s, another temperature increase is observed. This basically shows a time delay between water impingement and occurrence of water runback at 30% chord length. As ice accretion continues, surface water transports further downstream as indicated by the temperature at 40% chord length. It can be observed that after t = 6 s, the temperatures at all chord-wise locations tend to become constant, which suggests an equilibrium state. In this equilibrium state, as water constantly impinges on the surface, the latent heat of fusion is constantly removed by heat transfer along the airfoil. Ice features thicken as time goes on.

5.4.3 Evolution of Leading Edge Temperature Distribution

From the chord-wise temperature variations, it is noticed that the ice accretion mainly occurs around the leading edge. As water droplets impinge on the surface, ice starts to form around the leading edge and extend into the oncoming flow. The initially formed ice roughness essentially changes the air boundary layer flow and enhances the heat transfer process, which in turn, accelerates ice accretion. To better understand the initial transient icing process and the underlying heat transfer process, instantaneous temperature distributions around the leading edge are strongly desired.

Based on the time series of temperature distribution, the amount of local latent heat release could be estimated, which indicates the distribution of ice accretion. In this section,

the leading edge temperature distributions under various icing conditions are extracted from the time-resolved temperature measurements. The water run-back behavior, if in wet ice growth, will redistribute the surface water mass deposition, and hence, affect the local aerodynamics and heat transfer process. In dry ice growth, however, the collected water freezes immediately upon impact. The distribution of latent heat release along with the accreting ice is solely dependent on the distribution of local droplet collection efficiency. Thus, the knowledge of leading edge temperature distribution is of great importance in evaluating and analyzing an icing process and the underlying physical details. As discussed in the previous sections, LWC has a big effect on the icing morphology. Higher LWC tends to create wet ice growth and vice versa. To further quantify the distribution of droplets collection efficiency and local freezing ratio, the leading edge temperature distributions at LWC of 0.3 and 3.0 g/m^3 under a temperature of T_∞ = -8 °C and wind speed of 40 m/s are evaluated in this section. The corresponding icing morphologies under these conditions can be found in Table 5.2.

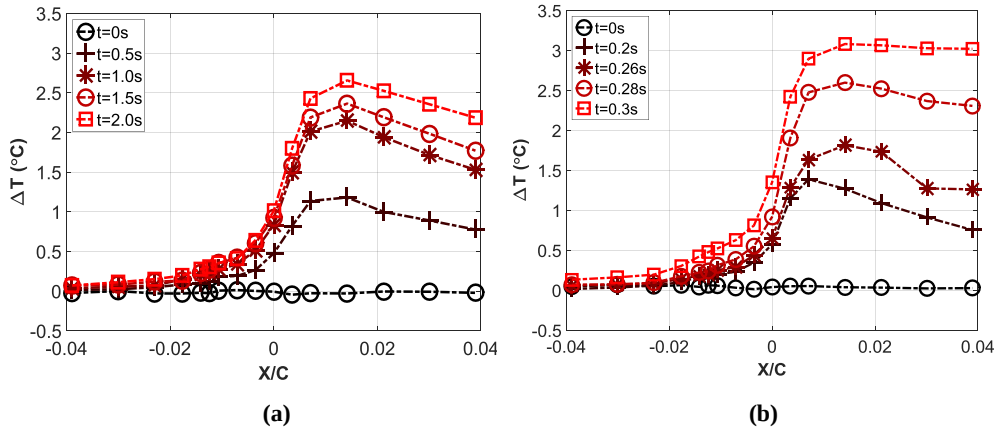

Figure 5.11 Temperature distribution around leading edge at T_∞ = -8 °C, V_∞ = 40 m/s and (a) LWC = 0.3 g/m^3. (b) LWC = 3.0 g/m^3.

The leading edge temperature distributions at an air temperature of -8 °C and wind speed of 40 m/s are shown in Figure 5.11. The chord-wise locations are all normalized by the chord length, with positive towards the trailing edge as shown in the figure. The evolution of temperature distribution at LWC of 0.3 g/m^3 is shown in Figure 5.11(a). It can be seen that before the water impingement (t = 0 s), the temperature is uniformly distributed at all locations, from upstream flow to the airfoil surface, indicated by the zero temperature increment as shown in the figure. As water droplets impinge on the airfoil surface, due to the heat release when the supercooled droplets freeze, the temperature around the leading edge increases as shown in the figure (t = 0.5 - 2.0 s). The ice accretion under this test condition is rime icing, in which there is no water run-back, and the amount of local ice accretion is solely determined by the local droplet collection efficiency. The amount of ice accretion is linearly related to the latent heat of fusion released in icing process. The distribution of heat release can be estimated by the temperature increment shown in the figure. Thus, based on the distribution of leading edge temperature increment, the distribution of leading edge water collection can be evaluated. During the initial water collection (t = 0 - 1.0 s), the leading edge temperature increases as more water is collected. It is noticed that as water impinges on the surface, the temperature distribution shows a dramatic increase starting from the leading edge, and reaches the maximum at the stagnation point (X/C = 0.014). Then, the temperature decreases gradually at the locations downstream. After the initial water collection (t = 1.0 - 2.0 s), the temperature distribution remains in a pattern in accordance with the distribution of local droplet collection efficiency as can be found in Özgen's modeling results (Özgen and Canıbek 2009). To

further validate this analogy, a parameter called *water collection ratio (WCR)* is defined, and denoted as θ. Assume the local water collection efficiency at any of the locations is β_i, and β_0 is the local water collection efficiency at the stagnation point, the *WCR* at the location is defined as

$$\theta_i = \beta_i / \beta_0 \tag{5.22}$$

*Table 5.3 Distribution of water collection ratio (*WCR*) around leading edge*

$\bar{X}/\bar{X}_{\beta max}$	*WCR* (Present experiments)	*WCR* (Özgen's model)
0.0	0.39	0.40
0.3	0.70	0.68
0.5	0.94	0.94
1.0	1.00	1.00
1.5	0.90	0.91
2.1	0.80	0.81
2.8	0.71	0.75

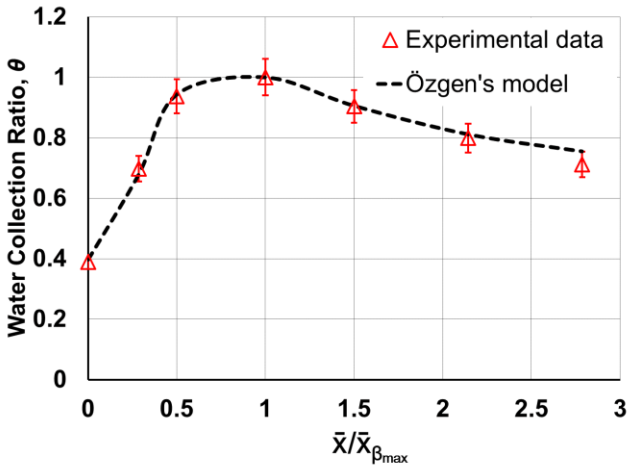

Figure 5.12 Comparison of water collection ratio (WCR) from the present experiments and Özgen's model.

For the rime icing process in this condition, the local *WCR*s around the leading edge are calculated based on the ratio of temperature increment at each location with that at the stagnation point. The *WCR*s calculated using this analogy are listed in Table 5.3, where $\bar{X}$

is the chord-wise location normalized by the chord length of the airfoil, and $\bar{X}_{\beta max}$ is the normalized location of the maximum water collection efficiency. Meanwhile, the *WCR* distribution can be extracted based on the distribution of droplet collection efficiency calculated using an extended Messinger model (Özgen and Canıbek 2009), as shown in Table 5.3. A comparison of the *WCR* distribution form the present experiments and Özgen's model is shown in Figure 5.12. It can be clearly seen that the *WCR* distribution measured in the present study agrees well with Özgen's modeling results. The water collection distribution, therefore, is well quantified based on the distribution of temperature increment around the leading edge, and can be used to further calculate the local freezing ratio for a glaze icing process.

The evolution of temperature distribution at an air temperature of -8 °C, wind speed of 40 m/s, and LWC of 3.0 g/m^3 is shown in Figure 5.11(b). As the LWC is significantly increased, the heat transfer is not adequate to remove all the latent heat of fusion in the collected water, the ice accretion presents a typical glaze icing that presents a clear water run-back process. It can be found in the figure that, at the very initial stage (t = 0.2 s), the temperature distribution is similar to that occurring in the initial stage of rime icing process (t = 0.5 s in Figure 5.11(a)), where there is a maximum temperature increment at X/C = 0.007. As time goes on, a lot of water droplets impinge on the surface, some of which splash and run back over the surface as indicated by the location shift of the maximum temperature increment (t = 0.26 s). As more water impinges and runs back over the leading edge area, the temperature at downstream locations is flattened out, and the temperature distribution presents a *stepped* increase (t = 0.28-0.3 s). Since the water collection ratio is

mainly determined by the airfoil shape and angle of attack, it can be assumed that the initial *WCR* distributions for both rime and glaze icing are the same as shown in Table 5.3. The *step*-shaped temperature distribution is due to the water run-back behavior that presents a uniform temperature distribution at downstream locations. In glaze icing, ice accretes along with the water transport. To quantify the amount of ice accretion in such conditions, another parameter, frozen water mass ratio (*FWMR*), is defined in this paper and denoted as φ. It is defined as the ratio of frozen water mass at a location and that at the stagnation location, and can be calculated using Eq. (5.22).

$$\varphi_i = \frac{m_{i,\,frozen}}{m_{0,\,frozen}} = \frac{\eta_i \cdot \sum_{k=0}^{i}\left[\theta_i \cdot \prod_{j=k}^{i-1}\left(1-\eta_j\right)\right]}{\eta_0} \tag{5.22}$$

where η_i and θ_i are the local freezing ratio and water collection ratio at the *ith* downstream location of the stagnation location.

Table 5.4 Freezing ratio at the stagnation point under different icing conditions

Temperature (ºC)	Wind Speed (m/s)	LWC (g/m^3)	Freezing Ratio (η)
-8	20	0.3	1.00
-8	40	0.3	0.94
-8	20	3.0	0.97
-8	40	3.0	0.91

Since the frozen water mass ratio, φ can be estimated based the distribution of temperature increment. For the distribution at t = 0.3s, the local freezing ratio at all locations can be calculated using Eq. (5.22). Using this methodology, the local freezing ratio at the stagnation point under different icing conditions can be calculated as listed in Table 5.4.

5.4.4 Convective Heat Transfer at Stagnation

Ice accretion on airfoil surface is a nonlinear process that involves unsteady mass and heat transfer due to droplet impingement, local freezing, and water run-back behavior. In this study, the transient convective heat transfer at the stagnation point will first be characterized to provide the basis of heat transfer evaluation over an ice accreting airfoil. Now recall the derivation of convective heat transfer coefficient in Eq. (5.20). The convective heat transfer process at the stagnation point can be quantified using the equation. Apply the local freezing ratio estimated in this study and the local water collection efficiency calculated in the previous research (Özgen and Canıbek 2009), the time-resolved heat convection coefficient at the stagnation point under different icing conditions can be calculated.

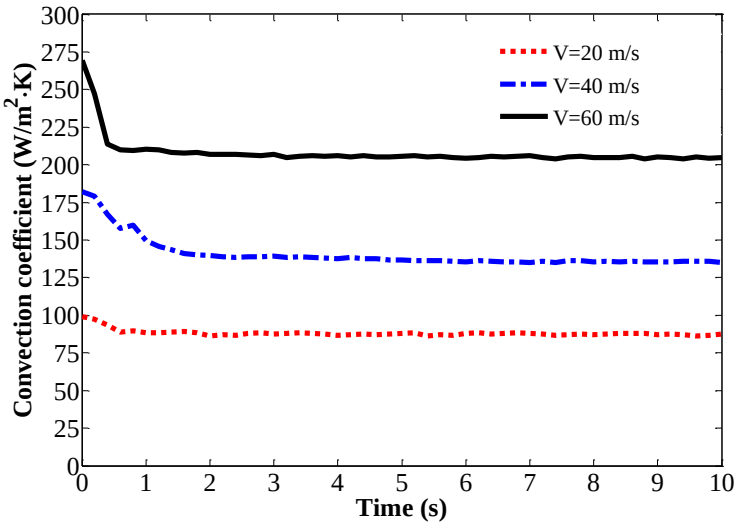

Figure 5.13 Time evolution of the stagnation heat convection coefficient at T_∞ = -8 °C and LWC = 0.3 g/m^3.

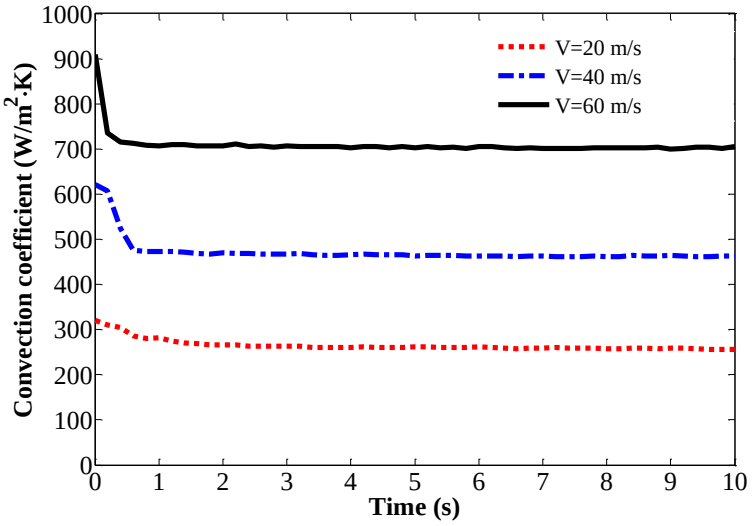

Figure 5.14 Time evolution of the stagnation heat convection coefficient at T_∞ = -8 °C & LWC = 3.0 g/m^3.

The time evolution of convective heat transfer at the stagnation point at a temperature of -8 °C and LWC of 0.3 g/m^3 are shown in Figure 5.13. It is clearly shown that higher wind speed reflects higher convection coefficient. As wind speed increases, the magnitude of $\partial T/\partial y$ in the thermal boundary layer at the surface becomes larger. Thus, the convection coefficient increases if the temperature difference between the surface and free-stream flow remains the same. On the other hand, the laminar boundary layer flow tends to transit to turbulence at higher wind speed. The turbulent flow structures are more intensive, which can essentially enhance the convective heat transfer. It is also found that there is a decrease of convection coefficient at the initial state of icing. This is mainly due to the formation of water film as water droplets initially impinge on the surface. The local turbulent intensity is lower at the gas-fluid interface as compared with that at a gas-solid interface. The convection in the boundary layer is thus reduced as shown in the figure. As

time goes on, water droplets continuously impinge on the surface and form into the film. Therefore, the convection coefficient stays the same afterward.

Figure 5.14 shows the evolution of convective heat transfer at the stagnation point at a temperature of -8 °C and LWC of 3.0 g/m^3. It can be clearly seen that the convection coefficients at different wind speed behave similarly as those at LWC of 0.3 g/m^3. The convective heat transfer is enhanced as wind speed increases. In the meantime, the increase of LWC could also enhance the convective heat transfer. It has been observed in many icing experiments (Hansman and Kirby 1987; Hansman and Turnock 1989; Hansman et al. 1991; Bragg et al. 1994; Waldman and Hu 2015) that there are bead-shape elements form upon the initial droplet impingement. These elements are the initial roughness that could essentially change the boundary layer flow, and enhance the convective heat transfer. Higher LWC tends to form more initial roughness elements, therefore, presents stronger heat convection.

5.5 Conclusions

In this study, an instant heat balance model on an ice accreting airfoil was formulated. A methodology based on infrared thermography was developed to achieve nonintrusive measurements of the transient heat transfer processes over an ice accreting NACA 0012 airfoil. Time-resolved temperature distributions on the ice accreting airfoil were acquired. The initial ice formation and accretion in both dry and wet icing conditions were characterized based on the temperature features in the distributions. Chord-wise temperature variations and evolutions were extracted to describe the ice formation and expansion under different icing conditions. The initial water collection is found to be

concentrated around the leading edge. The water transportation and ice formation were characterized based on the chord-wise temperature variations and evolutions.

Instantaneous temperature distributions around the leading edge were isolated to evaluate the transient details at the initial icing state. The ice morphology (dry or wet ice growth) can be recognized, and the stagnation point can be identified based on the temperature distribution in a dry ice growth. The initial water collection process was characterized based on the evolution of the leading edge temperature distribution under different icing conditions. The water collection distribution was evaluated based on the temperature distribution and presents a good agreement with the previous studies. For a wet ice accretion, the local freezing ration at the stagnation point was calculated based on the ratio of temperature increment at different locations.

Finally, based on the instant heat transfer model, the convective heat transfer at the stagnation point was characterized under different icing conditions. The convective heat transfer coefficient basically increases as the wind speed increases. Moreover, there is a significant magnitude decrease of convection during the initial water collection due to the boundary layer evolution from gas-solid to the gas-fluid interface. It is also found that LWC has a big effect on the heat convection. Higher LWC essentially provides more intense convective heat transfer due to the increase formation of initial roughness elements upon droplet impingement.

CHAPTER 6
EFFECT OF INITIAL ICE ROUGHNESS ON THE TRANSIENT WATER TRANSPORT PROCESS OVER A WING SURFACE

6.1 Introduction

Aircraft icing is widely recognized as one of the most serious threats to flight safety (Potapczuk 2013). Aircraft performance can be severely contaminated due to the icing caused stall margin reduction, drag increase, and lift decrease (Gent et al. 2000). It is documented that more than 1,100 icing-related accidents and incidents occurred in the US from 1978 to 2010 (Petty and Floyd 2004; Green 2006; Appiah-Kubi 2011). The in-flight ice formation and morphology are generally determined by icing cloud conditions (e.g., liquid water content (LWC), air temperature, and droplet size). As aircraft operate in the cloud with low LWC, small droplets, and cold temperatures (typically below -10 ºC), the droplets freeze immediately upon impact on the aircraft surface. Rime ice with rough, milky white appearance tends to form conforming to the aerodynamic shapes of aircraft. While under other cloud conditions with high LWC, large droplets, and temperature just below the freezing point, the impinged water runs back over aircraft surface before freezing downstream. Glaze ice forms with smooth, dense, and transparent appearance, and deforms into horn-like shapes as more water is transported and freezes (Hansman and Kirby 1987). These ice shapes extend into the airflow, and therefore, affect the aerodynamic and heat transfer characteristics. Glaze ice has been considered as the most dangerous icing hazards (Gent et al. 2000).

Accurate modeling and prediction of ice accretion could aid in the design of ice protection systems to mitigate icing effect and improve the determination of safety operating conditions (Tecson and McClain 2013a). However, the current icing simulation programs are limited in their capabilities to accurately predict glaze ice accretion, partly due to the use of simplified ice roughness models. In the LEWICE program, for example, ice roughness height is estimated based on the sand-grain equivalent model. As compared with the ice shapes produced in the icing experiments, the predicted ice shapes do not match well with the experimental results (Shin 1996; Vargas 2007). Initially formed roughness is suggested to be a key factor affecting icing process (Yamaguchi and Hansman 1992; Henry et al. 1994; Dukhan et al. 1996; Henry et al. 2000). As initial ice roughness forms, the boundary layer flow and heat transfer are essentially altered as well as the water collection and run-back process.

Many experimental studies have been conducted to evaluate the effect of simulated regular roughness (Henry et al. 1995; Kerho and Bragg 1995; Bragg et al. 1996; Winkler and Bragg 1996). Although the regular roughness is easy to implement, they may not reflect the irregularity and broad range of topographical scales of practical roughness (Bons and Christensen 2007). Different ice accretions have unique surface features that are not well captured by ordered arrays of discrete roughness elements. The use of regular roughness could create biases as compared with that using realistic roughness (Bons 2002; Mart et al. 2012). To better understand the effect of the actual ice roughness, various methods have been developed to create realistic ice roughness distributions (Rothmayer 2003; Tecson and McClain 2013b). Lagrangian droplet simulator is one of the recent

techniques that can generate roughness distributions with bead elements in random distribution and diameters (Tecson and McClain 2013a; Tecson and McClain 2013b). However, this method only operates with uniform droplet diameter, which differs from actual icing conditions. In recent years, laser-based and other optical scanning methods have been developed to accomplish three-dimension digitization of ice accretions (Lee et al. 2012). Recently developed 3-D laser scanners have been applied in generating 3-D point cloud containing details of ice roughness and shapes (Lee et al. 2014). An NACA 23012 airfoil with realistic ice roughness has been successfully recreated based on the 3-D scanning method (Liu and Hu 2016). The effect of the realistic roughness on the transient ice accretion and heat transfer process has been experimentally studied (Liu and Hu 2016). However, the microphysical details in water run-back process associated with glaze icing are still unknown, which is suggested to be of great importance in determining the morphology and growth of glaze ice (Du et al. 2010).

To quantify the microphysical details in water/ice transport process and evaluate the interaction between the initial ice roughness and surface water transport, advanced experimental techniques capable of providing accurate quantitative measurements of surface morphology are highly desired. The structured light technique developed in recent years have been successfully applied in reconstructing surface topographies. The basic methodology of this technique is to actively project known light patterns onto a surface, and extracting 3-D surface shapes from the images of the light patterns captured from one or more points of view (Salvi et al. 2010). As good space and time resolutions have been achieved, this technique is widely used in 3-D sensing, object recognition, robotic control,

industrial inspection of manufactured parts, stress/strain and vibration measurements, biometrics, biomedicine, dressmaking, and visual media (Salvi et al. 2010). In recent years, this technique has been introduced to measure fluid flow (Cazabat et al. 1990; Zhang and Su 2002; Cobelli et al. 2009; Hu et al. 2014). As the most recent progress, a digital image projection (DIP) technique was developed to quantify the surface water transport process over an NACA 0012 airfoil (Zhang et al. 2015). The microphysical details from droplet impingement to water film/rivulets formation and run-back were revealed based on the DIP measurements, which provides a decent method for measuring surface water/ice morphology. In the present study, a digital image projection-correlation (DIPC) technique developed from the DIP method was applied to provide non-intrusive, temporally resolved, and full-field measurements of the dynamic water/ice thickness distributions over the surface of an NACA 23012 airfoil.

In the sections that follow, the experiment methodology will first be described in detail. Then, the reconstruction and quantification of the instantaneous morphologies of the surface water/ice flow will be presented, in which, the effect of the initial ice roughness on the transient water/ice run-back behavior (e.g., water film wave formation and propagation, rivulets evolution and morphology) will be discussed and elucidated.

6.2 Experimental Methodology

6.2.1 Initial Ice Roughness Model

In the present study, An NACA 23012 airfoil was originally exposed to the icing conditions at NASA Icing Research Center to produce the initial ice roughness formation. Then the ice roughened airfoil was 3-D scanned into a point cloud file. As a typical reverse

engineering process, the point cloud was imported into a CAD software (CATIA-V5-R20 in this study) as shown in Figure 6.1(a). The imported point cloud was then manipulated (e.g., points filter, local and global points activate and remove) to generate a mesh surface containing the ice roughness features as can be seen in Figure 6.1 (b). The mesh surface is further operated by filling holes, flipping edges, and cleaning non-manifold meshes to create the airfoil surface with realistic ice roughness. Finally, the faces and solid body of the ice roughened airfoil were reconstructed. Wing models with smooth and rough leading edges (i.e., *SW* and *RW*) were finished and 3-D printed as shown in Figure 6.1(c) and Figure 6.1(d). It is evident that the roughness elements are in various shapes and sizes and randomly distributed around a smooth stagnation region, which is in consistence with the previous studies (Hansman et al. 1991). The parameters of the NACA 23012 airfoil are listed in Table 6.1.

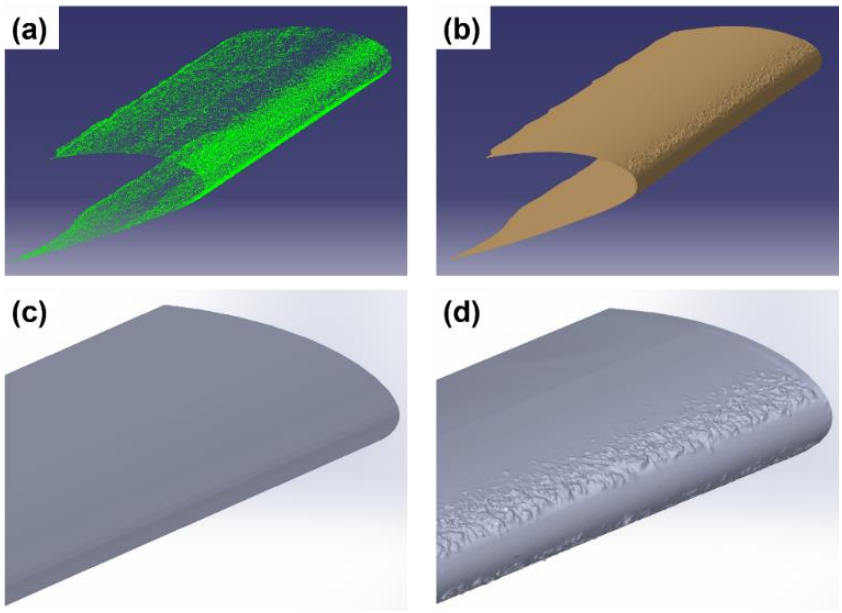

Figure 6.1 (a) Point cloud of the 3D scanned ice roughened NACA 23012 airfoil; (b) Mesh surface of the airfoil containing roughness features; (c) Wing model with smooth leading edge; (d) Wing model with rough leading edge

Table 6.1 Parameters of Wing Model

Airfoil Profile	Wing Spam	Chord length	Max Thickness	Max Camber
NACA 23012	406.4 mm	457.2 mm	54.86 mm at 29.8% chord	8.23 mm at 12.7% chord

6.2.2 Digital Image Projection-Correlation (DIPC) Technique

The digital image projection (DIP) technique has been reported in detail within Zhang's experimental study on the quantification of water transport process over an NACA 0012 airfoil (Zhang et al. 2015). In a typical DIP system, a digital projector is used to project image patterns with specific characteristics onto an object surface, while a digital camera is used to record image series. In the present study, a correlation based DIP technique was applied to quantify the transient water/ice runback process over the wing models.

6.2.2.1 Experimental Setup and Calibration Procedure

This experimental study was performed in the ISU Icing Research Wind Tunnel (ISU-IRWT). The icing research tunnel provides a unique facility for conducting fundamental experimental studies in icing-related scenarios. The icing wind tunnel can run over a range of test conditions to duplicate various atmospheric icing phenomena (e.g., from rime, mixed to glaze icing). The facility provides the capabilities to perform experiments at temperatures as low as -20 °C and wind speed up to 200 mph. A pneumatic spray system is integrated into the wind tunnel, which is capable of generating water droplets of 15–50 μm in diameter with liquid water content (LWC) adjustable to more than 5.0 g/m^3.

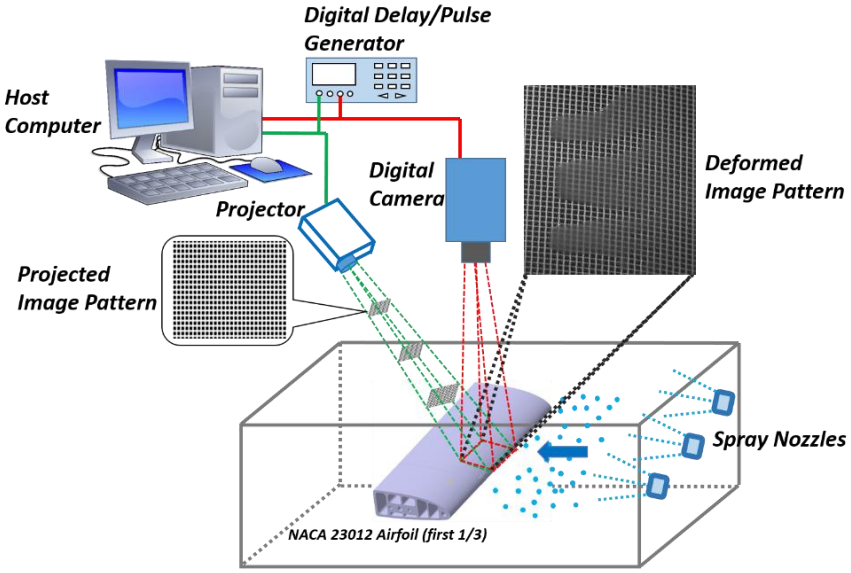

Figure 6.2 Schematic of experimental setup for digital image projection-correlation (DIPC) technique.

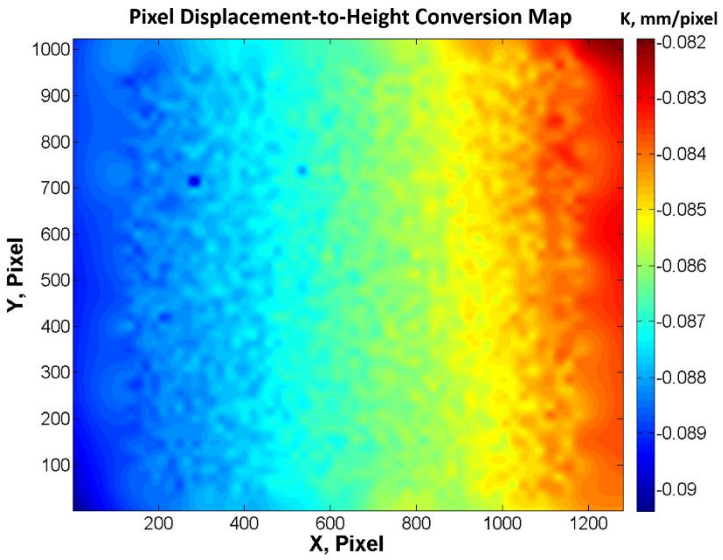

Figure 6.3 The displacement-to-height factor distribution in the measuring field.

The schematic of the experimental setup for the DIPC technique is shown in Figure 6.2. The experiments were conducted using a three-dimensionally printed test wing that spanned the width of the test section of the icing wind tunnel. Supported by a stainless

steel rod, the wing was mounted at oriented horizontally across the middle of the test section. The angle of attack was adjusted by pivoting the wing about the rod and fixing it at the desired angle measured with a digital inclinometer. The wing was finished with a coating of flat white paint and wet-sanded to a smooth finish using 2000 grit sand paper to improve the diffuse reflectivity of the projected grid images. A digital projector (DLP® LightCrafter™) was used to project the grid-patterned image as shown in the figure. A high-resolution 14-bit CCD camera (PCO sensicam with a maximum frame rate up to 400 Hz) with a 60 mm macro lens (Nikon, 60 mm Nikkor 2.8D) was mounted above the test section. The camera was positioned normal to the wing chord, providing a field of view of 1280 $\times$ 1024 pixels^2. As water film/rivulets appear on the wing surface, the grid pattern deforms; and the deformed pattern can be captured by the camera as can be seen in the figure. The digital camera and the projector were synchronized with a digital delay/pulse generator (BNC Model 575-8C). In this study, the frame rate for the image acquisition was set to 20 Hz to resolve the transient process of the surface water/ice run-back behavior over the wing models.

It has been derived in the previous study that the pixel displacement in a deformed image pattern is linearly related to the local height change at the corresponding point of interest (Zhang et al. 2015). By performing a calibration procedure similar as that described in the previous work (Hu et al. 2014; Zhang et al. 2015), the displacement-to-height conversion map (i.e., "$\boldsymbol{K}$" map) can be obtained. For the calibration in this study, the target plate with grid pattern was moved along the vertical direction. Then, the calibration images were collected at 27 parallel positions with an interval of 0.635 mm.

The pixel displacement map between each two successive images was derived by performing the cross-correlation algorithm (Zhang et al. 2015). Thus, the displacement-to-height conversion map in the measuring field can be integrated as shown in Figure 6.3.

6.2.2.2 Reconstruction of Water Film/Rivulets flow

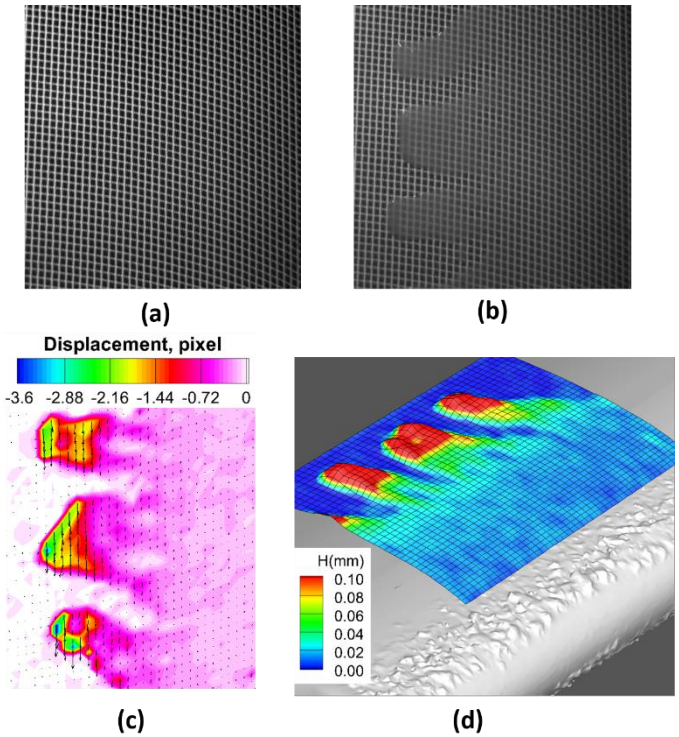

Figure 6.4 Typical raw images, pixel displacement map, and surface topography modulated in the DIPC method. (a) Reference image; (b) Deformed image with the presence of water film/rivulet flow; (c) Pixel displacement map; (d) Surface topography of the water/ice accreting wing

With the displacement-to-height conversion map, the surface water film/rivulets morphology can be reconstructed based on the pixel displacement distribution. Here, the routine operation for a typical raw image pair (including a reference image and a pattern-deformed image as can be seen in Figure 6.4(a) and Figure 6.4 (b)) acquired in the DIPC measurements will be described in brief. It can be found that the grid pattern in the

reference image is curved as fitting with the airfoil camber. All of the "Cross" units in the reference image can be detected and saved in a coordinate matrix. As water/ice appears on the wing surface, the grid pattern will deform as shown in Figure 6.4(b). Then, the coordinate matrix is applied to the deformed image as estimated "Cross" locations. For each estimated location, a cross-correlation algorithm will be applied and looped in a defined searching window around it to find the real "Cross" location. Thus, the displacement of each "Cross" unit can be determined as shown in Figure 6.4(c). By multiplying the displacement-to-height conversion factor, the local water/ice thickness can be calculated, and therefore, the full-field water/ice thickness distribution can be reconstructed as shown in Figure 6.4(d). It can be clearly seen that the film and rivulet shapes are well defined, and the surface morphology conforms well to the pattern-deformed raw image.

6.3 Results and Discussions

6.3.1 Quantification of Transient Water/Ice Runback Process

In the present study, two typical surface water morphologies were observed in various glaze icing trials: wave-modulated-film (WMF) flow and stripe-molded-rivulets (SMR) flow. It has been demonstrated that the surface morphology of the wind-driven water flow is highly dependent on the surface tension, inertia force in the advancing film/rivulets front and the aerodynamic force acting on it (Zhang and Hu 2016a). At low Reynolds number (low wind speed), the forces at the water film front are in equilibrium, and the WMF flow dominates the wing surface. As Reynolds number increases, the inertia force and aerodynamic force are increased, and the force balance at the advancing film front breaks,

due to which the film front breaks into rivulets, and the SMR flow develops (Zhang and Hu 2016b). In this study, to reproduce the water run-back process in glaze icing, the LWC was set to 5.0 g/m^3, and the air temperature was set at -5 °C. The WMF and SMR flow were modulated at a wind speed of 10 and 15 m/s, respectively.

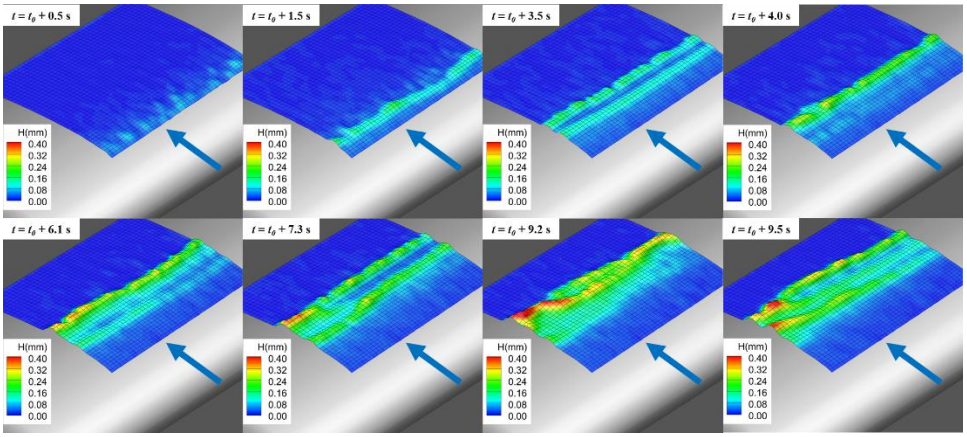

(a) Time evolution of the water film formation and propagation over the wing with a smooth leading edge.

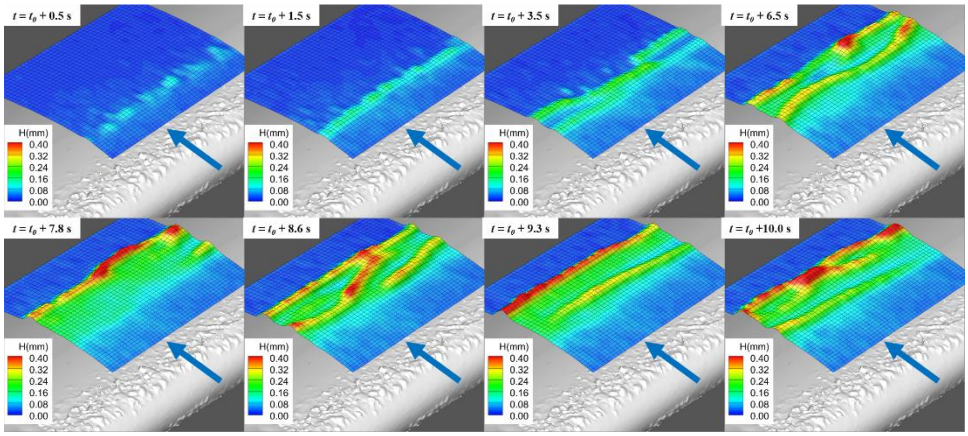

(b) Time evolution of the water film formation and propagation over the wing with a rough leading edge.

Figure 6.5 Time series of the transient water transport process over the wing surfaces at a wind speed of 10 m/s, LWC of 5.0 g/m^3, and an air temperature of −5 °C.

The time series of the water run-back process at a wind speed of 10 m/s are shown in Figure 6.5. When water impinged on the wing with smooth leading edge (SW) as shown in Figure 6.5(a), since the heat transfer was not adequate to remove all of the latent heat in the water droplets, they deformed and ran back under the effect of aerodynamic force (Liu and Hu 2016). The impinged water droplets were distributed according to the distribution of water collection efficiency. At the very early stage ($t = t_0 + 0.5$ s), the water droplets deformed and coalesced into beads around the leading edge, a portion of which can be found at the forefront of the measuring field as shown in Figure 6.5(a). As more water impinged onto the wing surface, the water beads ran back and merged into a water film with an evident wave (known as a primary wave) front as can be seen at $t = t_0 + 1.5$ s. Sheared by the boundary layer flow, the primary wave moved downstream as time goes on. In the meantime, more droplets were collected onto the surface and combined into the film flow. Under the effect of surface tension and aerodynamic force, secondary wave developed and moved downstream as can be seen at $t = t_0 + 3.5$ s. As the primary wave moved downstream, the secondary wave advanced over the wetted surface with a higher velocity and finally merged into the primary wave ($t = t_0 + 4.0$ s). Since the water droplets continuously impinged onto the wing surface, there was a periodical secondary wave formation and development ($t = t_0 + 4.0 \sim 9.5$ s). All of the secondary waves were finally merged into the primary wave as it advanced.

Now we come to the water film flow over the wing with a rough leading edge (RW) as shown in Figure 6.5(b). It can be seen that the measuring field was set right after the roughness. As water droplets impinged onto the wing surface, the initial roughness

essentially altered the water collection distribution and transport behavior (Liu and Hu 2016). It can be found that at the early stage ($t = t_0 + 0.5 \sim 1.5$ s), the first water wave (primary wave) front formed as the water droplets ran back and coalesced into a film. However, the location of the wavefront formation was found to start at further downstream as compared with the wave formation on the SW surface. It has been found that the initial ice roughness could trigger the boundary layer transition, which essentially thickens the air boundary layer and increases the skin-friction drag (Hansman et al. 1991). It is suggested that the retardation of the wave formation was due to the increased skin friction at the water film surface. As time goes on, the primary wave moved downstream, and multiple secondary waves formed and developed as can be seen from $t = t_0 + 3.5$ to 6.5 s. The secondary waves advanced over the wetted surface and finally merged into the primary wave ($t = t_0 + 7.8$ s). With time going on, more secondary waves developed downstream and advanced the primary wave ($t = t_0 + 7.8 \sim 10.0$ s).

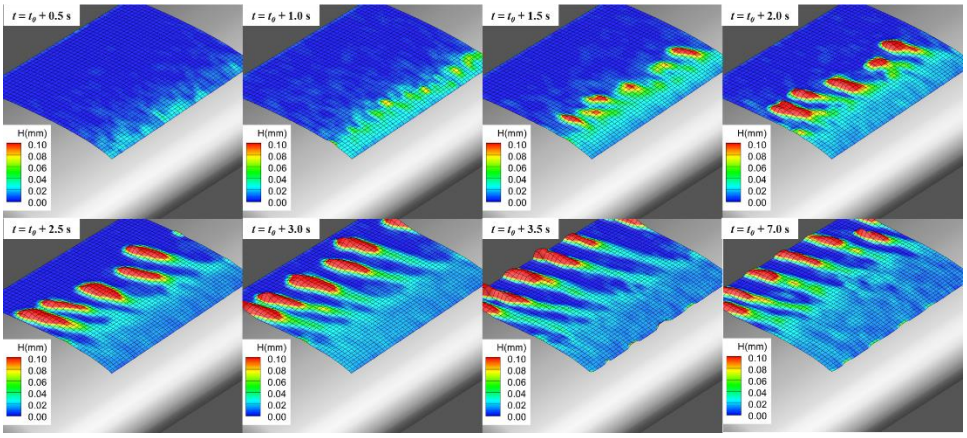

(a) Time evolution of the rivulets formation and development over the wing with a smooth leading edge.

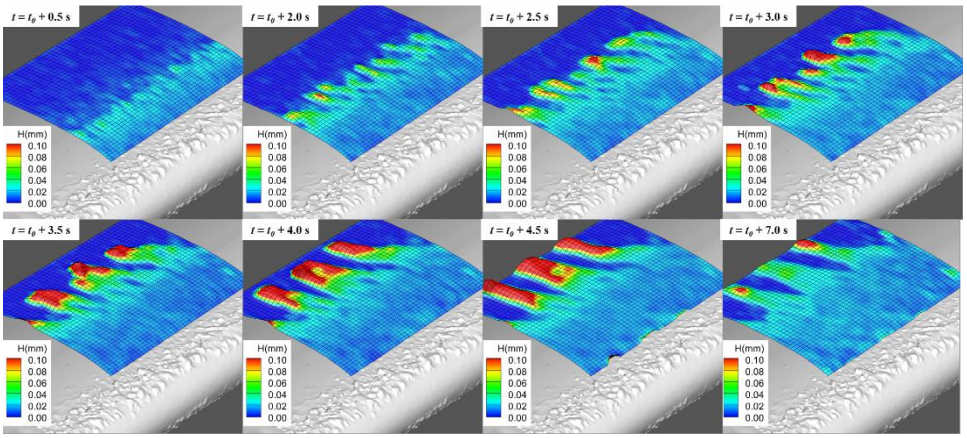

(b) Time evolution of the rivulets formation and development over the wing with a rough leading edge.

Figure 6.6 Time series of the transient water transport process over the wing surfaces at a wind speed of 15 m/s, LWC of 5.0 g/m^3, and an air temperature of −5 °C.

As wind speed increases to 15 m/s, the water transport presented evident rivulets flow over both SW and RW as shown in Figure 6.6. It has been demonstrated that the stability of the advancing water film is determined by the surface tension, the inertia force on the film front, and the aerodynamic force at the water/air interface (Zhang and Hu 2016b). As an apparent result of wind speed rise, the inertia force, and the aerodynamic force will increase while the surface tension remains the same. Thus, the force balance brakes and the film front breaks into multiple rivulets. For the water transport over the SW surface (Figure 6.6(a)), it can be observed that both film and rivulets features were presented in the water flow at the very early stage ($t \leq t_0$ + 1.0 s). As time goes on, the surface water ran back with more evident rivulets developing downstream as can be seen from $t = t_0$ + 1.0 to 2.5 s. During this process, the film/rivulets boundary also advanced as more water droplets were collected into the upstream film flow. As the rivulets moved further downstream, multiple isolated water transport channels were formed as shown in the

figure ($t = t_0 + 3.0 \sim 3.5$ s). These channels were turned out to be the main paths in transporting the water collected on the wing surface. It can be found that shortly after the channel paths formed, the wind-driven water flow became steady and showed a static surface morphology as can be seen from $t = t_0 + 3.5$ to 7.0 s. In this steady state, though the water droplets were continuously collected into the upstream film flow, the film/rivulets boundary only advanced a little as can be seen in the figure.

For the water transport over the RW surface, as shown in Figure 6.6(b), it can be clearly observed that the rivulets became wider, and the film/rivulets boundary developed further downstream as compared with that of the SW surface. As the impinged water droplets coalesced and traveled through the roughness elements, the film region was found to expand further downstream as can be seen at $t = t_0 + 0.5$ s. It has been experimentally proved that roughness arrays can trap and decelerate the surface water flow (Zhang et al. 2014). Therefore, it can be speculated that the realistic roughness in this study could trap and decelerate the water flow over the wing surface, though they are not in ordered arrays. Consequently, the inertia force in the water flow was reduced, which essentially delayed the breakup of the film front and the formation of rivulets. As time goes on, more droplets impinged on the surface, and the film broke into multiple rivulets as can be seen at $t = t_0 + 2.0$ s. It can be found that the initially formed rivulets presented evident meandering behavior. Based on the previous study, the meandering behavior is mainly caused by the non-uniformity of the advancing film front (Zhang and Hu 2016a). It has been demonstrated that realistic roughness with complex roughness topography could cause strong span-wise heterogeneities within the boundary layer flow (Barros and Christensen

2014; Liu and Hu 2016). It is suggested that the non-uniformity in the advancing film front was initiated by the realistic roughness distribution. Due to the nature of meandering behavior, the narrow rivulets tend to merge into wider rivulets as shown from $t = t_0 + 2.5$ to 3.5 s in the figure. As the rivulets merged and moved downstream, the film/rivulets boundary advanced. The initially formed rivulets were finally merged into three wide rivulets (in the measuring field) as can be seen at $t = t_0 + 4.0$ s. As more water was collected into the upstream film, the rivulets act as isolated water channels that transport the water to further downstream ($t = t_0 + 4.0 \sim 7.0$ s). While the water flow became steady in this process, the surface morphology with rivulet shapes was well defined as shown in the figure.

6.3.2 Effect of the Initial Ice Roughness on Water Wave Formation and Propagation

As has been noted in the depiction of the time series of the wave-modulated-film (WMF) flow (as shown in Figure 6.5), the most evident effect of the realistic roughness on the film flow is the retardation of the first wave formation. In order to further elucidate the retardation effect, we calculated the span-averaged chord-wise thickness distributions at different times for both SW and RW as shown in Figure 6.7. For the wave formation and development over the SW surface, the first wave started to form at 2% chord length as can be seen in Figure 6.7(a). As the wave is advanced, the wave amplitude increased as shown in the figure. It can be found that at $t = t_0 + 3.0$ s, the first wave formation was nearly completed, and the wave crest was located at 3.6% chord length. According to the definition above, this first wave is called primary wave as it is the wave with the maximum amplitude. The primary wave is also known as the film front advancing over the dry

surface downstream. With time going on, more water was collected into the film flow, and a secondary wave started to form as can be seen at $t = t_0 + 3.7$ s. After that, the secondary wave developed and advanced over the wetted surface before merging into the primary wave. Then, a periodical secondary wave formation and development can be observed as described in the above section. During this process, the primary wave advanced over the dry surface as the continuous coalescence occurred.

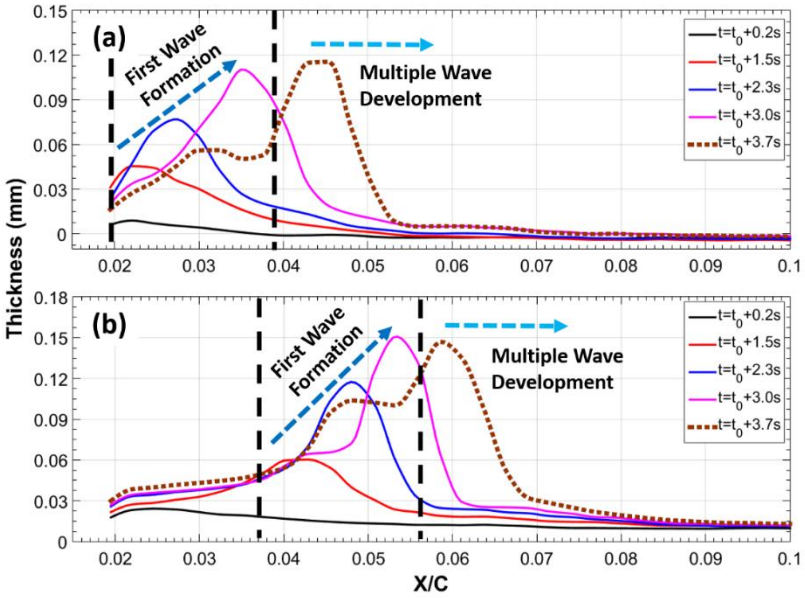

Figure 6.7 Time evolution of chord-wise thickness distribution over the wing with (a) smooth and (b) rough leading edge at a wind speed of 10 m/s, LWC of 5.0 g/m^3, and an air temperature of −5°C.

The time history of the primary wavefront locations is shown in Figure 6.8. It can be found that as time goes on, the primary wave moved downstream with a decreasing velocity as indicated by the reducing local slope along the curve as shown in the figure. As the primary wave moved over 8% chord length, the wave velocity became very slow as indicated in the figure. As a typical glaze icing process, the latent heat in the water film

was removed by the heat transfer as it moved downstream, in which process, the water froze and glaze ice formed (Liu et al. 2015).

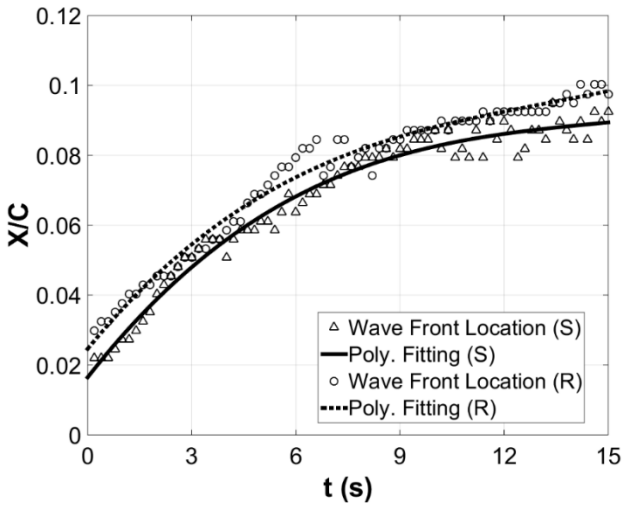

Figure 6.8 Time history of the primary wavefront locations in the water film flow over the wing with smooth (S) and rough (R) leading edge at a wind speed of 10 m/s, LWC of 5.0 g/m^3, and an air temperature of −5°C.

Now we take a look at the wave formation and development over the RW surface as shown in Figure 6.7(b). It can be found that the primary wave started to form at further downstream (3.8% chord length) as compared that over the SW surface. After a similar wave formation process, the primary wave advanced to about 5% chord length before the first secondary wave formed. An evident retardation of the primary wave formation can be concluded based on the comparison here. It is also noticed that at $t = t_0 + 3.0$ s, the first secondary wave had started to form into shape on the wing surface, which was not found for SW at the same time point. That means the duration of wave formation became shorter as the leading edge roughness altered the boundary layer flow. As the primary wave moved downstream, the secondary wave formed and developed as can be seen in the figure. In order to evaluate the effect of the leading roughness on the water wave propagation, the

time history of the primary wavefront locations over the wing with initial roughness is also plotted as shown in Figure 6.8. It can be found that the curve is basically parallel to the one for SW, meaning that the advancing velocities of the primary waves over the two wing surfaces were nearly the same along the time axis. It also can be noted that both of the primary waves slowed down as they advanced to about 8% chord length as indicated in the figure, which is suggested to be caused by the freezing process along with the surface water run-back process.

6.3.3 Effect of the Realistic Roughness on Rivulets Characteristics

As wind speed increases to 15 m/s, the surface morphology of the water transport presented evident rivulet shapes over both the SW and RW surfaces. Since the final rivulets shape is essentially determined by the initial rivulets formation and development process, more details during this process will be discussed in this section.

$$\eta = \frac{wetted\ area}{total\ area} \tag{6.1}$$

Here, we proposed a new method for recognizing the rivulets formation location and the film/rivulets boundary based on the DIPC measurements. Since the time-resolved surface water morphologies have been successfully reconstructed as shown in Figure 6.6, the thickness distribution of the water film/rivulets flow can be quantified. Then, the dry area and wetted area can be distinguished based on the water thickness distribution. For each chord-wise location, the water coverage ratio (denoted as η in this study) can be calculated using Eq. (6.1). If η = 100%, the whole area is wetted, indicating a film morphology at the chord-wise location. Otherwise, only part of the area is wetted, and rivulets present at the location.

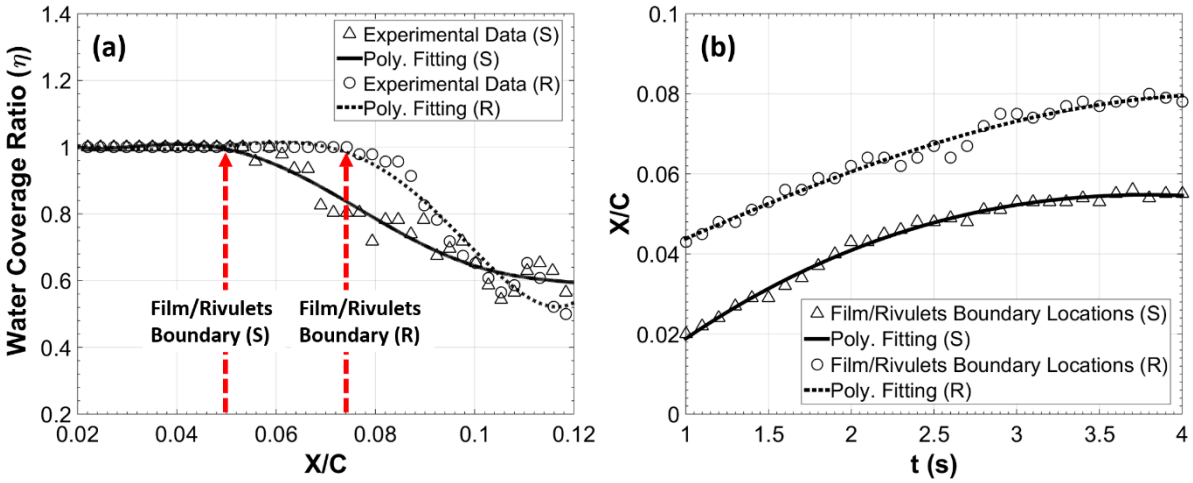

Figure 6.9 Effect of the leading edge roughness on rivulets formation and development at a wind speed of 15 m/s, LWC of 5.0 g/m^3, and an air temperature of −5°C. (a) Chord-wise distributions of water coverage ratio over the wing with smooth and rough leading edge. (b) Time history of water film/rivulets boundary locations over the wing with smooth and rough leading edge.

To illustrate the recognization process of the rivulets formation or film/rivulets boundary, we take the instantaneous water film/rivulets morphologies at $t = t_0 + 2.8$ s for example. According to the definition, the chord-wise distribution of the water coverage ratio (η) for the water flow over the two wing surfaces can be derived as shown in Figure 6.9(a). Based on the distribution curves, the film/rivulets boundaries can be easily recognized as indicated in the figure. It can be seen that the film/rivulets boundary of the water flow over the SW surface is located at 5% chord length while the boundary over the RW surface is located at 7.4% chord length. Here, we can conclude that the water film region is extended due to the existence of the leading edge roughness. In the rivulets region, it can be noticed that the water coverage ratio decreases at further downstream, indicating a transient stage of the rivulets development. As the rivulets are fully developed, the curves

start to become flatter as can be seen in the figure. The constant level of water coverage ratio is lower for RW, indicating a smaller wetted surface area.

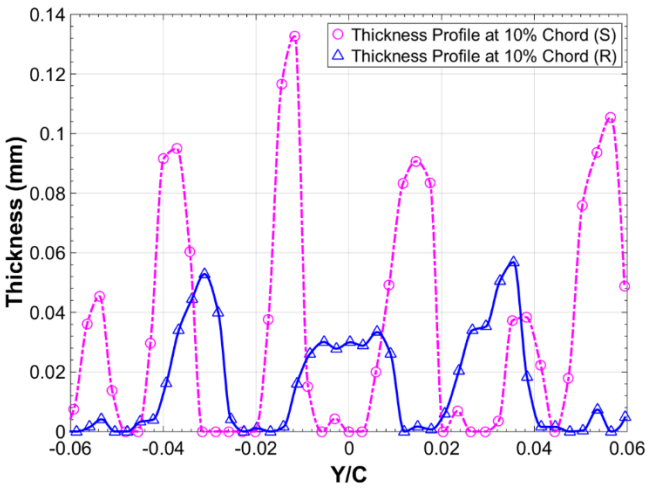

Figure 6.10 Time-averaged span-wise thickness profiles in steady state at 10% chord length of the wing with smooth (S) and rough (R) leading edge at a wind speed of 15 m/s, LWC of 5.0 g/m^3, and an air temperature of −5°C.

If we perform this recognization process for each surface morphology in time series, the time evolution of the film/rivulets boundaries can be extracted as shown in Figure 6.9(b). From the evolution curve for SW, it can be seen that the rivulets start to form at 2% chord length. As time goes on, the film/rivulets boundary moves downstream with a decreasing velocity as indicated by the reducing local slope along the curve as shown in the figure. After $t = t_0 + 3.5$ s, the curve becomes flat, and film/rivulets boundary settles down at 5.6% chord length. Now, we look at the evolution curve for RW. The rivulets started to form at 4.2% chord length, and settles down after $t = t_0 + 3.8$ s at 8% chord length as can be seen in the figure. As has been mentioned above, the realistic roughness could effectively trap and decelerate the water film flow, which essentially decreases the inertia force within the film front, and delays the rivulets formation. It can be found that

the two evolution curves are nearly parallel, indicating that the advancing velocities of the two film/rivulets boundaries are very close at each time point.

Table 6.2 Characteristics of the Rivulets at 10% Chord of the Wing

Leading Edge Condition		Rivulet #1	Rivulet #2	Rivulet #3	Rivulet #4	Rivulet #5	Rivulet #6
Smooth	Rivulet Center Location (Y/C)	-0.056	-0.038	-0.014	0.012	0.038	0.056
	Rivulet Width (w/C)	0.014	0.014	0.014	0.016	0.014	0.016
	Rivulet Height (mm)	0.046	0.096	0.132	0.092	0.040	0.106
Rough	Rivulet Center Location (Y/C)	-0.032	0.000	0.030	N/A	N/A	N/A
	Rivulet Width (w/C)	0.024	0.026	0.024	N/A	N/A	N/A
	Rivulet Height (mm)	0.054	0.032	0.058	N/A	N/A	N/A

Based on the above analysis, it can be noted that as time goes on, the film/rivulets will settle down, and the rivulets flow will enter the steady state. To evaluate the rivulets shape in the steady state, we calculated the time-averaged thickness distribution from $t = t_0 + 5.0$ to 10.0 s. Then, the span-wise thickness profiles at downstream locations where rivulets dominate can be isolated to provide quantitative facts about the rivulet characteristics. The time-averaged span-wise thickness profiles at 10% chord length of the wing with smooth

(S) and rough (R) leading edge are shown in Figure 6.10. From the thickness profiles, the parameters of the each rivulet can be isolated as shown in Table 6.2. Based on the rivulet center locations, the spacings between the rivulets can be estimated, and the average spacings of the rivulets on SW and RW are 2.2% and 3.1% chord length, respectively. It is evident that the rivulets become wider as the initial roughness forms around the leading edge as can be seen in the table. The average rivulet height also can be calculated, which turns out to be 0.085 mm and 0.048 mm for SW and RW, respectively. Therefore, it can be concluded that the initial ice roughness has a significant effect on the downstream rivulets characteristics.

6.4 Conclusions

In the present study, an experimental study of the effect of initial ice roughness on the transient water/ice run-back process in glaze ice accretion over an NACA 23012 airfoil was performed in the ISU Icing Research Wind Tunnel (ISU-IRWT). A digital image projection-correlation technique was used to provide non-intrusive, temporally resolved, and full-field thickness measurements of the water/ice transport process.

The instantaneous surface morphologies of the water film/rivulets flow over the wing with different leading edge conditions (smooth and rough) were successfully reconstructed and quantified. Two typical surface water morphologies were observed in various glaze icing trials: wave-modulated-film (WMF) flow and stripe-molded-rivulets (SMR) flow. In the WMF flow, one primary wave and multiple secondary waves present as the water film moves downstream; while in the SMR flow, upstream film flow with multiple downstream rivulets development can be observed.

The initial ice roughness is found to be able to retard and shorten the primary wave formation in the WMF flow while the wave velocity was not affected. For the SMR flow, the initial ice roughness is found to trap and decelerate the water film flow and decrease the inertia force in the film front, which essentially delays the rivulets formation. The roughness trapped flow also presented a meandering behavior during the initial rivulets formation, due to which, the initially formed rivulets merged into wider rivulets.

As a new method was proposed to recognize the film/rivulets boundary, the instantaneous chord-wise distribution of water coverage ratio was acquired, from which the dynamic process of film/rivulets boundary, rivulets transition and development were quantified. The time evolution of film/rivulets boundary was also established, from which the advancing velocity of the film/rivulets boundary was found not affected by the initial ice roughness.

For the steady state water film/rivulets flow, the time-averaged thickness profile was derived. The characteristics of the steady-state rivulets flow were also extracted. The initial ice roughness was demonstrated to have a significant effect on the rivulet shape (e.g., rivulet width, spacing, and height).

CHAPTER 7
EFFECT OF INITIAL ICE ROUGHNESS ON THE TRANSIENT ICE ACCRETION AND HEAT TRANSFER OVER A WING SURFACE

7.1 Introduction

Aircraft icing has been recognized as a big threat to flight safety for several decades (Potapczuk 2013). The flight performance of an aircraft encountering icing clouds can be significantly contaminated by the ice accumulated on critical surfaces (Cebeci and Kafyeke 2003). Ice accretions could negatively affect the aerodynamic performance of aircraft by reducing stall margin, increasing drag, and decreasing lift (Gent et al. 2000). It is documented that more than 1,100 accidents and incidents occurred in the US from 1978 to 2010 (Petty and Floyd 2004; Green 2006; Appiah-Kubi 2011). A considerable amount of the incidents were related to in-flight icing occurring on the wings, fuselage or control surfaces. Many essentials during these icing processes, however, are still not fully understood.

The in-flight ice formation and accretion are highly dependent on weather conditions, e.g., cloud liquid water content (LWC), atmosphere temperature, and cloud droplet median volumetric diameter (MVD). Various ice shapes have been produced under different icing cloud conditions (Shin and Bond 1992; Vargas and Tsao 2008). In the past years, many efforts have been made to characterize the effects of LWC, air temperature and velocity, and droplet size on ice shape formations (Hansman and Kirby 1986; Gent et al. 2000; Cebeci and Kafyeke 2003). Clouds with low LWC and small droplets at cold temperatures (typically below -10 ºC) tend to produce ice shapes with rough, milky white appearance

conforming to aircraft surfaces. While under other cloud conditions with high LWC and large droplets at temperatures just below the freezing point, some erratic ice horns with clear, smooth, and dense appearance may form and extend into the oncoming flows (Hansman and Kirby 1987).

It has been concluded that the heat transfer is one of the most essential mechanisms that control the ice shape accretion (Yamaguchi and Hansman 1992). Ice forms as the heat transfer remove the latent heat in the collected water. If the heat transfer is adequate to remove all of the latent heat of fusion in the water, the collected droplets will freeze immediately upon impact; if not, a portion of the water will run back over aircraft surfaces and freeze over a larger area extending to further downstream. Many experimental studies, either in-flight or ground wind tunnel test, have been conducted to evaluate the heat transfer process pertinent to icing events (Arimilli et al. 1984; Hansman and Kirby 1987; Poinsatte et al. 1989). It was shown that the heat transfer is significantly affected by the roughness elements formed in the initial stage of ice accretion. Further studies revealed that the initial ice roughness is significant because it couples the fluid flow, droplet impingement, and heat transfer processes (Olsen and Walker 1986; Yamaguchi and Hansman 1992; Henry et al. 1994; Dukhan et al. 1996; Henry et al. 2000). The initial ice roughness essentially induces higher levels of turbulence in the airflow and accelerate the convective heat transfer from the surfaces to freestream (Vargas 2007).

Based on the heat transfer models in the various ice accretion processes, there are multiple heat transfer mechanisms occurring on the airfoil/ice surfaces during ice accretions (Myers 2001; Fortin et al. 2006), among which, convective heat transfer is

considered to be predominant in aircraft icing (Dukhan et al. 2003; Liu et al. 2015). Since the initial ice roughness is closely coupled with the local flow field and convective heat transfer, even a slight change in roughness characteristics (element size, element spacing, etc.) could essentially impact the convective heat transfer, and hence, change the amount and rate of ice accretion (Tecson and McClain 2013a). Therefore, it is important to accurately characterize the initial roughness elements for the further prediction of final ice shapes and sizes.

It is of great importance to precisely predict ice accretion events to aid in the design of ice protection systems to mitigate icing effects, and furthermore, to improve the determination of safety operating conditions (Tecson and McClain 2013a). During the past years, some ice accretion prediction codes have been developed to simulate icing process from water droplet trajectory calculations to ice growth on aircraft surfaces. One of the most commonly used codes is the Lewis ice accretion program (LEWICE) from NASA. The LEWICE program combined a potential flow calculation, droplet trajectory analysis, and a mass and energy balance to predict ice growth (Potapczuk 2013). However, the current ice accretion codes are limited in their capabilities in predicting ice accretion, partially due to the use of simplified ice roughness models. In the LEWICE, the ice roughness height is estimated based on the sand-grain equivalent model. Convective heat transfer is then determined as coupled with the ice roughness height estimation (Wright 1999). This simplification could essentially affect the ice accretion shape and size because the sand-grain roughness is different from the real ice roughness as found in the previous icing experiments (Shin 1996). Based on the comparison of the ice shapes generated in

the icing experiments and that from the LEWICE program, it was found that the predicted ice shapes did not match well with the experimental results. The comparison, consequently, presented a poor agreement of the convective heat transfer coefficients (Shin 1996; Vargas 2007).

Many experimental studies have been conducted to provide realities of the effects of the roughness elements on the local convective heat transfer and boundary layer development. However, since the initial ice roughness is difficult to characterize, most of these studies were focused on the effects of the non-realistic ice roughness, or simplistically distributed roughness (Henry et al. 1994; Bragg et al. 1994; Henry et al. 1995; Kerho and Bragg 1995; Bragg et al. 1996; Winkler and Bragg 1996). Although these simulated roughness characterizations are easy to implement, they may not reflect the irregularity and broad range of topographical scales of practical roughness (Bons and Christensen 2007). Different ice accretions have unique surface features that are not always well captured by ordered arrays of discrete roughness elements. The use of these non-realistic ice roughness is proved to create biases in convective heat transfer results as compared with that using realistic distributions of roughness elements (Bons 2002; Mart et al. 2012). Assessing the impact of realistic roughness features on the initial ice accretion and heat transfer process is critical to improving the accuracy of ice accretion prediction.

Over the years, several techniques have been developed to create realistic ice roughness distributions (Rothmayer 2003; Tecson and McClain 2013b). One of the recent techniques is a Lagrangian droplet simulator, which can be used to generate realistic ice roughness distributions (Tecson and McClain 2013a; Tecson and McClain 2013b). The

resultant roughness is a bead distribution with random distribution and diameters. This approach enables the characterization of boundary layer development and convective heat transfer from surfaces exhibiting such kind of roughness distributions(Tecson and McClain 2013a). The real ice roughness elements from real icing conditions may be of various shapes and sizes. In order to better understand the boundary layer flow and local heat transfer in these situations, another approach employing cast surfaces of real icing models was developed (Dukhan et al. 2003). The three-dimensional features of ice accretion can be captured using the mold and casting method. However, this approach is time-consuming in operation, and the cost can be significant (Lee et al. 2012). In recent years, laser-based and other optical scanning methods have been developed to accomplish three-dimension digitization of ice accretion (Lee et al. 2012). The 3-D laser scanners developed in recent years were proved to be capable of accurately recording and reproducing the details of ice formations (Lee et al. 2014).

In this study, an NACA 23012 airfoil with initial ice roughness formed in NASA research center was 3-D scanned. The point cloud of the ice roughened airfoil was generated and used to rebuild the airfoil shape with realistic ice roughness. For comparison, Another NACA 23012 airfoil with smooth leading edge was also modeled. Icing experiments were performed in the ISU Icing Research Wind Tunnel (ISU-IRWT). A high-speed videography was used to visualize the icing process including droplet collection, ice formation, water run-back, and ice accretion. The time sequence of the icing process was recorded, based on which, the ice formation and evolution were extracted from the frames of the high-speed video sequence. An infrared thermometry combined

with thermocouple measurements was also applied to map the temperature distribution over the ice accreting airfoil surfaces. This temperature measurement provides insight into the initial droplet collection distribution and the heat transfer process during icing. The effect of the realistic ice roughness on the droplet collection distribution and the heat transfer enhancement were elucidated.

7.2 Experimental methodology

7.2.1 Construction of Airfoil Model with Realistic Ice Roughness

The test model used in this study is an NACA 23012 airfoil with realistic initial ice roughness. The initial ice accretion was made and 3-D scaned in the NASA Icing Research Center. A point cloud data file was provided in this study to rebuild the airfoil model with realistic ice roughness. The construction of the solid airfoil model from the point cloud data is a typical reverse engineering project. The point cloud file was imported into a 3D CAD software (CATIA-V5-R20 in this study) as shown in Figure 7.1(a). The imported point cloud was then manipulated (e.g., points filter, local and global points activate and remove) to generate a mesh surface containing the ice roughness features as can be seen in Figure 7.1(b). The mesh surface is further treated by filling holes, flipping edges, and cleaning non-manifold meshes to create the airfoil surface with realistic ice roughness. Finally, the faces and solid body were generated by using the Quick Surface Reconstruction (QSR) module in the CAD software. Figure 7.2 shows the realistic ice roughness features around the airfoil leading edge. It can be clearly seen that the roughness elements are of various shapes and sizes and randomly distributed while the stagnation

region presents a smooth surface that is consistent with the previous studies (Hansman et al. 1991).

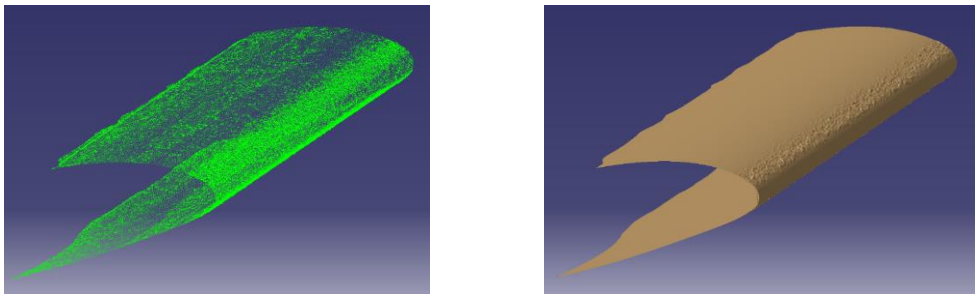

(a) (b)

Figure 7.1 (a) Point cloud of the 3D scanned ice roughened NACA 23012 airfoil; (b) Mesh surface of the airfoil containing ice roughness features.

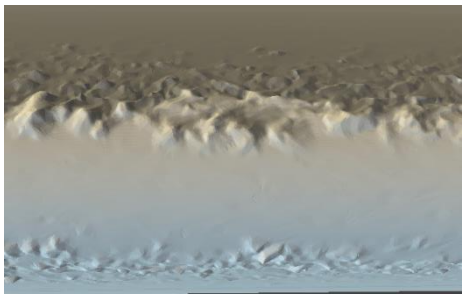

Figure 7.2 Zoom-in of the airfoil leading edge with ice roughness features.

7.2.2 Experimental Setup

The experiments were carried out in the ISU Icing Research Wind Tunnel (ISU-IRWT) as shown in Figure 7.3. The icing research tunnel provides a unique facility for conducting aerodynamic and heat transfer research under icing conditions. The facility provides the capabilities to perform experiments at temperatures below -20 °C and wind speeds up to 200 mph. A pneumatic spray system generates water droplets 15–50 μm in diameter with the liquid water content adjustable to more than 3.0 g/m^3. Replaceable test section panels allow different windows for visible or infrared imaging experiment.

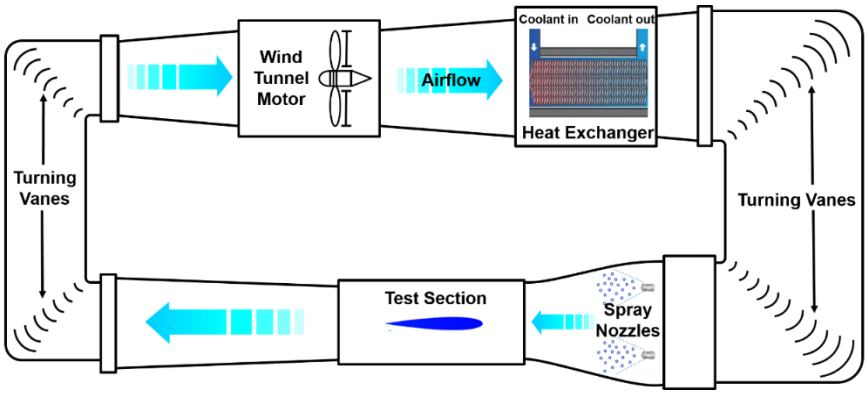

Figure 7.3 Schematic of the ISU Icing Research Wind Tunnel (ISU-IRWT).

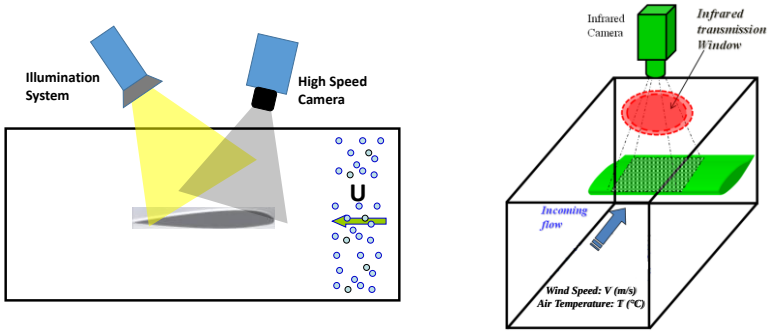

Figure 7.4 Schematic of the experimental setup for (a) High-speed videography; (b) Infrared thermography.

High-speed video was recorded using a high-resolution 14-bit CCD camera (PCO sensicam with a maximum frame rate up to 400 Hz) mounted 0.5 m above the wing using a 60 mm macro lens (Nikon, 60 mm Nikkor 2.8D). The camera was positioned normal to the wing chord, providing a top-down view with a 1280 $\times$ 1024 pixels^2 field of view and a pixel resolution of 11.7 pixels/mm. Low-flicker illumination was provided by a pair of 150 W fiber-coupled halogen lamps (AmScope, HL250-AS). The experimental configuration is illustrated in Figure 7.4(a).

A schematic of the experimental setup for infrared imaging measurements is shown in Figure 7.4(b). An infrared transmission window (FLIR IR Window-IRW-4C) with a

diameter of 101.6 mm was set in the top panel of the test section. An infrared (IR) camera (FLIR A615) was mounted above the IR window as shown in the figure. The wavelength range that can be detected by the camera sensor is from 7.5 to 14 μm. The resolution of the camera is 640 × 480 pixels, which is capable of providing high accuracy of measured temperatures spotting even small objects from a distance. FLIR A615 adopts a new camera interface standard, GigE Vision that allows for fast image transfer. The camera can achieve a 16-bit temperature linear output at frequencies up to 200 Hz.

The experimental trials presented here were conducted at air temperatures of T = −15 and -5 °C and freestream velocity of U = 40 m/s, and the liquid water content for each trial was LWC = 3.0 g/m^3.

7.2.3 Measurement Calibration

In the IR imaging measurements, the IR camera was mounted above the measuring object at a distance of 215 mm. The infrared radiation from the airfoil and ice/water can be transmitted through the IR window with a transmission coefficient of 0.82. The emissivity coefficients of airfoil surface, ice, and water are listed in Table 7.1. To validate the IR imaging measurements, a temperature calibration procedure is required. The IR camera was present with the given parameters. A spot temperature measurement on the airfoil surface was conducted both using the IR camera and a thermocouple. The temperature range in the calibration process is from -17 to 1 ºC. A comparison of temperatures measured by the IR camera and a thermocouple is shown in Figure 7.5. It shows that the temperatures measured by the IR camera and the thermocouple agree well,

validating the infrared tomography in achieving accurate temperature measurements over the airfoil.

Table 7.1 Emissivity coefficients of materials used in the measurements

Material	Emissivity
Airfoil surface (Paint: oil white)	0.95
Ice	0.965
Water	0.95-0.963

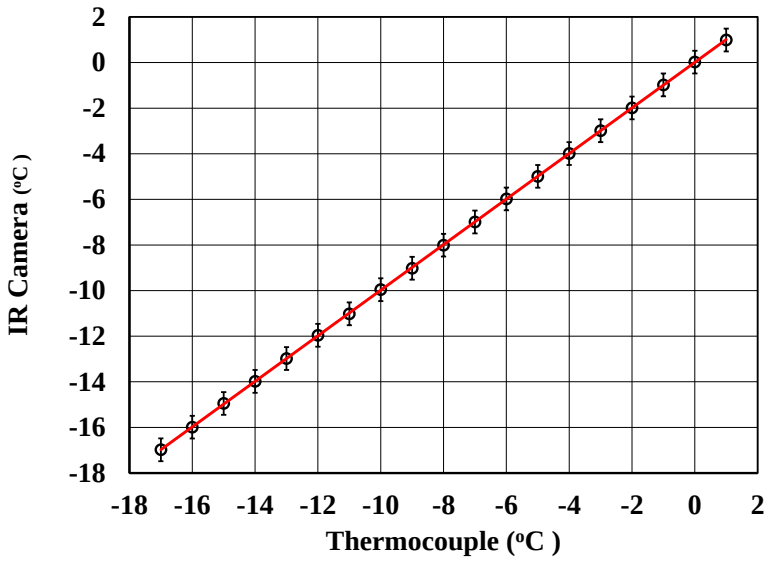

Figure 7.5 Comparison of temperature measured by the IR camera and a K-type thermocouple

7.3 Visualization of Transient Initial Ice Accretion

In the present study, the ice accretion process over the wing model was first visualized and examined using the high-speed videography. Here, typical ice accretion trials over the two surface conditions at U = 40 m/s and LWC = 3.0 g/m^3 are presented. Then, the effect of the realistic ice roughness on ice accretion as the air temperature changes is examined. The initial ice accretion process on the pressure side of the NACA 23012 airfoil at

temperature T = −15 °C is given in Figure 7.6. For the ice accretion on the smooth airfoil (Figure 7.6(a)-(e)), the ice accretion exhibits characteristics in agreement with previous works on icing (Waldman and Hu 2015). First, the impinging water droplets are collected around the leading edge (Figure 7.6(a)). As more water impinges on the wing surface, a film region forms as shown in Figure 7.6(b)-(e). In the meantime, sparse roughness spots can be observed behind the film region. Since the temperature is fairly cold, the impinged water droplets freeze immediately upon impact. There is no run-back icing can be observed under this condition. In the initial icing stage (t = 1-4 s), the water droplets impinge and freeze on the wing surface, forming an extending smooth ice film (Figure 7.6(b)-(d)). As time goes on, more droplets impinge on the formed ice surface and freeze instantly, which thickens the ice film at the leading edge, while the chordwise extent of the smooth ice film remains the same (Figure 7.6(d)-(e)). A distinct straight boundary between the smooth ice film and the rough spots region can be seen in the figures, which indicates the ice accretion around the smooth leading edge is uniform along spanwise. Since the ice accretion distribution in rime icing is solely determined by the water collection efficiency distribution (Hansman et al. 1991), the amount of local ice accretion is only related to the local water collection efficiency. It can be seen in Figure 7.6(e) that the ice thickness decreases as developing downstream, which is in accord with the previous studies (Özgen and Canıbek 2009), in which the water collection gradually decreases from stagnation point to downstream.

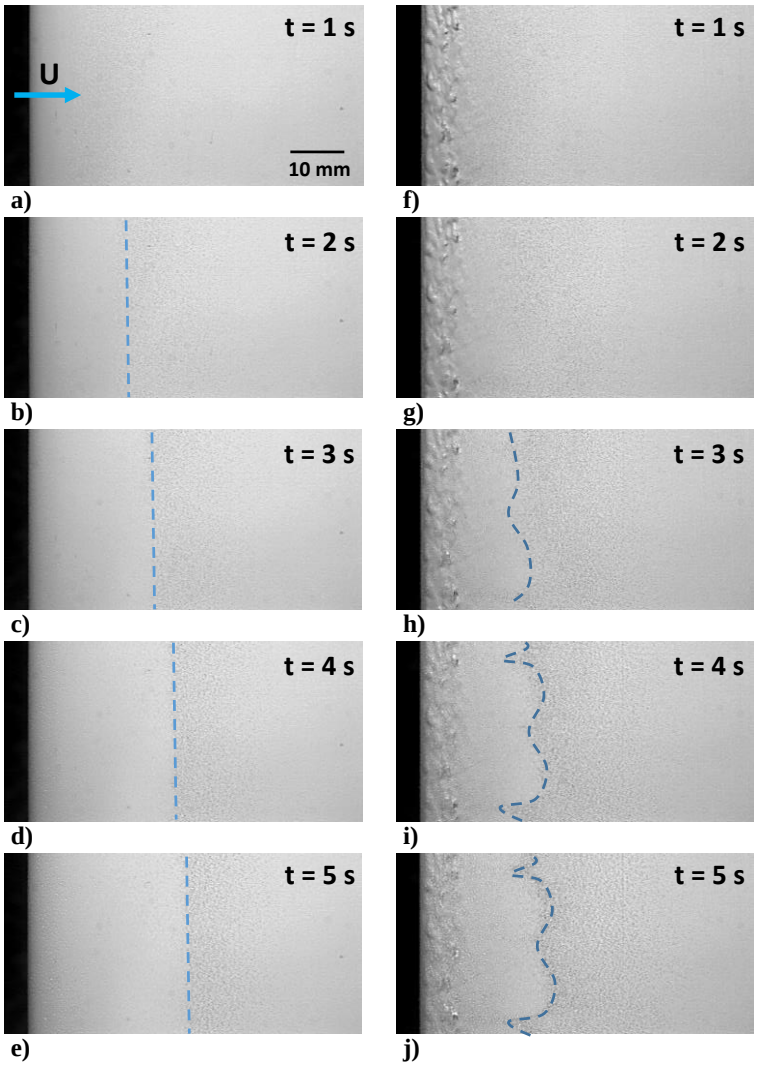

Figure 7.6 Snapshots of initial ice accretion process on the airfoil with smooth leading edge ((a)-(e)) and realistic roughness ((f)-(j)) with a free-stream velocity of 40 m/s, LWC of 3.0 g/m^3, and temperature of −15°C.

For the ice accretion on the airfoil with realistic roughness (Figure 7.6(f)-(j)), the irregular roughness distribution will affect the water impingement distribution at the initial water collection. As the water droplets impinge on the airfoil surface, due to the blockage at the elevated elements and the trap at the recessed spots, the water collection distribution is essentially altered. However, it is hard to visualize this change in the icing snapshots.

Since the water collection distribution is changed, the initial ice accretion will be redistributed. As more droplets impinge on the wing surface, ice forms over the roughness elements with an altered distribution as can been seen in Figure 7.6(f)-(g). Besides the redistribution of initial water collection, the roughness elements could essentially change the boundary layer flow, and therefore enhance the heat convection at typical regions. More ice forms at the regions with higher turbulence intensity and enhanced heat convection. It can be observed in Fig 7(h)-(j) that finger-like boundary forms between the ice film region and the rough spots region. An alternativity in ice accretion exists at downstream of the realistic roughness. A possible reason for this phenomenon is that there is an alternative high- and low-heat convection distribution in spanwise induced by the leading edge roughness distribution.

The initial ice accretion process at a temperature of −5 °C is shown in Figure 7.7. For the ice accretion over the smooth leading edge (Fig. 8a-e), the icing process exhibits the same characteristics as the previous works (Waldman and Hu 2015). As water droplets impinge on the wing surface, since the air temperature is not cold enough to convectively remove all the latent heat of fusion in the collected water, a smooth water/ice film first forms at the leading edge as shown in Figure 7.7(a)-(b). As time goes on, more water deposits on the surface and rivulets develop due to instability (Figure 7.7(c)-(e)). A water/ice run-back process can be clearly observed. The film region extends as more water impinges on the surface. Meanwhile, typical water/ice rivulets develop further downstream along with the film extension.

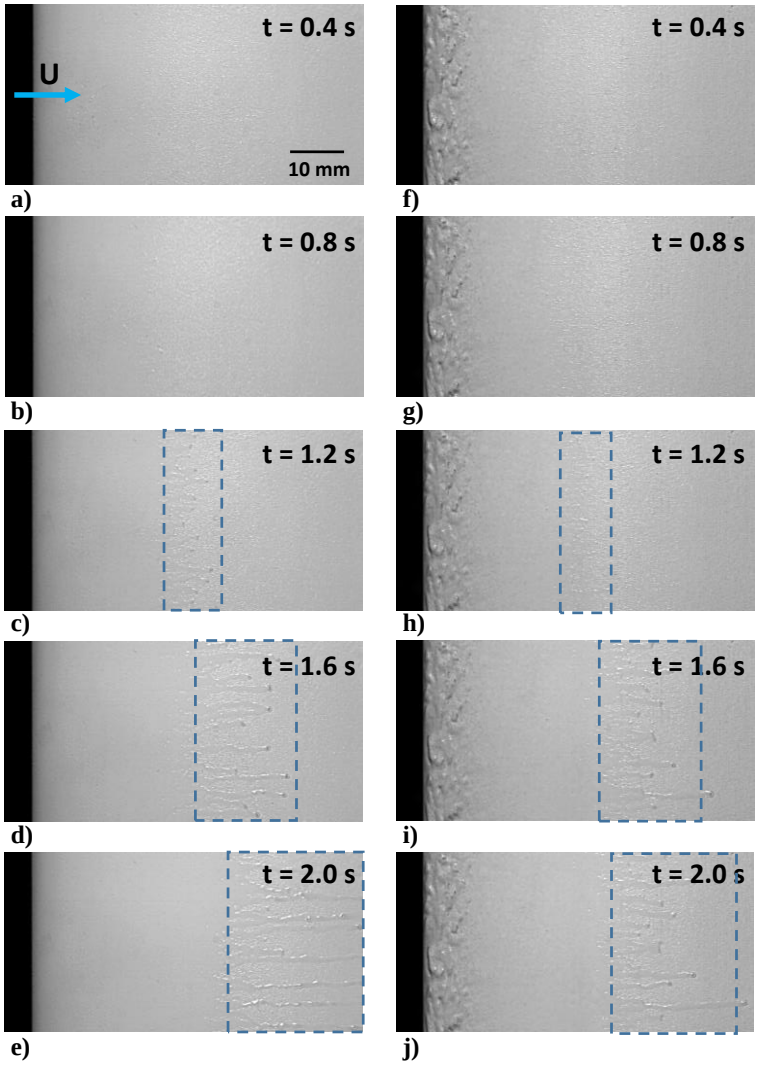

Figure 7.7 Snapshots of initial ice accretion process on the smooth airfoil ((a)-(e)) and rough airfoil ((f)-(j)) with the freestream velocity, U=40 m/s; LWC=3.0 g/m^3; and T =−5°C.

For the ice accretion over the rough leading edge (Figure 7.7(f)-(j)), though the leading edge roughness alters the water collection process, a similar water/ice run-back behavior is observed in the figure. Since the heat convection under this temperature condition is not adequate to remove all the latent heat of fusion in the water, the water will run back and flush over the roughness elements. The leading edge roughness basically traps the water

run-back and deaccelerates the water/ice film formation, and therefore the development of rivulets as shown in Figure 7.7(f)-(i). However, as time goes on, the general icing distribution develops the same as that over the smooth model as shown in Figure 7.7(j).

7.4 Temperature Mapping of Transient Initial Ice Accretion

In the last section, the ice accretion processes are visualized in the snapshot time series of high-speed videography. Typical icing features can be extracted from the video visualization. Qualitative descriptions of the effect of the realistic roughness were made. To quantify the essential mechanism of the roughness effect on the initial water collection, heat transfer enhancement, and water/ice transport process, infrared thermography was used to map the temperature distribution over the wing surface, and therefore extract more transient details during the ice accretion process.

The evolution of temperature distribution over the NACA 23012 airfoil during ice accretion process with the freestream velocity of 40 m/s, LWC of 3.0 g/m^3, and temperature of −15°C is shown in Figure 7.8. The icing process under this condition is a typical rime ice accretion. The impinging water droplets freeze immediately upon impact. The amount of ice accretion is linearly related to the release of latent heat of fusion, and therefore the temperature increment. Thus, based on the temperature map, the ice accretion distribution can be estimated. For the ice accretion over the smooth leading edge (Figure 7.8(a)-(e)), as the water impinge on the smooth leading edge, ice forms and extends downstream. The temperature is uniformly distributed in span-wise around the leading edge as shown in Figure 7.8(a). The amount of water collection and ice accretion is therefore uniformly distributed along spanwise. As more water impinges on the surface,

the extent of ice film develops downstream, and a clear temperature gradient presents along chordwise, which corresponds to the ice accretion gradient (Figure 7.8(b)-(e)). The boundaries in the temperature gradient appear to be straight lines.

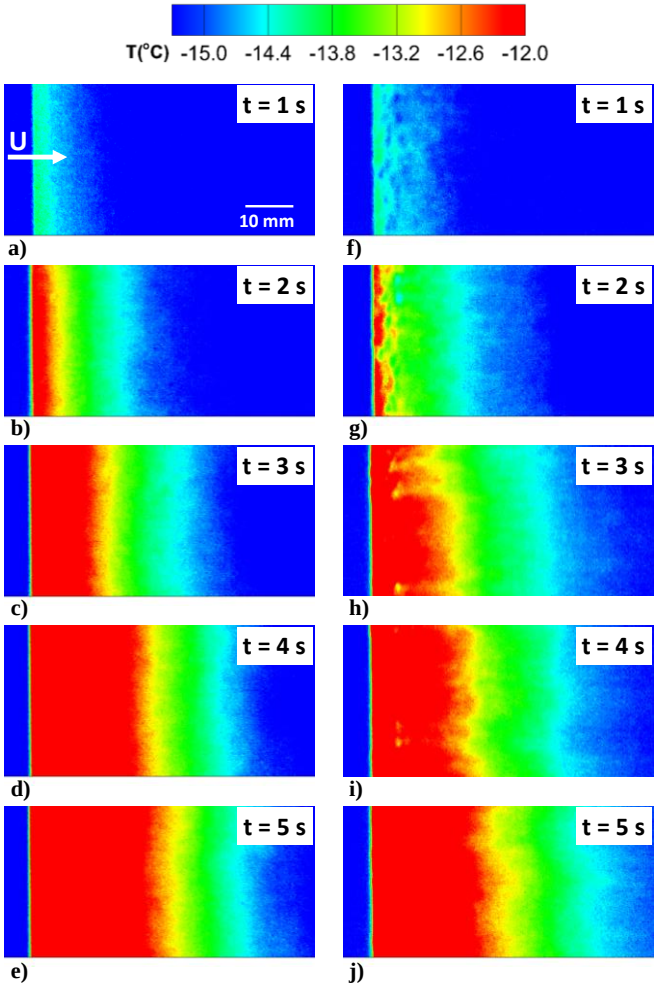

Figure 7.8 Evolution of temperature distribution during initial ice accretion process on the smooth airfoil ((a)-(e)) and rough airfoil ((f)-(j)) with the freestream velocity, U=40 m/s; LWC=3.0 g/m^3; and T =−15°C.

For the ice accretion over the rough leading edge (Figure 7.8(f)-(j)), the realistic roughness elements essentially change the water impingement distribution as also stated in the icing visualization. Based on the temperature map at the initial water collection

stage (Figure 7.8(f)-(g)), nonuniformity in both span- and chord-wise temperature distribution can be clearly seen in the figure. As more water impinge on the surface, ice forms over the leading edge roughness elements and extends downstream. It can be found in Figure 7.8(h)-(j) that jagged boundaries present in the temperature gradient. Alternative "crests" and "troughs" appear at the temperature boundaries. It is suggested that the realistic roughness distribution could induce span-wise-alternating low- and high-momentum pathways (LMPs and HMPs, respectively) separated by stream-wise-oriented swirling motions (Barros and Christensen 2014), which could essentially affect the heat convection and ice accretion.

The evolution of temperature distribution over the smooth and rough leading edge at an air temperature of −5°C is shown in Figure 7.9. The icing process under this condition is a typical glaze ice accretion. There is a water/ice run-back behavior occurring on the surface. The amount of local ice accretion is basically determined by the local freezing ratio. For the ice accretion over the smooth leading edge (Figure 7.9(a)-(e)), as the water droplets uniformly impinge on the smooth leading edge, the temperature map presents a nonuniformity as shown in Figure 7.9(a). Since the heat convection is not adequate to remove all the latent heat of fusion in the impinged water, the droplets will deform and splash before freezing downstream, which can be clearly observed in the figure. As more water impinge on the surface, a water/ice film forms and run back, along with which, beads and rivulets form due to the surface tension effects as can be seen in Figure 7.9(b)-(e).

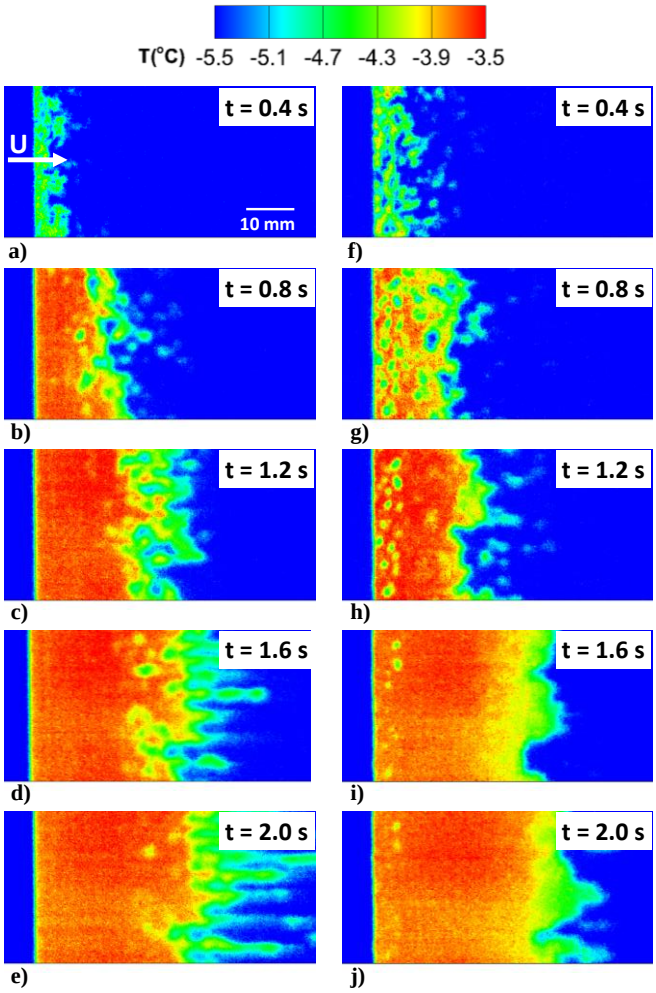

Figure 7.9 Evolution of temperature distribution during initial ice accretion process on the smooth airfoil ((a)-(e)) and rough airfoil ((f)-(g)) with the freestream velocity, U=40 m/s; LWC=3.0 g/m^3; and T =−5°C.

For the ice accretion over the rough leading edge (Figure 7.9(f)-(j)), due to the redistribution of the water collection by the realistic roughness, and the droplets deformation break-up, the impinged water is spread out over the roughness elements as shown in Figure 7.9(f). As more water impinges on the surface, the water/ice flush over the realistic roughness, and transport downstream as shown in Figure 7.9(g)-(h). Here, the roughness elements basically trapped the water film flow and deaccelerate the water/ice

transport. After the redirection and deceleration of the roughness elements, a water/ice film transport downstream with fewer beads formation as compared with that over the smooth model. As time goes on, the water film break into rivulets as shown in Figure 7.9(i)-(j).

7.5 Results and Discussion

7.5.1 Initial Water Collection Distribution

As described in the evolution of temperature distribution during icing process in the last section, the initial water collection is essentially redistributed by the realistic roughness elements around the leading edge. To further elucidate the effect of the roughness on the initial water collection process, the initial-state (t = 0.5 s) leading edge temperature distribution over the smooth and rough model at freestream velocity of 40 m/s, LWC of 3.0 g/m^3, and temperature of −15°C is zoomed in for further discussion.

The temperature distribution over the smooth leading edge can be found in Figure 7.10. It can be seen that the temperature evenly distributes along spanwise with a clear chordwise temperature gradient. Since the amount of ice accretion is linearly related to the temperature increment, the ice accretion distribution can be evaluated based on the temperature increment distribution. Meanwhile, at the initial state, the amount of ice accretion is solely determined by the water collection distribution. Therefore, the chordwise water collection distribution can be estimated based on the chordwise temperature increment distribution. By averaging the chordwise temperature increment distribution along spanwise, the overall temperature increment distribution in chordwise can be acquired as shown in the figure. The maximum ice accretion occurs at the

stagnation point as indicated in the figure. The amount of ice accretion gradually decreases at downstream along chordwise. This distribution is in accord with the water collection efficiency distribution in the previous studies (Bilodeau et al. 2015).

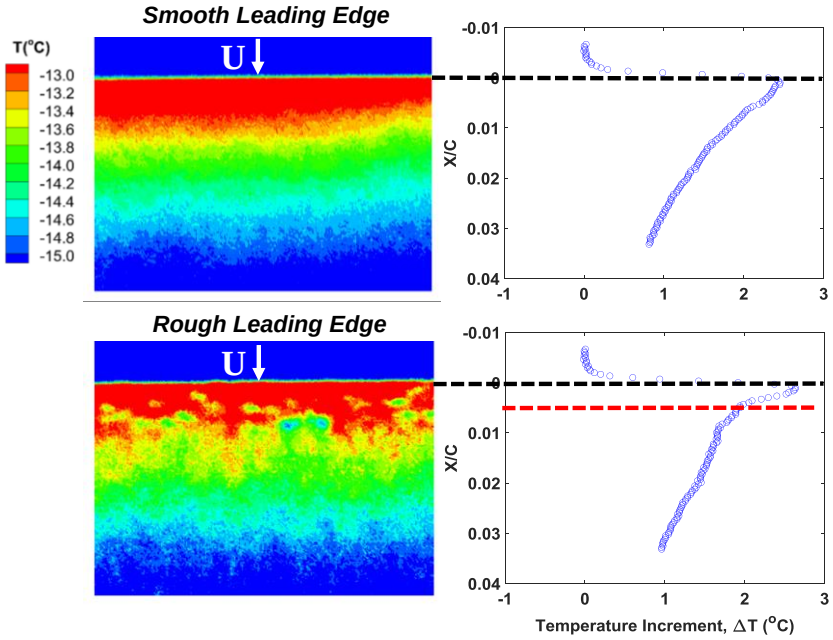

Figure 7.10 Initial-state leading edge temperature distribution and span-averaged temperature distribution over the smooth and the rough leading edge at test conditions of U=40 m/s; LWC=3.0 g/m^3; and T =−15°C.

The temperature distribution around the rough leading edge is also shown in Figure 7.10. The irregularity can be clearly observed in the temperature distribution. Moreover, there are no obvious gradient boundaries in the temperature map. The existence of the realistic roughness elements essentially redistributes the water collection. It should be noticed that though the local water collection is redistributed, the overall chordwise water collection distribution still follows the same trend as that of the smooth model. As compared with the results for the smooth leading edge, a greater temperature drop right

after the stagnation point can be observed. The roughness elements tend to block and capture more water droplets at the initial water collection.

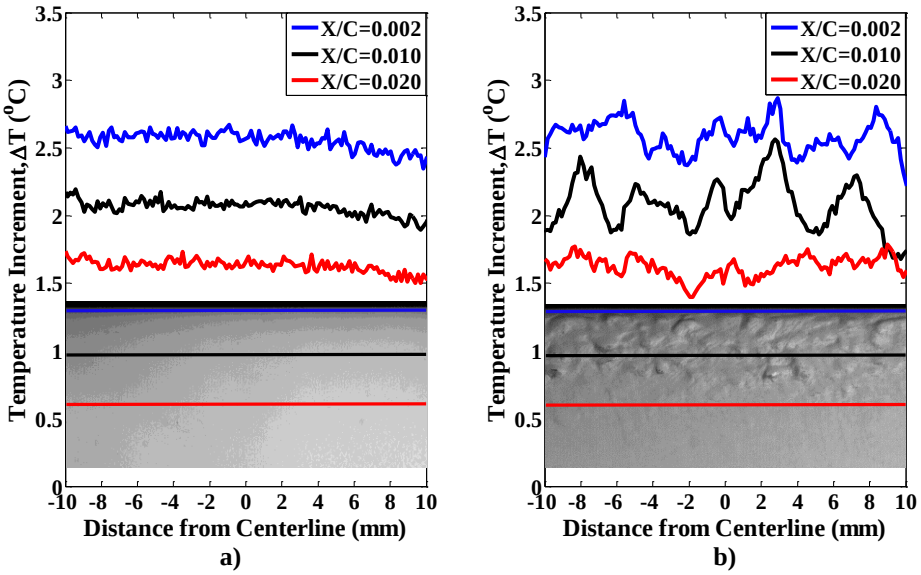

Figure 7.11 Initial-state span-wise temperature distribution over (a) smooth leading edge, and (b) rough leading edge at test conditions of U=40 m/s, LWC=3.0 g/m^3, and T =−15°C.

In order to further evaluate the effect of the realistic roughness on the initial water collection distribution, the spanwise temperature increment distribution at three chordwise locations (X/C = 0.002, 0.010, and 0.020) are extracted for both smooth and rough leading edge as shown in Figure 7.11. It can be found that the spanwise temperature increment distribution over the smooth leading edge present fairly constant temperature levels at each chordwise location. However, for the temperature distribution over the rough leading edge, the jagged distribution at the different chordwise location can be observed. Therefore, the realistic roughness essentially breaks the uniformity of the spanwise water collection distribution, and the variation of the local water collection is suggested to be closely related to the intense span-wise gradients in topographical height.

7.5.2 Evaluation of Convective Heat Transfer Enhancement

It has been studied that the realistic roughness distribution could induce span-wise-alternating low- and high-momentum pathways (LMPs and HMPs, respectively) separated by stream-wise-oriented swirling motions with LMPs embodying intense regions of enhanced TKE and RSS (Barros and Christensen 2014). Since the convective heat transfer can be essentially enhanced as a consequence of the enhanced TKE, and accelerate ice accretion, the low-momentum pathways (LMPs) tends to deposit more ice. Therefore, the convective heat transfer enhancement can be evaluated based on the ice accretion and temperature increment distributions, which could provide identifications of the span-wise-alternating low- and high-momentum pathways over the ice accreting surface.

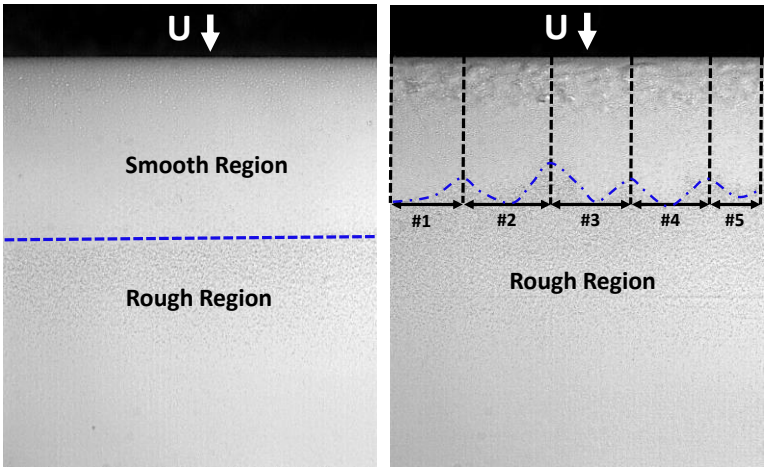

Figure 7.12 Ice accretion over (a) smooth leading edge, and (b) rough leading edge at a wind speed of U=40 m/s, LWC of 3.0 g/m^3, and temperature of −15°C.

The snapshots for ice accretion over the smooth and rough leading edge at t = 10s at a wind speed of 40 m/s, LWC of 3.0 g/m^3, and temperature of −15°C are shown in Figure 7.12. It can be seen that for the ice accretion over the smooth leading edge model, there is

a distinct straight line boundary between the smooth ice film and the rough spots regions as shown in Figure 7.12(a). The ice accretion uniformly distributes along spanwise. For the airfoil with realistic roughness, however, the ice accretion presents a finger-like boundary between the ice regions as shown in Figure 7.12(b). The ice "crests" can be identified as numbered in the figure.

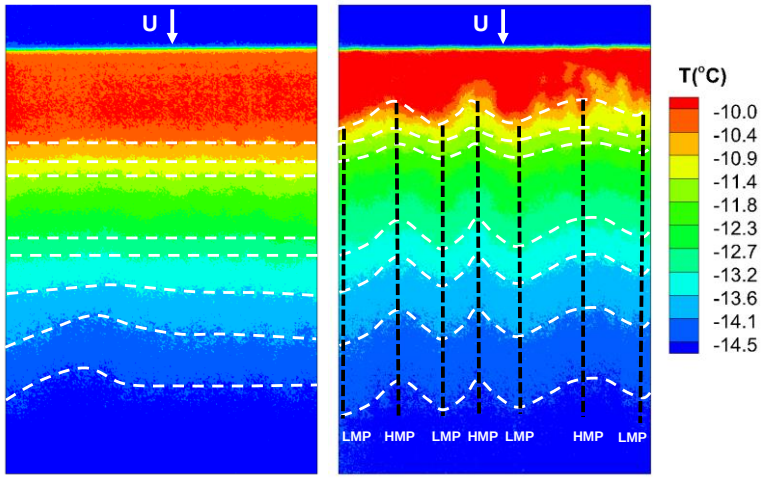

Figure 7.13 Temperature mapping over (a) smooth and (b) rough leading edge under test conditions of U=40 m/s; LWC=3.0 g/m^3; and T =−15°C.

To further identify the icing features, The temperature distribution over the smooth and rough leading edge at t = 10 s wind speed of 40 m/s, LWC of 3.0 g/m^3, and temperature of −15°C are shown in Figure 7.13. It can be seen that, for the ice accretion over the smooth leading edge model, an obvious temperature gradient exists with distinct boundaries as shown in Figure 7.13(a). In accordance with the result in the ice image, ice uniformly accretes in spanwise. For the rough leading edge model, the temperature map presents a distribution with multiple finger-like boundaries between the temperature gradients as shown in Figure 7.13(b). Based on the previous studies on the span-wise-

alternating low- and high-momentum pathways induced by realistic roughness (Barros and Christensen 2014), the LMPs tends to capture more ice due to the higher TKE and enhanced heat convection. Therefore, based on the temperature map in Figure 7.13(b), the LMPs and HMPs can be identified. The local convective heat transfer is essentially enhanced at LMPs as indicated in the figure.

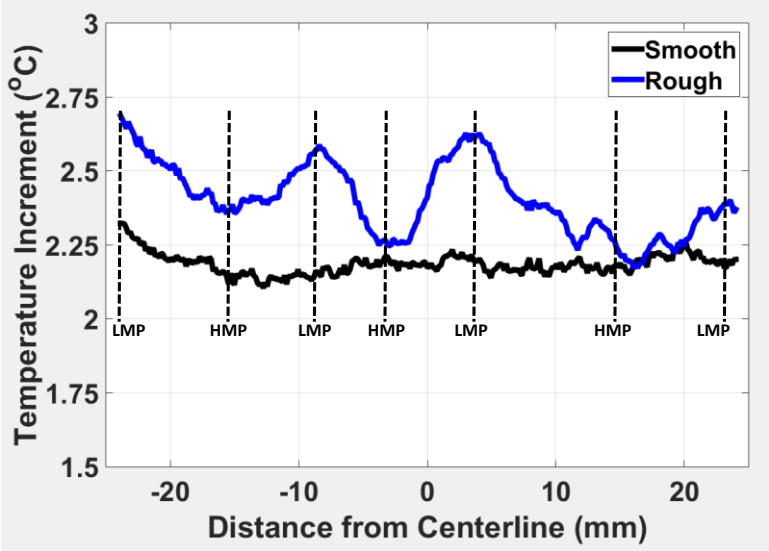

Figure 7.14 Chord-averaged spanwise temperature increment distribution under test conditions of U=40 m/s; LWC=3.0 g/m^3; and T =−15°C.

By averaging the spanwise temperature increment distribution along chordwise, an obvious difference in the spanwise temperature increment, and therefore the ice accretion between the smooth and rough leading edge model can be acquired as shown in Figure 7.14. It can be found that the temperature increment distribution for smooth leading edge model remains at a fairly constant level, indicating a uniform ice accretion and heat convection along spanwise. For the rough leading edge model, however, distinct “crests” and “trough” present in the figure. Based on this temperature increment distribution, the

LMPs and HMPs can be identified, and the convective heat transfer enhancement can be estimated.

7.6 Conclusions

In this study, an NACA 23012 airfoil with realistic ice roughness was modeled to investigate the effect of the realistic roughness on the transient initial ice accretion and heat transfer process. Icing experiments were performed in the ISU Icing Research Wind Tunnel (ISU-IRWT). A high-speed videography was used to visualize the icing process including droplet collection, ice formation, water run-back, and the evolution of the accreted ice. An infrared thermometry combined with thermocouple measurements was also applied to map the temperature distribution over the ice accreting airfoil surfaces. The temperature measurement provides insight into the initial droplet collection distribution and the heat transfer process during ice accretion. The effect of the realistic ice roughness on the droplet collection distribution and the heat transfer enhancement were elucidated.

Based on the initial-state leading edge temperature distribution and the spanwise-averaged chordwise temperature profile, the overall chordwise water collection distribution can be quantified, and found to follow the same trend for both smooth and rough leading edge models, with the maximum ice accretion occurring at the stagnation point, though the local water collection is redistributed and highly irregulated for the rough leading edge model. The roughness elements tend to block and capture more water at the initial water collection. The realistic roughness essentially breaks the uniformity of the spanwise water collection distribution, and the variation of the local water collection is suggested to be closely related to the intense span-wise gradients in topographical height.

The convective heat transfer enhancement can be evaluated based on the ice accretion and temperature increment distributions as more ice accrete in downstream, which provide identifications of the span-wise-alternating low- and high-momentum pathways over the ice accreting surface. The ice accretion on the smooth leading edge model uniformly distributes along spanwise with an obvious temperature gradient in chordwise. While the ice accretion on the rough leading edge model presents multiple finger-like boundaries between the temperature gradients. Distinct “crests” and “trough” in the temperature distribution represent the LMPs and HMPs, which indicates the convective heat transfer enhancement regions.

CHAPTER 8
GENERAL CONCLUSION

1. Major Accomplishments of the Current Research

In the present study, a multi-transducer ultrasonic pulsed-echo (MTUPE) technique was developed to achieve time-resolved film thickness measurements of wind-driven surface water flows over a test plate, which is pertinent to the glaze ice accreting process over an aircraft wing. The time series of the measured film thickness profiles of the surface water flows were analyzed to quantify the characteristics of wind-driven surface water transport process at different test conditions.

A novel strategy was proposed to characterize the different ice structures pertinent to the ice accretion on aircraft. While the ultrasonic attenuation function in the pulse-echo field was successfully derived, a feasibility study was performed to discriminate the different ice samples based on the frequency-dependent ultrasonic attenuation. Two obviously different ice structures: rime-like and glaze-like ice, were prepared and tested for the ultrasonic attenuation measurements. It is demonstrated that the ultrasonic attenuation characteristics may be utilized to classify the ice accreted on aircraft wings.

A comprehensive experimental study was also conducted to quantify the transient surface water transport and dynamic ice accreting process over airfoil surfaces at different icing conditions. The experiments were conducted in an Icing Research Tunnel available at Iowa State University (ISU-IRT). While the transient behaviors of surface water run-back over an NACA 23012 airfoil with realistic initial ice roughness at the airfoil leading

edge are investigated using an innovative digital image projection-correlation (DIPC) technique, the unsteady heat transfer and phase changing processes under different icing conditions were examined in details based on measured surface temperature maps over the ice accreting surfaces by using an infrared thermal imaging system.

The underlying physics were elucidated to improve our understanding of the important microphysical processes pertinent to aircraft icing phenomena to develop more effective and robust anti-/de-icing strategies to ensure safer and more efficient aircraft operations in cold weather.

2. Recommendations for Future Research

Based on the research accomplishments as discussed above, the following recommendations are made:

1) The multi-transducer ultrasonic pulse-echo (MTUPE) technique has been developed to quantify the surface water film flow over a flat plate. However, the MTUPE technique has not been applied on a wing model. More temporal details of the surface water transport behavior can be resolved if the MTUPE system can be integrated into a wing section.

2) The ultrasonic attenuation characteristics in the different ice structures were demonstrated to be significantly different. However, more quantitative measurements are desired to provide more evidence in the classification of the accreting ice on aircraft.

3) The transient surface water transport and heat transfer processes have been evaluated with the presence of the realistic initial ice roughness. Since the convective heat

transfer, air boundary layer flows field, and the surface water flow is coupled and interacted. To better understand the effect of the initial ice roughness, the temporally resolved air boundary layer flow should be measured and evaluated by using PIV technique.

4) To further elucidate the heat transfer process with the presence of the realistic initial ice roughness, quantitative measurements with stable heat flux supply is desired to assess the distribution of the heat convection coefficient over the wing surface.

APPENDIX STATISTICS OF WIND-DRIVEN WATER FILM FLOW

Introduction

For the evaluation of the wind-driven water film flow, The mean thickness and corresponding variance were usually performed by assuming a normal distribution, and neglected the correlation of data collections in time series.

To better understand the thickness variation at an individual point, we estimated the mean thickness and the variance of mean using auto-correlation method. An estimator of water thickness at time *t* is formulated based on auto-regression modelling, in which the order and estimation of the regression parameters are determined. Based on the data collection from the measurement and the estimator, a truth model of the local film thickness variation is established. A simulation process is performed based on the truth model. A comparison of the variance of mean of film thickness with and without consideration of time correlation is presented.

Measurement Results

The time history of the water film thickness variation at an individual point in the wind-driven surface water film flow is shown in Fig. 1. In this measurement, the sample number is 481 as shown in the figure. It can be clearly seen that periodical wave structures present in the time domain.

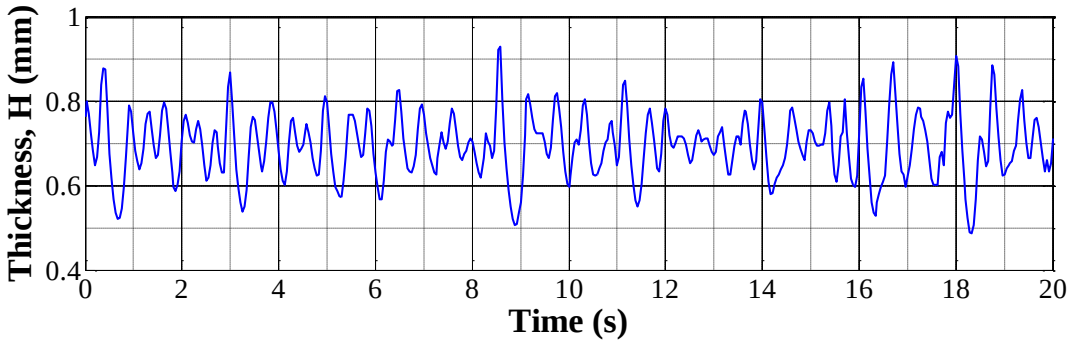

Figure. 1: Time history of water film thickness variation

Statistical Analysis of Thickness Variation at Single point

As we statistically process the data collection, each data point in the time domain is a value generated by a variable at the time point, e.g. the thickness data at $\boldsymbol{t = t_i}$ s is $\boldsymbol{h_i}$; It is a value generated by variable $\mathbf{H_i}$. If we regard the 481 thickness data points as thickness values generated by 481 thickness variables, we get into the world of statistics, and multiple statistical methods can be applied in dealing with these variables.

Assumptions

When we observe the time history of the thickness variation, the data collection $\{H\}_{i=1}^{n}$ presents a high correlation between successive variables. These variables are not identically independent distributed (iid). Therefore, we cannot simply apply the statistic theories talked in John E. Freund's mathematical statistics (Miller 2004). The regression and correlation models in time series should be used here. Before that, we will propose two assumptions based on the real physical mechanisms of the water film flow.

Since the water supply and wind speed are controlled to be constant during the data collection, the film thickness does not essentially increase as time goes on, but just varies

around a stationary point. This process can be regarded as a steady state. So we assume that the mean and variance of the thickness values of each variable are identically the same; and the autocorrelation of two variables depends only on the time delay between them, $\tau = t_2 - t_1$. Then we have:

$$E(\mathrm{H}_k) = \mu_{\mathrm{H}}$$

$$E\left[\left(H_k - \mu_{H_k}\right)\left(H_j - \mu_{H_j}\right)\right] = R(t_i, t_j) = R(t_i - t_j)$$

Here, R is the auto-correlation function of $\boldsymbol{H_k}$ and $\boldsymbol{H_j}$. It is utilized as it gives correlation between the elements of a series and others from the same series separated from them by a given interval (time lag).

$$R(k) = \sum_{i=1}^{n-k}(H_i H_{i+k})$$

We call such a discrete-time random process, **H(*t*),** wide-sense stationary. Now we propose the two assumptions in this study:

1. The thickness variables $\{H\}_{i=1}^{n}$ are identically distributed with same mean (μ_X) and variance (σ_X), $\{H\}_{i=1}^{n} \sim f_H(H)$.
2. The discrete-time random process, H(*t*) is wide-sense stationary; the autocorrelation of two variables depends only on the time-lag between them.

Estimation of Mean Thickness and Variance of Mean

As we deal with the data collection $\{H\}_{i=1}^{n}$, we first want to get the mean of the film thickness. Based on the 1st assumption, we can simply calculate the mean thickness as follows:

$$\hat{\mu}_H = \frac{1}{n}\sum_{k=1}^{n} H_k = 0.6952$$

Here, we need to know the variance of the mean thickness. In the current study, however, we only have one data collection, so we apply the following method to obtain the variance of the mean.

First, we subtract $\hat{\mu}_H$ for the data set, and then calculate $\sigma^2_{\hat{\mu}_H}$ as follows:

$$\sigma^2_{\hat{\mu}_H} = E\left(\hat{\mu}_H^2\right) = E\left[\left(\frac{1}{n}\sum_{k=1}^{n} H_k\right)\cdot\left(\frac{1}{n}\sum_{j=1}^{n} H_j\right)\right] = \frac{1}{n^2}E\left(\sum_{k=1}^{n}\sum_{j=1}^{n} H_k H_j\right) = \frac{1}{n^2}\sum_{k=1}^{n}\sum_{j=1}^{n} E\left(H_k H_j\right)$$

$$\sigma^2_{\hat{\mu}_H} = \frac{1}{n^2}\sum_{k=1}^{n}\sum_{j=1}^{n} R\left(|k-j|\right) = \frac{1}{n^2}\left\{nR(0) + 2(n-1)R(1) + 2(n-2)R(2) + \cdots + 2R(n-1)\right\}$$

$$\sigma^2_{\hat{\mu}_H} = \frac{1}{n}\sum_{k=-(n-1)}^{n-1}\frac{n-|k|}{n}R(k)$$

The estimate of the auto-correlation function of the data collection can be acquired. Both unbiased and biased estimates are plotted as shown in Fig. 2. For the unbiased estimate result, it can be seen that at the two ends, the ***R*** varies significantly as compare to that at the center. It is due to the reduction of estimation size as time-lag increases:

$$\hat{R}_{unbiased}(k) = \frac{1}{n-k}\sum_{i=1}^{n-k}\left(H_i H_{i+k}\right)$$

However, for the biased estimate result, ***R*** value decays as time-lag increases, which is physically reasonable, the bigger of the time-lag, the less of the correlation coefficient.

$$\hat{R}_{biased}(k) = \frac{1}{n}\sum_{i=1}^{n-k}\left(H_i H_{i+k}\right)$$

Therefore, we use the biased estimate of the auto-correlation function to estimate the variance of the mean obtained in the measurement, then we can get

$$\sigma^2_{\hat{\mu}_X} = \frac{1}{n}\sum_{k=-(n-1)}^{n-1}\frac{n-|k|}{n}R(k) = 6.2148\times10^{-7}$$

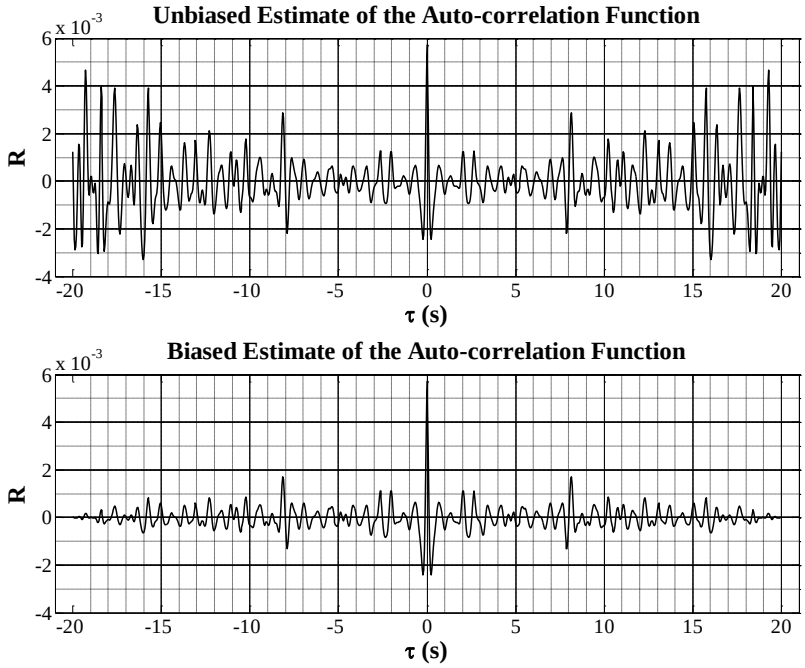

Figure. 2: Estimate of the auto-correlation function. upper: unbiased; lower: biased

Modelling of Thickness Estimator

A major objective of this statistical study is to establish relationships that make it possible to predict thickness variable H(t_i) at moment t_i in terms of other given variables. As we have the data collection $\{H\}_{i=1}^{n}$ from the measurement, we can formulate an autoregressive (AR) model, which specifies that the output variable depends linearly on its own previous values (Madsen 2007).

$$\hat{H}_k = c + \sum_{i=1}^{p} \varphi_i H_{k-i}$$

where $\varphi_1, \varphi_2, \cdots, \varphi_p$ are the parameters of the model, c is a constant. In the current study, we subtract all variable by μ_X, so we have

$$E\left(\hat{H}_k\right) = c + E\left(\sum_{i=1}^{p} \varphi_i H_{k-i}\right) \Rightarrow 0 = c + 0$$

Now the estimator is simplified to $\hat{H}_k = \sum_{i=1}^{p} \varphi_i H_{k-i}$. To solve the AR parameters ($\varphi_1, \varphi_2, \cdots, \varphi_p$), there are many ways to estimate, such as the ordinary least squares procedure and method of moments (Yule-Walker equations). Here we use the Yule-Walker equations (Yule 1927; Walker 1931).

$$R_m = \sum_{k=1}^{p} \varphi_k R_{m-k}$$

where $m = 1, \ldots, p$, yielding p equations. Here R_m is the auto-covariance function of X_k. Now we have the equation

$$\begin{bmatrix} R_1 \\ R_2 \\ R_3 \\ \vdots \\ R_p \end{bmatrix} = \begin{bmatrix} R_0 & R_1 & R_2 & \cdots \\ R_1 & R_0 & R_1 & \cdots \\ R_2 & R_1 & R_0 & \cdots \\ \vdots & \vdots & \vdots & \ddots \\ R_{p-1} & R_{p-2} & R_{p-3} & \cdots \end{bmatrix} \begin{bmatrix} \varphi_1 \\ \varphi_2 \\ \varphi_3 \\ \vdots \\ \varphi_p \end{bmatrix}$$

Which can be solved for all $\{\varphi_1, \varphi_2, \cdots, \varphi_p\}$. As we have the parameters for different orders of the estimator model, to implement an estimator model, we need to determine the order and the corresponding parameters. So we set another parameter

$$MSE = \frac{1}{n} \sum_{i=1}^{n} \left(\hat{H}_i - H_i \right)^2 = \frac{1}{n} \sum_{i=1}^{n} \left(\sum_{i=1}^{p} \varphi_i H_{k-i} - H_i \right)^2$$

Figure. 3: Auto-regression order vs MSE (mean squared error)

Figure. 3 shows us the MSE at different estimator orders. It can be clearly seen that at the order of 2, the MSE decreases to a lower level can stays constant. So we choose 2nd order estimator, which can well estimate the thickness variance.

$$\hat{H}_k = \varphi_1 H_{k-1} + \varphi_2 H_{k-2}$$

By solving the parameter equation (see the code in Appendix), we can get the parameters for the 2nd order estimator: $\varphi_1 = 1.5120$; $\varphi_2 = -0.7950$. A comparison of the thickness variation from measurement and the estimator can be found in Fig. 8. It is clear that the two data sets agree well. The 2nd order estimator developed in this section can be used to predict the temporal thickness at any moment t_i.

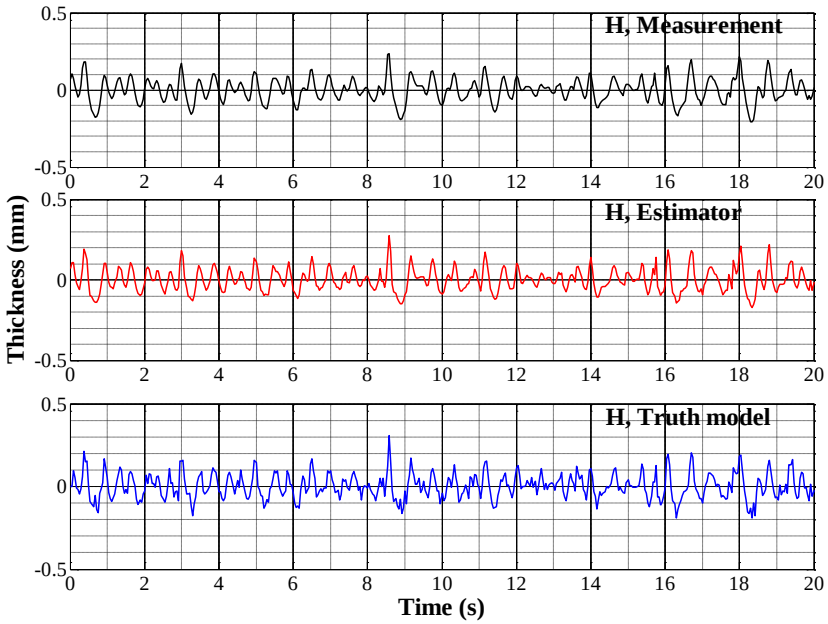

Figure. 4: Time series of thickness variance from (a). Measurement, (b). Estimator, (c). Truth Model

Formulation of Truth Model

As we obtained the 2nd order AR estimator, the truth model can be formulated by adding white noise to the estimator.

$$H_k = \varphi_1 H_{k-1} + \varphi_2 H_{k-2} + v_k$$

where v_k is the white noise process with zero mean and constant variance σ_v^2. We multiply this equation by H_k and apply expectation function on both sides:

$$E(H_k H_k) = \varphi_1 E(H_k H_{k-1}) + \varphi_2 E(H_k H_{k-2}) + E(H_k v_k)$$

Since the autocorrelation of H_k depends only on the lag in between. Thus, we have

$$R(0) = \varphi_1 R(1) + \varphi_2 R(2) + \sigma_v^2$$

As we repeat the process by multiplying H_{k-1} and H_{k-2}, another two equations can be formulated:

$$R(1) = \varphi_1 R(0) + \varphi_2 R(1)$$

$$R(2) = \varphi_1 R(1) + \varphi_2 R(0)$$

Rearrange the three equations, and we can get the following matrix equation:

$$\begin{bmatrix} \varphi_1 & \varphi_2 & 0 \\ (1-\varphi_1)/\varphi_2 & 0 & 0 \\ -\varphi_1/\varphi_2 & 1/\varphi_2 & 1 \end{bmatrix} \begin{bmatrix} R(1) \\ R(2) \\ \sigma_v^2 \end{bmatrix} = \begin{bmatrix} R(0) \\ R(0) \\ R(0) \end{bmatrix}$$

Solve the equation, and we have $R(1) = 0.0048$, $R(2) = 0.0028$, and $\sigma_v^2 = 0.0006$. For the further auto correlations, we have $R(k) = \varphi_1 R(k-1) + \varphi_2 R(k-2)$, where $k = 3, 4, \ldots n$.

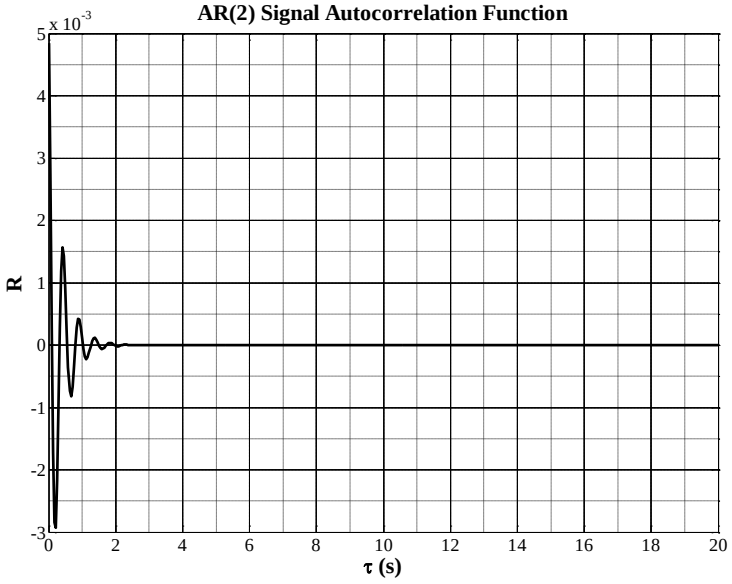

Figure. 5: AR(2) signal autocorrelation function

The AR autocorrelation function is shown in Fig. 5. A typical exponential decay can be observed as time-lag increases.

Since the variance of the white noise is obtained in the above calculation, the random v_k component can be generated, and finally formulate the truth model with the estimator parameters.

$$H_k = \varphi_1 H_{k-1} + \varphi_2 H_{k-2} + v_k$$

where $\varphi_1 = 1.5120$; $\varphi_2 = -0.7950$, v_k is the white noise process with zero mean and constant variance $\sigma_v^2 = 0.0006$. The time series of the thickness variation based on the truth model is shown in Fig. 8. A good agreement is presented when compare with the data collection from the measurement. If we subtract the measurement data by the truth model, another random component, error process, can be generated as shown in Fig. 6.

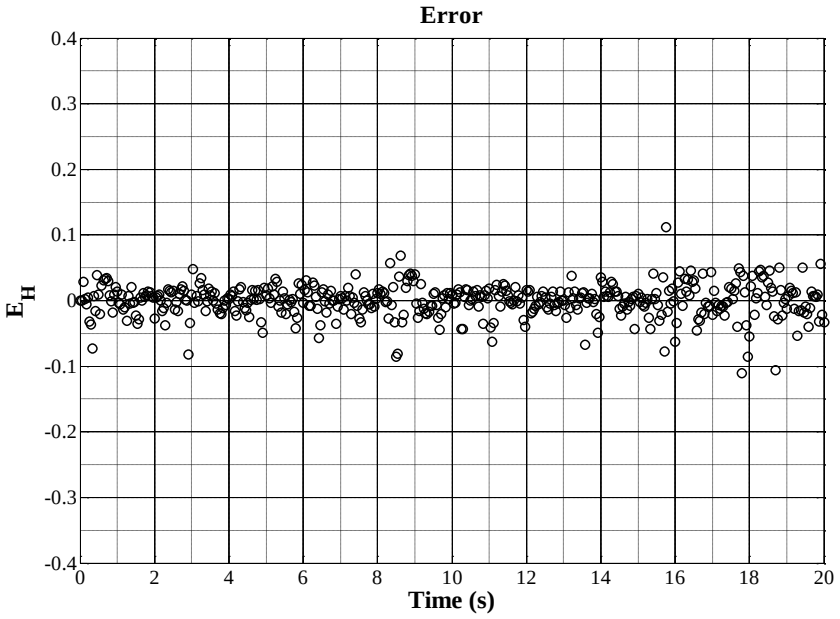

Figure. 6: Error process based on measurement and truth model

Simulations

Since we have established the truth model of the correlated thickness variation, now we can run simulations to find out the distribution of the mean thickness, and the variance of the mean.

We did 5000 simulations for the same sample size of N = 481. The distribution of mean thickness can thus be formulated as shown in Fig. 7.

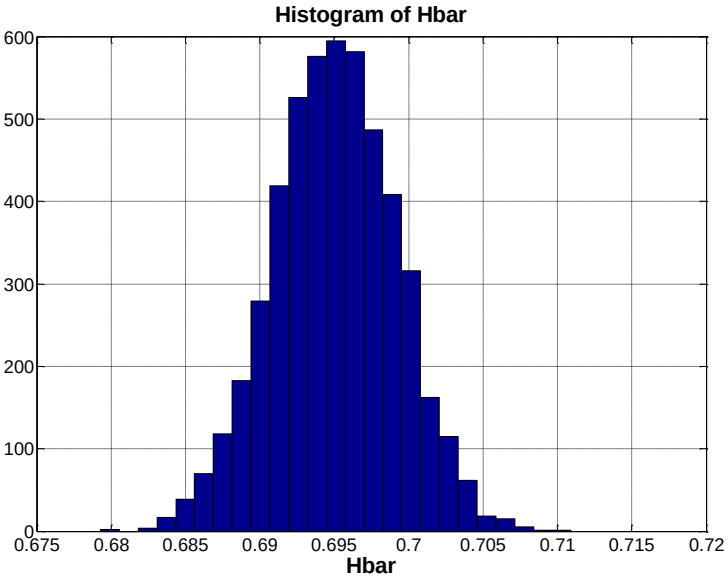

Figure. 7: Histogram of Hbar based on simulations

For each simulation, we can also get the variance of the mean. If we assume the variables are *iid*, then we can simply calculate the variance using $\sigma^2_{\mu_H} = \sigma^2_H / N$. However, the thickness variables in this study are not *iid*, the variance of the mean should be calculated using

$$\sigma^2_{\hat{\mu}_H} = \frac{1}{n^2}\sum_{k=1}^{n}\sum_{j=1}^{n} R(|k-j|) = \frac{1}{n^2}\{nR(0) + 2(n-1)R(1) + 2(n-2)R(2) + \cdots + 2(n-p)R(n-p)\}$$

where p is the maximum lag in the estimation. Therefore, by performing the simulations, we can compare the distributions of the two estimation of $Var(\bar{H})$.

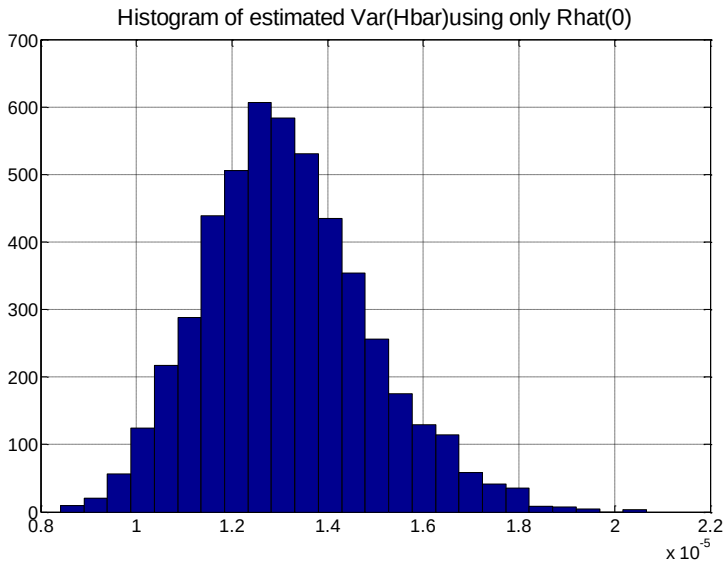

Figure. 8: Histogram of $Var\left(\bar{H}\right)$ using only R(0)

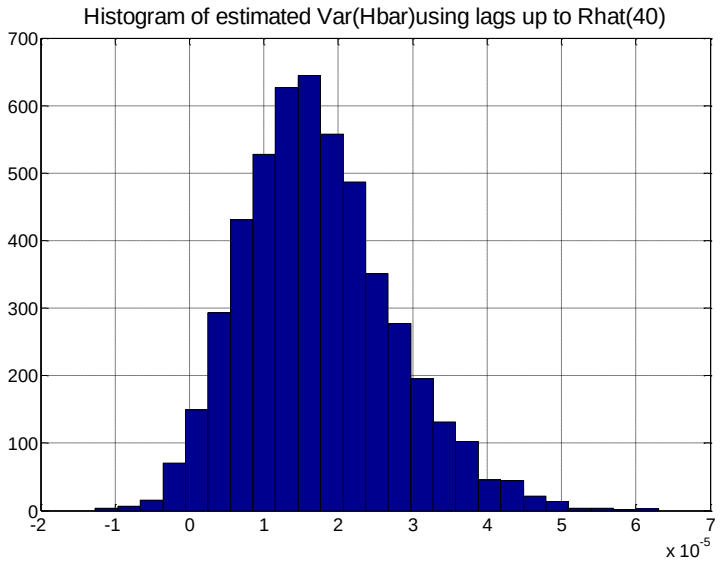

Figure. 9: Histogram of $Var\left(\bar{H}\right)$ using lags up to R(40)

The histogram of the variance of the mean thickness using only R(0) and that using lags up to R(40) are shown in Fig. 8 and 9, respectively. It can be seen that the distribution of $Var\left(\bar{H}\right)$ using lags up to R(40) is much wider than that using only R(0), which indicates

that the time correlation in the data collection has a big effect on the statistical distribution of the mean thickness. Many of the previous studies regarding the data collection as *iid* should be corrected using the model formulated in this study.

Conclusions

In this study, the mean thickness and the variance of mean are estimated using auto-correlation method. An estimator of water thickness at any moment *t* is formulated based on auto-regression modelling, in which the order and estimation of the regression parameters are determined. Based on the data collection from the measurement and the estimator, a truth model of the local film thickness variation is established. A simulation process is performed based on the truth model. A comparison of the variance of mean of film thickness with and without consideration of time correlation is presented. The time correlation in the data collection has a big effect on the statistical distribution of the mean thickness.

BIBLIOGRAPHY

Abbasi R, Abdou Y, Abu-Zayyad T, et al (2011) Measurement of acoustic attenuation in South Pole ice. Astropart Phys 34:382–393. doi: 10.1016/j.astropartphys.2010.10.003

Abbasi R, Abdou Y, Ackermann M, et al (2010) Measurement of sound speed vs. depth in South Pole ice for neutrino astronomy. Astropart Phys 33:277–286. doi: 10.1016/j.astropartphys.2010.01.012

Appiah-Kubi P (2011) US Inflight Icing Accidents and Incidents, 2006 to 2010. University of Tennessee

Arimilli R V, Keshock EG, Smith ME (1984) Measurements of local convective heat transfer coefficients on ice accretion shapes. In: AIAA 22nd Aerospace Sciences Meeting, Reno, Nevada.

Barros JM, Christensen KT (2014) Observations of turbulent secondary flows in a rough-wall boundary layer. J Fluid Mech 748:null–null.

Bassey CE, Simpson GR (2007) Aircraft ice detection using time domain reflectometry with coplanar sensors. In: IEEE Aerospace Conference Proceedings. IEEE, pp 1–6

Bilodeau DR, Habashi WG, Fossati M, Baruzzi GS (2015) Eulerian Modeling of Supercooled Large Droplet Splashing and Bouncing. J Aircr 52:1611–1624. doi: 10.2514/1.C033023

Bogorodskii V V., Gavrilo VP, Nikitin VA (1976) Sound-Propagation in Ice Crystallized From Salt-Water. Sov Phys Acoust 22:158–159.

Bons J, Christensen K (2007) A Comparison of Real and Simulated Surface Roughness Characterizations. In: 37th AIAA Fluid Dynamics Conference and Exhibit. p 3997

Bons JP (2002) St and Cf augmentation for real turbine roughness with elevated freestream turbulence. In: ASME Turbo Expo 2002: Power for Land, Sea, and Air. American Society of Mechanical Engineers, pp 349–363

Bragg M, Kerho M, Cummings M (1994) The effect of initial ice roughness on airfoil aerodynamics. In: 32nd Aerospace Sciences Meeting and Exhibit. American Institute of Aeronautics and Astronautics,

Bragg MB, Cummings MJ, Lee S, Henze CM (1996) Boundary-layer and heat-transfer measurements on an airfoil with simulated ice roughness. AIAA Pap 866:1–16.

Caliskan F, Hajiyev C (2013) A review of in-flight detection and identification of aircraft icing and reconfigurable control. Prog Aerosp Sci 60:12–34.

Cazabat AM, Heslot F, Troian SM, Carles P (1990) Fingering instability of thin spreading films driven by temperature gradients. Nature 346:824–826.

Cebeci T, Kafyeke F (2003) Aircraft icing. Annu Rev Fluid Mech 35:11–21.

Cobelli PJ, Maurel A, Pagneux V, Petitjeans P (2009) Global measurement of water waves by Fourier transform profilometry. Exp Fluids 46:1037–1047.

Cochard S, Ancey C (2008) Tracking the free surface of time-dependent flows: image processing for the dam-break problem. Exp Fluids 44:59–71.

Cohen LS, Hanratty TJ (1965) Generation of waves in the concurrent flow of air and a liquid. AIChE J 11:138–144. doi: 10.1002/aic.690110129

Craik ADD (1966) Wind-generated waves in thin liquid films. J Fluid Mech 26:369. doi: 10.1017/S0022112066001289

Dong W, Zhu J, Zheng M, Chen Y (2015) Thermal Analysis and Testing of Nonrotating Cone with Hot-Air Anti-Icing System. J Propuls Power 1–8. doi: 10.2514/1.B35378

Du Y, Gui Y, Xiao C, Yi X (2010) Investigation on heat transfer characteristics of aircraft icing including runback water. Int J Heat Mass Transf 53:3702–3707. doi: 10.1016/j.ijheatmasstransfer.2010.04.021

Dukhan N, De Witt KJ, Masiulaniec KC, Van Fossen GJ (2003) Experimental Frossling Numbers for Ice-Roughened NACA 0012 Airfoils. J Aircr 40:1161–1167. doi: 10.2514/2.7205

Dukhan N, Va G J, Masiulaniec K, DeWitt K (1996) Convective heat transfer coefficients from various types of ice roughened surfaces in parallel and accelerating flow. In: AIAA, Aerospace Sciences Meeting and Exhibit, 34 th, Reno, NV.

Ensminger D, Bond LJ (2011) Ultrasonics: fundamentals, technologies, and applications. CRC Press, Boca Raton

Filipczynski L, Pawlowski Z, Wehr J (1966) Ultrasonic methods of testing materials. Butterworths, London

Fortin G, Laforte J-L, Ilinca A (2006) Heat and mass transfer during ice accretion on aircraft wings with an improved roughness model. Int J Therm Sci 45:595–606. doi: 10.1016/j.ijthermalsci.2005.07.006

Gao H, Rose JL (2009) Ice detection and classification on an aircraft wing with ultrasonic shear horizontal guided waves. Ultrason Ferroelectr Freq Control IEEE Trans 56:334–344.

Gent RW, Dart NP, Cansdale JT (2000) Aircraft icing. Philos Trans R Soc London Ser A Math Phys Eng Sci 358:2873–2911.

Green SD (2006) A study of US inflight icing accidents and incidents, 1978 to 2002. In: 44th AIAA Aerospace Sciences Meeting and Exhibit. Reno, Nevada,

Gudra T, Najwer L (2011) Ultrasonic Investigation of Snow and Ice Parameters. Acta Phys Pol A 120:625–629. doi: 10.12693/APhysPolA.120.625

Hansman RJ, Kirby MS (1987) Comparison of wet and dry growth in artificial and flight icing conditions. J Thermophys Heat Transf 1:215–221.

Hansman RJ, Kirby MS (1986) Measurement of ice growth during simulated and natural icing conditions using ultrasonic pulse-echo techniques. J Aircr 23:492–498.

Hansman RJ, Kirby MS (1985) Measurement of ice accretion using ultrasonic pulse-echo techniques. J Aircr 22:530–535.

Hansman RJ, Turnock SR (1989) Investigation of surface water behavior during glaze ice accretion. J Aircr 26:140–147.

Hansman RJ, Yamaguchi K, Berkowitz B, Potapczuk M (1991) Modeling of surface roughness effects on glaze ice accretion. J Thermophys Heat Transf 5:54–60.

Henry R, Hansman RJ, Breuer KS (1994) Measurement of heat transfer variation on surface roughness elements using infrared techniques. AIAA Pap 94–801.

Henry RC, Guffond D, Fran-atilde, et al (2000) Heat transfer coefficient measurement on iced airfoil in small icing wind tunnel. J Thermophys Heat Transf 14:348–354.

Henry RC, Hansman RJ, Breuer KS (1995) Heat transfer variation on protuberances and surface roughness elements. J Thermophys Heat Transf 9:175–180.

Homola MC, Nicklasson PJ, Sundsbø PA (2006) Ice sensors for wind turbines. Cold Reg Sci Technol 46:125–131.

Hongerholt DD, Willms G, Rose JL (2002) Summary of results from an ultrasonic in-flight wing ice detection system. In: AIP Conference Proceedings. AIP, pp 1023–1028

Hu H, Wang B, Zhang K, et al (2014) Quantification of transient behavior of wind-driven surface droplet/rivulet flows using a digital fringe projection technique. J Vis 1–14.

Incropera FP (2011) Fundamentals of heat and mass transfer. John Wiley & Sons

Jeong H, Hsu DK (1995) Experimental analysis of porosity-induced ultrasonic attenuation and velocity change in carbon composites. Ultrasonics 33:195–203.

Kabov OA, Scheid B, Sharina IA, Legros J-C (2002) Heat transfer and rivulet structures formation in a falling thin liquid film locally heated. Int J Therm Sci 41:664–672.

Kerho M, Bragg M (1995) Effect of large distributed leading-edge roughness on boundary layer development and transition. In: 13th Applied Aerodynamics Conference. American Institute of Aeronautics and Astronautics,

Kind RJ, Potapczuk MG, Feo A, et al (1998) Experimental and computational simulation of in-flight icing phenomena. Prog Aerosp Sci 34:257–345.

Krautkrämer J, Krautkrämer H (1990) Ultrasonic testing, 4th edn. Springer Verlag

Lee S, Broeren A, Addy H, et al (2012) Development of 3D Ice Accretion Measurement Method. In: 4th AIAA Atmospheric and Space Environments Conference. American Institute of Aeronautics and Astronautics,

Lee S, Broeren AP, Kreeger RE, et al (2014) Implementation and Validation of 3-D Ice Accretion Measurement Methodology. In: 6th AIAA Atmospheric and Space Environments Conference. American Institute of Aeronautics and Astronautics,

Lel V V, Al-Sibai F, Leefken A, Renz U (2005) Local thickness and wave velocity measurement of wavy films with a chromatic confocal imaging method and a fluorescence intensity technique. Exp Fluids 39:856–864.

Li F-C, Chen W-L, Li H, Zhang R (2010) An ultrasonic transmission thickness measurement system for study of water rivulets characteristics of stay cables suffering from wind--rain-induced vibration. Sensors Actuators A Phys 159:12–23.

Li F-C, Serizawa A (2004) Experimental study on flow characteristics of a vertically falling film flow of liquid metal NaK in a transverse magnetic field. Fusion Eng Des 70:185–199.

Li X, Bai J, Wang K, Shi Y (2014) The application of eulerian two-phase flow method in airfoil ice accretion. Sin-Phys Mech Astron 44:258–266.

Liu Q, Wu K-T, Kobayashi M, et al (2008) In-situ ice and structure thickness monitoring using integrated and flexible ultrasonic transducers. Smart Mater Struct 17:45021–45023.

Liu Y, Bond LJ, Hu H (2016) Reconstruction of wave features in wind-driven water film flow using ultrasonic pulse-echo technique. In: AIP Conference Proceedings 1706. AIP Publishing, p 020015

Liu Y, Chen W, Bond LJ, Hu H (2014) A Feasibility Study to Identify Ice Types by Measuring Attenuation of Ultrasonic Waves for Aircraft Icing Detection. In: ASME 2014 4th Joint US-European Fluids Engineering Division Summer Meeting collocated with the ASME 2014 12th International Conference on Nanochannels, Microchannels, and Minichannels. American Society of Mechanical Engineers, pp V01BT22A003–V01BT22A003

Liu Y, Hu H (2016) An Experimental Investigation on the Convective Heat Transfer Process over an Ice Roughened Airfoil. In: 54th AIAA Aerospace Sciences Meeting. American Institute of Aeronautics and Astronautics,

Liu Y, Waldman R, Hu H (2015) An Experimental Investigation on the Unsteady Heat Transfer Process Over an Ice Accreting NACA 0012 Airfoil. In: 53rd AIAA Aerospace Sciences Meeting. American Institute of Aeronautics and Astronautics,

Madsen H (2007) Time series analysis. CRC Press

Mart SR, McClain ST, Wright LM (2012) Turbulent Convection From Deterministic Roughness Distributions With Varying Thermal Conductivities. J Turbomach 134:51030.

McClain ST, Hodge BK, Bons JP (2010) The Effect of Element Thermal Conductivity on Turbulent Convective Heat Transfer From Rough Surfaces. J Turbomach 133:21024.

Messinger BL (1953) Equilibrium temperature of an unheated icing surface as a function of air speed. J Aeronaut Sci (Institute Aeronaut Sci 20:29–42.

Miller I (2004) John E. Freund's Mathematical Statistics: With Applications. Pearson Education India

Mohseni M, Frioult M, Amirfazli A (2012) Simultaneous monitoring of ice accretion and thermography of an airfoil: an IR imaging methodology. Meas Sci Technol 23:105405.

Moin P (2009) Revisiting Taylor's hypothesis. J Fluid Mech 640:1–4.

Murphy DM, Koop T (2005) Review of the vapour pressures of ice and supercooled water for atmospheric applications. Q J R Meteorol Soc 131:1539–1565. doi: 10.1256/qj.04.94

Myers TG (2001) Extension to the Messinger model for aircraft icing. AIAA J 39:211–218.

Olsen W, Walker E (1986) Experimental evidence for modifying the current physical model for ice accretion on aircraft surfaces. Cleveland, OH, United States

Özgen S, Canıbek M (2009) Ice accretion simulation on multi-element airfoils using extended Messinger model. Heat Mass Transf 45:305–322. doi: 10.1007/s00231-008-0430-4

Petty KR, Floyd CDJ (2004) A statistical review of aviation airframe icing accidents in the US. In: Proceedings of the 11th Conference on Aviation, Range, and Aerospace Hyannis.

Poinsatte PE, Vanfossen GJ, Dewitt KJ (1989) Convective heat transfer measurements from a NACA 0012 airfoil in flight and in the NASA Lewis Icing Research Tunnel. In: 27th AIAA Aerospace Sciences Meeting. pp 8–11

Potapczuk MG (2013) Aircraft Icing Research at NASA Glenn Research Center. J Aerosp Eng 26:260–276.

Price PB (2006a) Attenuation of acoustic waves in glacial ice and salt domes. J Geophys Res. doi: 10.1029/2005JB003903

Price PB (2006b) Attenuation of acoustic waves in glacial ice and salt domes. J Geophys Res Solid Earth 111:n/a–n/a. doi: 10.1029/2005JB003903

Rogers PH, Van Buren AL (1974) An exact expression for the Lommel-diffraction correction integral. J Acoust Soc Am 55:724–728.

Rothmayer A (2003) On the Creation of Ice Surface Roughness by Interfacial Instabilities. In: 41st Aerospace Sciences Meeting and Exhibit. American Institute of Aeronautics and Astronautics,

Salvi J, Fernandez S, Pribanic T, Llado X (2010) A state of the art in structured light patterns for surface profilometry. Pattern Recognit 43:2666–2680.

Schagen A, Modigell M (2007) Local film thickness and temperature distribution measurement in wavy liquid films with a laser-induced luminescence technique. Exp Fluids 43:209–221.

Schlichting H, Gersten K, Gersten K (2000) Boundary-layer theory. Springer Science & Business Media

Schmerr LW (1998) Fundamentals of Ultrasonic Nondestructive Evaluation. Springer US, Boston, MA

Selfridge AR (1985) Approximate Material Properties in Isotropic Materials. IEEE Trans Sonics Ultrason 32:381–394. doi: 10.1109/T-SU.1985.31608

Serizawa A, Nagane K, Kamei T, et al (2004) Dynamic measurement of liquid film thickness in stratified flow by using ultrasonic echo technique. In: Proceedings of the 4th International Topical Meeting on Nuclear Thermal Hydraulics. Taipei, Taiwan,

Shin J (1996) Characteristics of surface roughness associated with leading-edge ice accretion. J Aircr 33:316–321. doi: 10.2514/3.46940

Shin J, Bond TH (1992) Results of an icing test on a NACA 0012 airfoil in the NASA Lewis Icing Research Tunnel. In: 30th Aerospace Sciences Meeting & Exhibit. American Institute of Aeronautics and Astronautics, Reno,

Smith SW (1997) The scientist and engineer's guide to digital signal processing. California Technical Pub. San Diego

Smith WL (1929) Weather problems peculiar to the New York-Chicago airway. Mon Weather Rev 57:503–506.

Steuernagle J, Roy K, Wright D (2008) Aircraft Icing.

Svilainis L (2012) Review of high resolution time of flight estimation techniques for ultrasonic signals. In: 2013 International Conference NDT, Telford, UK,(Sep. 8-12, 2013). pp 1–12

Taylor GI (1938) The Spectrum of Turbulence. Proc R Soc London A Math Phys Eng Sci 164:476–490.

Tecson L, McClain ST (2013a) Convective Enhancement of Surfaces with Realistic Ice Roughness Distributions. In: 5th AIAA Atmospheric and Space Environments Conference. American Institute of Aeronautics and Astronautics,

Tecson L, McClain ST (2013b) Modeling of Realistic Ice Roughness Element Distributions to Characterize Convective Heat Transfer. In: 5th AIAA Atmospheric and Space Environments Conference. American Institute of Aeronautics and Astronautics.

Thomas SK, Cassoni RP, MacArthur CD (1996) Aircraft anti-icing and de-icing techniques and modeling. J Aircr 33:841–854. doi: 10.2514/3.47027

Treiber M, Kim J-Y, Jacobs LJ, Qu J (2009) Correction for partial reflection in ultrasonic attenuation measurements using contact transducers. J Acoust Soc Am 125:2946–2953.

Ueno K, Farzaneh M (2011) Linear stability analysis of ice growth under supercooled water film driven by a laminar airflow. Phys Fluids 23:042103.

Umchid S (2008) Frequency dependent ultrasonic attenuation coefficient measurement. In: Proc. 3rd International Symposium on Biomedical Engineering. pp 234–238

Vargas M (2007) Current Experimental Basis for Modeling Ice Accretions on Swept Wings. J Aircr 44:274–290. doi: 10.2514/1.23323

Vargas M, Broughton H, Sims JJ, et al (2007) Local and Total Density Measurements in Ice Shapes. J Aircr 44:780–789. doi: 10.2514/1.23326

Vargas M, Tsao J-C (2008) Time-Sequence Observations of the Formation of Ice Accretions on Swept Wings. In: 46th AIAA Aerospace Sciences Meeting and Exhibit. American Institute of Aeronautics and Astronautics,

Vellekoop MJ, Jakoby B, Bastemeijer J (1999) A Love-wave ice detector. In: Ultrasonics Symposium, 1999. Proceedings. 1999 IEEE. IEEE, pp 453–456

Vogt C, Laihem K, Wiebusch C (2008) Speed of sound in bubble-free ice. J Acoust Soc Am 124:3613–3618.

Waldman R, Hu H (2015) High-Speed Imaging to Quantify the Transient Ice Accretion Process on a NACA 0012 Airfoil. In: 53rd AIAA Aerospace Sciences Meeting.

Walker G (1931) On periodicity in series of related terms. Proc R Soc London Ser A, Contain Pap a Math Phys Character 518–532.

Wang B, Lohry W, Zhang S, Hu H (2012) Development of a Digital Fringe Projection Technique to Quantify Surface Film/Rivulet Flows. In: 50th AIAA Aerospace Sciences Meeting including the New Horizons Forum and Aerospace Exposition. Nashville, Tennessee,

Wang X, Bibeau E, Naterer GF (2007) Experimental correlation of forced convection heat transfer from a NACA airfoil. Exp Therm Fluid Sci 31:1073–1082.

Wang X, Naterer G, Bibeau E (2008) Convective Heat Transfer from a NACA Airfoil at Varying Angles of Attack. J Thermophys Heat Transf 22:457–463.

Willis GE, Deardorff JW (1976) On the use of Taylor's translation hypothesis for diffusion in the mixed layer. Q J R Meteorol Soc 102:817–822. doi: 10.1002/qj.49710243411

Winkler J, Bragg M (1996) Local flowfield about large distributed roughness in the initial ice accretion process. In: 34th Aerospace Sciences Meeting and Exhibit. American Institute of Aeronautics and Astronautics,

Wright WB (1999) User manual for the NASA Glenn ice accretion code LEWICE. National Aeronautics and Space Administration, Glenn Research Center ; National Technical Information Service, distributor, Cleveland, Ohio

Wright WB, Budakian R, Putterman SJ (1996) Diffusing light photography of fully developed isotropic ripple turbulence. Phys Rev Lett 76:4528.

Wu P, Stepinski T (2000) Quantitative estimation of ultrasonic attenuation in a solid in the immersion case with correction of diffraction effects. Ultrasonics 38:481–485.

Yamaguchi K, Hansman RJ (1992) Heat transfer on accreting ice surfaces. J Aircr 29:108–113.

Yule GU (1927) On a method of investigating periodicities in disturbed series, with special reference to Wolfer's sunspot numbers. Philos Trans R Soc London Ser A, Contain Pap a Math or Phys Character 267–298.

Zeng F, Agnew SR, Raeisinia B, Myneni GR (2010) Ultrasonic attenuation due to grain boundary scattering in pure niobium. J Nondestruct Eval 29:93–103.

Zhang K, Hu H (2016a) An Experimental Study on The Transient Behavior of Wind-Driven Water Runback over a Flat Surface. In: 54th AIAA Aerospace Sciences Meeting. American Institute of Aeronautics and Astronautics,

Zhang K, Hu H (2016b) An Experimental Study on The Transient Behavior of Wind-Driven Water Runback over a Flat Surface. In: 54th AIAA Aerospace Sciences Meeting. American Institute of Aeronautics and Astronautics,

Zhang K, Liu Y, Rothmayer AP, Hu H (2014) An Experimental Study of Wind-Driven Water Film Flows over Roughness Array. In: 6th AIAA Atmospheric and Space Environments Conference. American Institute of Aeronautics and Astronautics,

Zhang K, Wei T, Hu H (2015) An experimental investigation on the surface water transport process over an airfoil by using a digital image projection technique. Exp Fluids 56:1–16. doi: 10.1007/s00348-015-2046-z

Zhang Q-C, Su X-Y (2002) An optical measurement of vortex shape at a free surface. Opt Laser Technol 34:107–113.

Zhang X, Dabiri D, Gharib M (1996) Optical mapping of fluid density interfaces: concepts and implementations. Rev Sci Instrum 67:1858–1868.

Zou J, Ye L, Ge J (2013) Ice type detection using an oblique end-face fibre-optic technique. Meas Sci Technol 24:35201.